2019

Frequency-Reconfigurable Microstrip Patch and Cavity-Backed Slot ESPARs

Wei Ouyang
University of Central Florida

FREQUENCY-RECONFIGURABLE MICROSTRIP PATCH AND CAVITY-
BACKED SLOT ESPARS

by

WEI OUYANG

B.S. South China University of Technology, 2014

A dissertation submitted in partial fulfillment of the requirements
for the degree of Doctor of Philosophy
in the Department of Electrical and Computer Engineering
in the College of Engineering & Computer Science
at the University of Central Florida
Orlando, Florida

Summer Term
2019

Major Professor: Xun Gong

ABSTRACT

Wireless communication systems have rapidly evolved over the past decade which has led to an explosion of mobile data traffic. Since more and more wireless devices and sensors are being connected, the transition from the current 4G/LTE mobile network to 5G is expected to happen within the next decade. In order to improve signal-to-noise ratio (SNR), system capacity, and link budget, beam steerable antenna arrays are desirable due to their advantage in spatial selectivity and high directivity. Electronically steerable parasitic array radiator (ESPAR) that can achieve low-cost continuously beamsteering using varactor diodes have attracted a lot of attention. This dissertation explores bandwidth enhancement of the ESPAR using frequency-reconfigurable microstrip patch and cavity-backed slot (CBS) antennas.

In chapter 2, an ESPAR of three closely-coupled rectangular patch elements that do not use phase shifters is presented; the beamsteering is realized by tunable reactive loads which are used to control the mutual coupling between the elements. Additional loading varactors are strategically placed on the radiating edge of all the antenna elements to achieve a 15% continuous frequency tuning range while simultaneously preserving the beamsteering capability at each operating frequency. Therefore, this frequency-reconfigurable ESPAR is able to provide spectrum diversity in addition to the spatial diversity inherent in a frequency-fixed ESPAR. A prototype of the patch ESPAR is fabricated and demonstrated to operate from 0.87 to 1.02 GHz with an instantaneous fractional bandwidth (FBW) of ~1%. At each operating frequency, this ESPAR is able to scan from -20 to +20 degrees in the H plane. However, the beamsteering of the patch ESPAR is limited in the H-plane and its instantaneous S_{11} fractional bandwidth (FBW) is very narrow.

This dissertation also explores how to achieve 2-D beamsteering with enhanced FBW using CBS antennas. A 20-element cavity-backed slot antenna array is designed and fabricated based on a CBS ESPAR cross subarray in chapter 5. This ESPAR array is able to steer the main beam from +45º to -45º in the E plane and from +40º to -40º in the H plane, respectively, without grating lobes in either plane. The impedance matching is maintained below -10 dB from 6.0 to 6.4 GHz (6.4% fractional bandwidth) at all scan angles. In addition, the CBS ESPAR exhibits minimum beam squint at all scan angles within the impedance matching bandwidth. This array successfully demonstrates the cost savings and associated reduction in required number of phase shifters in the RF front end by employing ESPAR technology.

Dedicated to my lovely family for all your love and support.

ACKNOWLEDGMENTS

TABLE OF CONTENTS

LIST OF FIGURES

LIST OF TABLES

CHAPTER 1   INTRODUCTION

This chapter begins by introducing the advantage of phased arrays in meeting the requirements of modern wireless communications systems. An overview of the electronically steerable parasitic array radiators (ESPARs) is presented to show how the ESPARs can reduce the cost and design complexity of phased arrays. In the end, an outline of this dissertation is listed.

1.1   Motivation

Phased arrays play an important role in modern military and commercial communications systems due to their advantages in high directivity and beamsteering ability. In point-to-point communications systems such as satellite networks [1]-[5], signals suffers from severe free space path loss (FSPL) due to the long distance between the satellites and ground stations. In order to compensate for the large FSPL, phased arrays are desirable to ensure a high signal-to-noise ratio (SNR) and track the satellite when the terminal moves or maneuvers [3]. In the cellular telephony industry, there has been significant growth in wireless communications devices such as smartphones, tablets and smart home systems in recent years; such rapid growth has led to an explosion of mobile data traffic with zettabytes of data being transmitted and received every year [6]. As a result, the demand for faster network speeds and larger system capacities is greater than ever. The transition from the current 4G/LTE mobile network to 5G is expected to happen within the next decade [7]-[10]. The increasingly crowded frequency spectrum hinders the implementation of next-generation communication systems and sensor networks. In order to efficiently exploit the existing frequency spectrum, the main communication system (primary user)

should be able to allow other systems (secondary users) to access the licensed bands opportunistically and dynamically. The secondary users are required to sense the spectrum in real time and identify transmission opportunities whenever the licensees (primary users) are not using their allocated spectrum. In such a system, phased arrays can further improve system capacity by enabling the spatial selectivity of both the transmitter and receiver.

For applications in target detection such as snow avalanches [11]-[13], frequency-modulated continuous wave (FMCW) radar is used to continuously transmitting chirps towards the target. In order to monitor the whole track of the snow avalanche, an antenna array with steering capability is required. In a mechanically scanned system, the beam agility is greatly limited by the speed of the antenna mounting structure, which takes around one second to scan the beam [14]. On the other hand, a fast-scanning phased array is more suitable to effectively track the fast-moving snow avalanches. However, the application of phased array antennas has been historically limited to military systems due to their prohibitively high fabrication cost.

In conventional phased arrays [15]-[19], each antenna element requires either a phase shifter or transmit/receive (T/R) module both of which are very costly. Therefore, the reduction in the number of required phase shifters would significantly reduce the total cost of a phased array system, making them much more attractive for commercial use. In addition, phase shifters exhibit a considerable amount of insertion loss which will reduce the antenna efficiency of the phased array and typically require the use of additional amplifiers, increasing system cost and DC power consumption [20], [21]. Therefore, it is of great benefit to reduce the number of phase shifters in the phased array while maintaining comparable beam steering performance.

1.2   Overview of Phased Arrays with Reduced Number of Phase Shifters

A great deal of research effort has gone towards reducing the number of phase shifters used in phased arrays. Nemit [22] proposed a network approach to divide a large array into several in-phase subarrays and use a single phase shifter for each subarray. Various microstrip patch phased arrays have been designed to demonstrate this concept [23]-[25]. However, this approach has a few inherent disadvantages such as many crossovers in the feeding network, limited beam scan angles, large scan losses, and narrow FBWs due to the use of long transmission lines connecting antenna elements. Alternatively, Akbar [26] presented a scalable phased array technique with a reduced number of phase shifters. Nevertheless, this approach requires the use of multiple amplifiers and showed limited scan angles of $\pm 18.5^{\circ}$.

1.2.1   Operation Mechanism of ESPAR

The development of the ESPAR has grown from the desire for low-cost beam steerable array with large scan ranges and low scan losses. The first prevalent ESPAR was proposed by Roger Harrington in 1974 [27]. The basic concept of the ESPAR is to feed one antenna element directly with an RF source and excite the surrounding parasitic antenna elements through the mutual coupling between them. The phase difference between the antenna elements can be controlled by adjusting the variable reactive loads connected to the parasitic elements. By properly designing the magnitude and phase of the induced current on the parasitic elements, the main beam of the ESPAR can be steered to a desired direction.

1.2.2 Advantages and Challenges of the ESPAR

The immediate benefit of employing the ESPAR technique in phased arrays is apparent. By utilizing an inexpensive tunable load, which is typically designed using varactors, within the ESPAR subarray, the total cost of the array can be substantially reduced. In addition, it is possible to independently control the frequency and spatial diversities in ESPAR antenna systems [28]. However, such benefits do not come without a new set of design challenges. While enabling frequency and radiation pattern reconfigurability is desired, the loss from the tuning elements degrades the efficiency of the ESPAR, especially at lower operating frequencies. High-Q microelectromechanical systems (MEMS) varactors [29]-[32] can be used to alleviate this issue. There are also challenges for wideband ESPAR designs. First, it is possible to have wider impedance matching bandwidth of ESPAR than a single antenna element. However, this increased impedance-matching bandwidth comes at the cost of poor pattern shapes and cross-polarization levels. Therefore, the useful operation bandwidth of the ESPAR is limited. Wideband antennas such as stacked patch antenna, slot antenna and dielectric resonator antenna can be employed to address this issue. Another important phenomenon that can limit ESPAR FBW is beam squinting, i.e. the changing of the main beam direction as a function of the operating frequency. Because the frequency variation of the mutual coupling can cause significant phase variation of the induced currents on the parasitic elements, beam squinting occurs within the impedance-matching bandwidth of the ESPAR, limiting its useful operation bandwidth. Care must be taken to achieve a relatively smooth frequency response of the Z-parameters for the ESPAR. In addition, a customized tunable load which incorporates a fixed inductor and varactor can be designed to extend reactively tuning range. By using this customized load, substantial magnitude of the

4

induced current can be maintained during beamsteering, which also alleviates the beam squinting issue.

1.3   Literature Review of ESPARs

1.3.1   Monopole ESPARs

The ESPAR has been an active area of research for the past ten years. This inexpensive beam steerable antenna array is initially designed to reduce DC power consumption and fabrication costs as compared to digital beamforming (DBF) antennas. This advantage is of great importance, especially for implementation in battery-operated wireless devices [33]. The arrays presented in [34]-[36] represented the first significant design improvement after [27] in which, the profile of the parasitic array was significantly reduced by using monopole antennas with a ground plane instead of the dipole antennas as shown in Figure 1. A conductive ground skirting is used to maximize the horizontal gain by lowering the elevation angle of the maximum radiation [37], [38]. It is noted in [39] that a further improvement in the design profile was achieved by embedding the ESPAR antenna array in a homogeneous dielectric material. However, this device only exhibits azimuthal beamsteering and its ability to be incorporated into electrically large arrays has not been explored. Moreover, manufacture of these devices is also a complex process compared to standard PCB fabrication, requiring precise machining of the ground plane and the conductive skirt. On the other hand, the ability to steer the beam around the boresight and simpler PCB fabrication process associated with microstrip patch antenna array have attracted strong research interest for employing ESPAR technique into planar array designs.
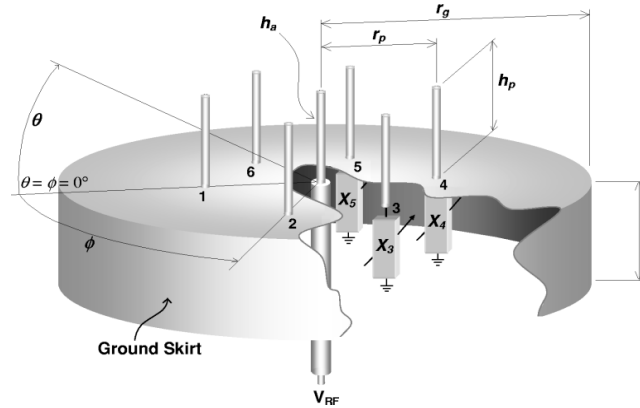
Figure 1: Monopole ESPAR structure (reprinted from Schlub, Lu, and Ohira (2003) [34]).

1.3.2   Microstrip Patch ESPARs

The extension of the ESPAR technique to microstrip patches has been previously explored. The coupling between the patch elements has been characterized in [40] and [41], which demonstrated that substantial magnitude coupling is possible with the coupling in the H plane. A three-element microstrip patch ESPAR H-plane array was presented in [42]. In this design, H-plane beam steering was achieved by placing tunable reactive loads at the ports of parasitic patch elements which are mutually coupled to the center driven patch element. However, the tunable reactive loads were realized by switching out various chip capacitors with fixed capacitances, avoiding the complications introduced by the requisite DC biasing network. A second design [43] introduced new reactive loading locations on the parasitic element as shown in Figure 2, allowing the mutual coupling between the antennas to be enhanced and well controlled. In addition, these devices include fully implemented DC biasing to realize individually control for the varactors with different functions. However, all the aforementioned patch ESPARs have a very limited impedance matching FBW, e.g. 1% [42]-[46]. Additionally, their beam steering capability is

6

limited in the H plane due to the difficulty of using the mutual coupling in the E plane without disturbing the radiating mode of the patch.

It is clear that frequency reconfigurable antenna techniques [47]-[51] can be utilized to extend the operational bandwidth of the patch ESPAR but the efficiency of the ESPAR will be degraded due to the introduction of the varactors on the radiating edges of the patch. In addition, it is desirable to achieve 2-D beamsteering. The best candidate for such an antenna will have wide impedance matching FBW and straightforward control of the mutual coupling in both E and H planes.
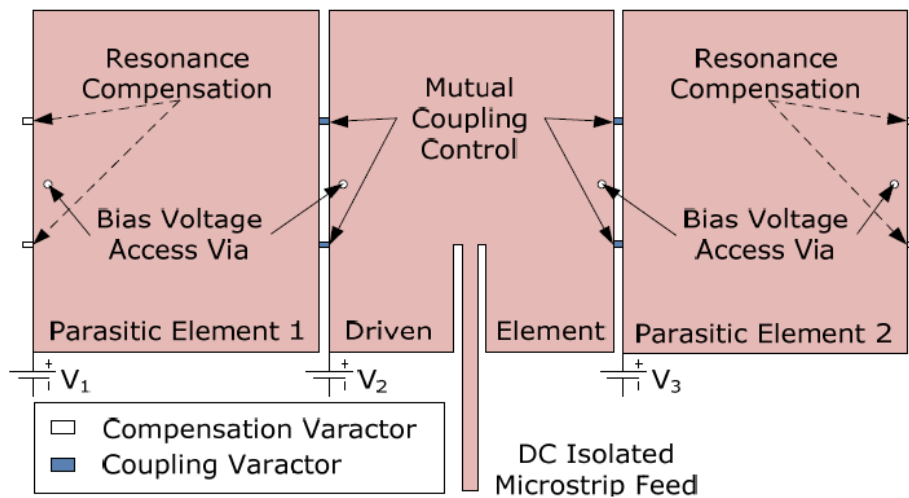
Figure 2: Single-layer microstrip patch ESPAR (reprinted from Luther, Ebadi, and Gong (2012) [43]).

1.3.3   Dielectric Resonator Antennas ESPARs

The dielectric resonator antenna (DRA) was originally proposed in the early 1980s [52]. Compared with microstrip antennas, the DRA exhibits many attractive features such as wide impedance matching FBW and low dissipation loss at high frequencies [56]. Mutual coupling between DRAs was studied in [53]-[55], which demonstrates that the DRA technique can accommodate a parasitic element coupled to the driven element in both E and H planes. The configuration of the five-element ESPAR using DRAs is displayed in Figure 3. The DRA ESPAR cross array was shown to be able to achieve 2-D boresight beamsteering with wider impedance-matching FBW in [56]-[59]. Nevertheless, the element spacing in the E plane needs to be much larger than that in the H plane in order to achieve the proper phase shift; this reduces the energy coupled to the E-plane parasitic elements and ultimately compromises the antenna gain [57]. In addition, the beam squint performance was not directly reported for DRA ESPARs. However, the 3-dB gain FBW of 5.7% for a 240-element DRA ESPAR is much narrower than its impedance-matching FBW of 13.6% [58].

(a)

(b)
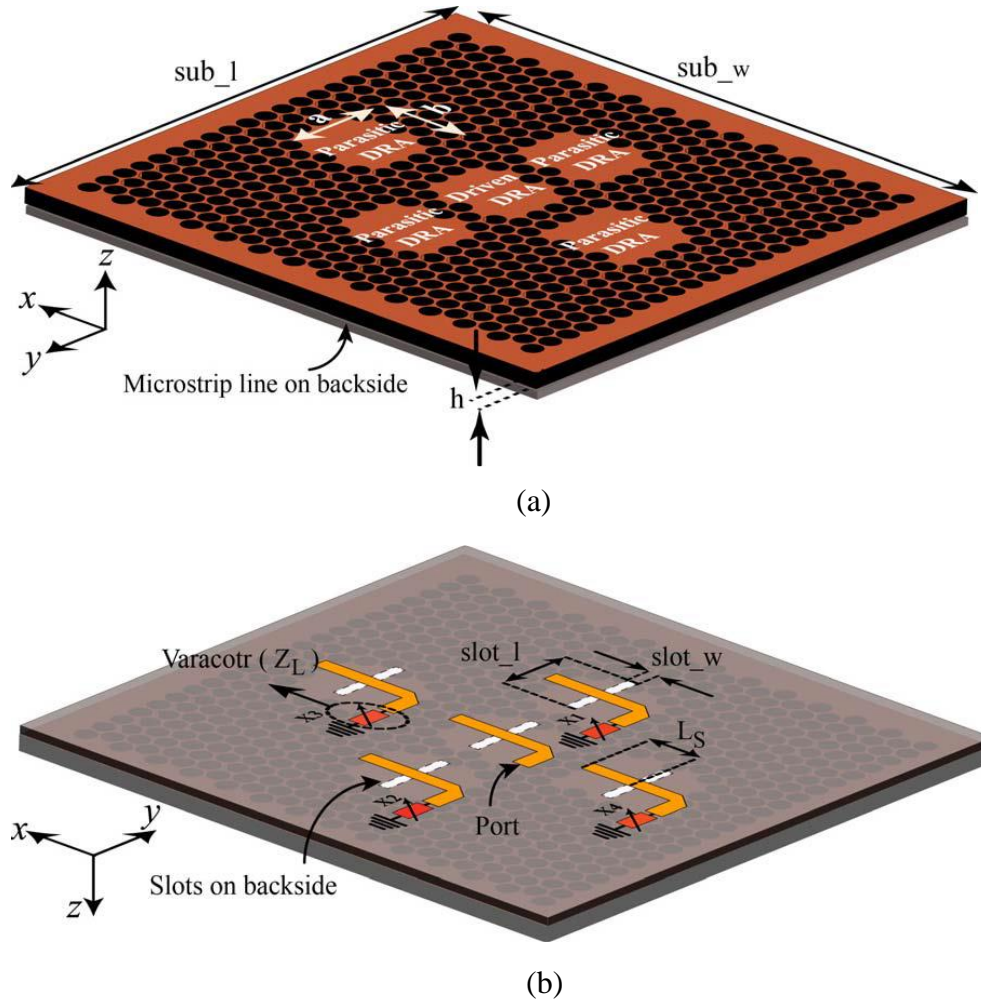
Figure 3: (a) Top and (b) bottom view of the five-element DRA ESPAR (reprinted from Movahedinia, Chaharmir, Sebak, Nikkhah, and Kishk (2017) [58]).

1.3.4   Cavity-Backed Slot ESPAR

Currently, the existing ESPARs have limitations in different aspects. In order to achieve a new ESPAR with 2-D beamsteering, large scan angles, wide FBW, high efficiency, and minimum beam squint, a 20-element cavity-backed slot (CBS) ESPAR is proposed in this dissertation as shown in Figure 4. The antenna array consists of four identical five-element cavity-backed slot ESPAR cross

9

subarrays. The beamsteering of the CBS ESPAR cross array is achieved by the tunable reactive loads on the parasitic elements, which reduces 80% of phase shifters compared to a conventional phased array. Since the mutual coupling between the cavities can be easily adjusted by the dimensions of the irises, the CBS ESPARs can achieve proper phase shifts in the E plane without the aforementioned element spacing issue of the DRA ESPARs, with the benefit of high antenna efficiency using substrate integrated waveguide (SIW) technology [60]-[62]. Additionally, several critical parameters are systematically studied to understand and optimize the beam squinting performance of the CBS ESPAR so that the useful operational FBW can match the S_{11} FBW. A comparison of ESPAR using different radiating elements is summarized in Table 1.

.
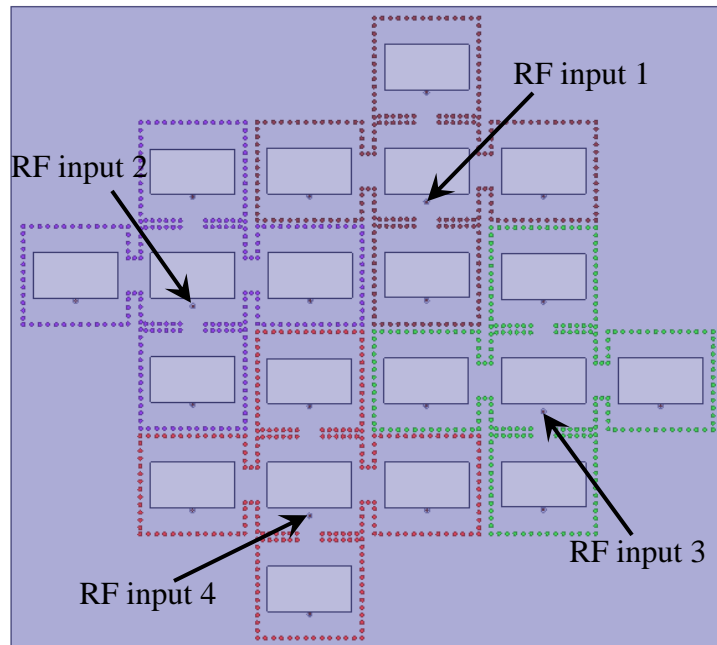
Figure 4: Proposed 20-element CBS ESPAR.

Table 1: Comparison of ESPARs with different radiating elements

	20-element CBS ESPAR	[46]	[58]
Radiating element	CBS	Patch	DRA
Beamsteering capabilities	2-D	1-D	2-D
PS reduction (%)	80	67	80
Center freq. (GHz)	6.2	1.0	10.5
Aperture size (λ_0^2)	$2.4 \times 2.6^*$	2.0×1.7	7.0×9.4
Gain (dBi)	14.0	12.1	22.4
Antenna efficiency (%)	85	N/A	56
Aperture efficiency (%)	32^*	38	20
Max. scan angles (deg.)	±45	±20	±25
Scan loss (dB)	1.5	0.5	0.5
S_{11} FBW (%)	6.4	1.0	13.6
3-dB Gain FBW (%)	6.4	1.5	5.7
Max. SLL (dB)	-10	-7	-10

*The aperture size is defined by the smallest rectangle that can include the 20 cavities. If the total area of 20 cavities is used as the aperture size, then the aperture efficiency increases to 58%.

1.4   Dissertation Outline

This dissertation explores the advantages of applying frequency-reconfigurable patch antenna and cavity-backed slot antenna techniques to ESPAR applications. Chapter 2 presents a frequency-reconfigurable microstrip patch ESPAR. Chapter 3 shows an ESPAR using CBS antennas in the E plane. A five-element CBS ESPAR cross array with 2-D beam steering is also discussed in this chapter. An approach to achieve enhanced FBW for the CBS ESPAR E-plane array is demonstrated in Chapter 4. In Chapter 5, the design details of the 20-element CBS ESPAR with 2-D beamsteering and minimized beam squint is presented. Finally, a summary and some future work, which can further enhance the FBW of the CBS ESPAR by using microstrip-line-fed cavity, are presented in Chapter 6.

CHAPTER 2   A FREQUENCY-RECONFIGURABLE MICROSTRIP

PATCH ESPAR

This chapter begins by presenting a microstrip patch ESPAR with continuous frequency reconfigurability. Similar to fixed-frequency ESPARs, only the driven element is fed by radio frequency (RF) power. The parasitic elements receive energy from the driven element through the mutual coupling, which can be controlled by varactors. By properly designing the mutual coupling level and adjusting the loading varactors on the parasitic elements, continuous beam steering can be realized. In addition, the return loss of this ESPAR can be maintained for all beam scanning angles since the mutual coupling is incorporated in the ESPAR design. In this work, loading varactors are strategically placed on the radiating edge of all antenna elements to achieve a 15% continuous frequency tuning range, while preserving all the aforementioned ESPAR features at each operating frequency. Therefore, this frequency-reconfigurable ESPAR is able to provide spectrum diversity in addition to the spatial diversity inherent in a frequency-fixed ESPAR. Herein, a low-cost microstrip patch ESPAR is demonstrated to operate from 0.87 to 1.02 GHz with an instantaneous fractional bandwidth of ~1%. At each operating frequency, this ESPAR is able to scan from -20 to 20 degree in H plane. The ESPAR gain and The input third-order intercept point (IIP$_3$) are also measured and presented here.

2.1   Introduction of the Patch ESPAR

Wireless communication systems and sensor networks have witnessed a rapid growth in the past decade. As a result, there are more and more wireless devices used in these systems. However, the

designated frequency spectrum is limited. The increasingly-crowded frequency spectrum hinders the implementation of next-generation communication systems and sensor networks. To resolve this challenge, millimeter-wave technology is exploited to provide larger bandwidth by operating at higher frequencies [63]-[66]. However, millimeter-wave signals exhibit higher path losses and are more susceptible to the terrain/building effects for wireless applications. It was reported that on average less than 15% spectrum was actually utilized from 450 to 2,700 MHz [67]. Therefore, it is of great importance to efficiently exploit this existing frequency spectrum which is more suitable for wireless applications within complex terrains.

In order to achieve this goal, the main communication system (primary user) should be able to allow other systems (secondary users) to access the licensed bands opportunistically and dynamically. The secondary users are required to sense the spectrum in real time and identify transmission opportunities, whenever the licensees (primary users) are not using their allocated spectrum. Typically, the instantaneous frequency bandwidth for various applications is relatively narrow. Therefore, a frequency-reconfigurable antenna is advantageous in that it can cover wide frequency range while maintaining a relatively narrow instantaneous bandwidth, by either discrete [68]-[70] or continuous [71]-[73] tuning mechanism. On the other hand, a beam-steerable antenna can boost the communication system capacity through the introduction of spatial diversity [74]-[76]. By combining both frequency and spatial diversity in the same device, the system capacity can be further improved. There has been a very limited number of works in this category [77]-[81]. Frequency-reconfigurable antennas with azimuth beamscanning capability were reported in[77], [78]. While frequency-agile antennas with beascanning capability at boresight were proposed in [79]-[81]. However, there are limited beam directions in [79], [80] while the frequency and spatial

14

diversity are not independent in [78] and [81]. It is highly desirable to realize a low-cost antenna with independent control on operating frequency and radiation pattern.

The Electronically-Steerable Parasitic Array Radiator (ESPAR) has been previously studied as an economic way to perform continuous beam steering using varactor diodes. This concept was first proposed in [27]. One of the original ESPARs was designed with seven monopole antennas [33]-[36] with azimuth beamscanning capability. Additionally, frequency-agile monopole ESPARs were demonstrated in [82] and [83] using a similar configuration. ESPARs employing dielectric resonator antennas (DRAs) were demonstrated to be able to scan the beam around boresight in both H and E planes [56]-[58]. Microstrip patch ESPARs with continuous beamscanning around boresight were presented in [42]-[46]. ESPARs exploiting inverted-F and inverted-L structures were also reported for cellphone applications in [84].

In this chapter, a three-element microstrip patch ESPAR with frequency reconfigurability is presented as shown in Figure 5. In order to achieve the frequency reconfigurability, each patch is loaded with a tunable capacitor on the radiating edge. These varactors are able to not only achieve the frequency reconfigurability but also realize beamscanning at each operating frequency. In comparison, the ESPAR design in [43], which is illustrated in Figure 6, contains no varactors on the radiating edge. It should be noted that there is no frequency reconfigurability in [43] due to the fact that the compensation varactors are placed on the non-radiating edges. In addition, the instantaneous bandwidth is narrow, approximately 1%, limiting the application of this antenna. The ESPAR presented in this chapter is able to tune the center frequency from 0.87 to 1.02 GHz,

15

which effectively covers 15 times of frequency spectrum compared to the one in [43]. In addition,

±20° continuous beam steering in H plane is realized at each operating frequency.
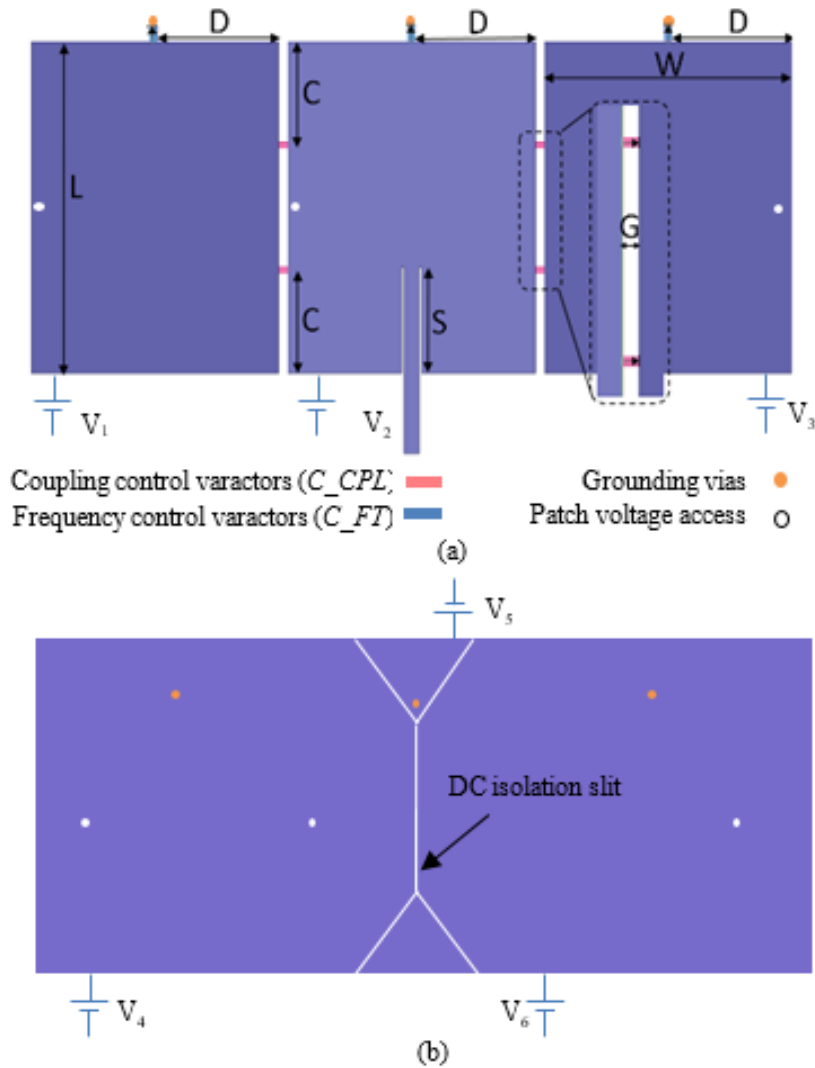
Figure 5: (a) Top layer of the frequency-reconfigurable ESPAR. Inset: zoomed-in view of the inter-element gap with coupling varactors. (b) Ground plane layer. (*L=97, D=38.5, C=31, S=31, W=77, G=3, Dimensions are in mm. Substrate thickness: 62 mil*)
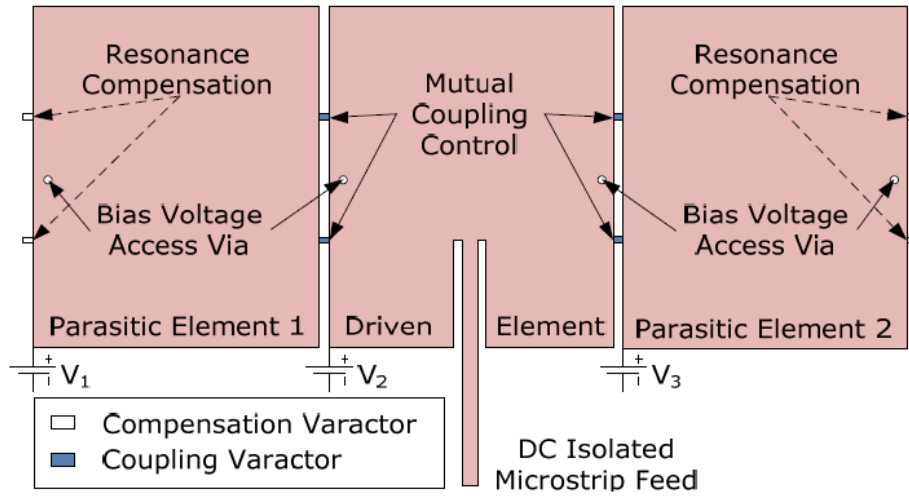
Figure 6: Single-layer microstrip patch ESPAR. (reprinted from Luther, Ebadi, and Gong (2012) [43])

This chapter is organized as follows. Section II describes the theory and design of the frequency-reconfigurable ESPAR antenna. Section III presents simulation results. Section IV provides the fabrication procedure and measurement results.

2.2   Antenna Theory and Design

2.2.1   Radiating Element Design

Single-layer inset-fed microstrip patch antenna is chosen as the radiating element designed on a 62-mil-thick Rogers RT/Duroid 5880 (ε_r=2.2, tanδ=0.0009) substrate. The driven element without varactor loading is initially designed to resonate at 5% higher than 1 GHz to compensate for the frequency downshift caused by the varactors. Two parasitic patches are symmetrically placed on both sides of the driven patch with a gap distance G. It should be noted that a smaller G can create stronger mutual coupling, which is beneficial for realizing larger beamscanning angles. However,

17

G = 3 mm is selected in this design to avoid the adverse effects from fabrication tolerances. In addition, a very small G can disturb the field distribution of the resonant patch, resulting in a higher cross-polarization level.

2.2.2   *Varactor Loading*

In order to reconfigure the resonant frequency of the ESPAR, each patch element is loaded with a frequency control varactor on its radiating edge. These varactors are placed in the middle of the radiating edge to maintain the symmetry, thereby minimizing the cross-polarization level. Two pairs of coupling control varactors are placed in the gap between the driven and parasitic elements to provide a stronger mutual coupling. In addition, it is noted that the phase shifts between the driven and parasitic elements are realized by these coupling control varactors rather than varactors loaded at the ports of the parasitic elements. Even though the coupling control varactors can provide stronger mutual coupling and larger phase shifts when they are placed closer to the radiating edges, a comprise needs to be made to avoid the disturbance of the field distribution of the natural resonant mode of the patch, which can deteriorate the radiation pattern and increase the cross-polarization level. When the coupling control varactors are tuned, the resonant frequency of each patch element is slightly modified. The frequency control capacitors on the parasitic elements can be adjusted accordingly to compensate for this frequency detuning and therefore maintain good impedance matching at all scan angles.
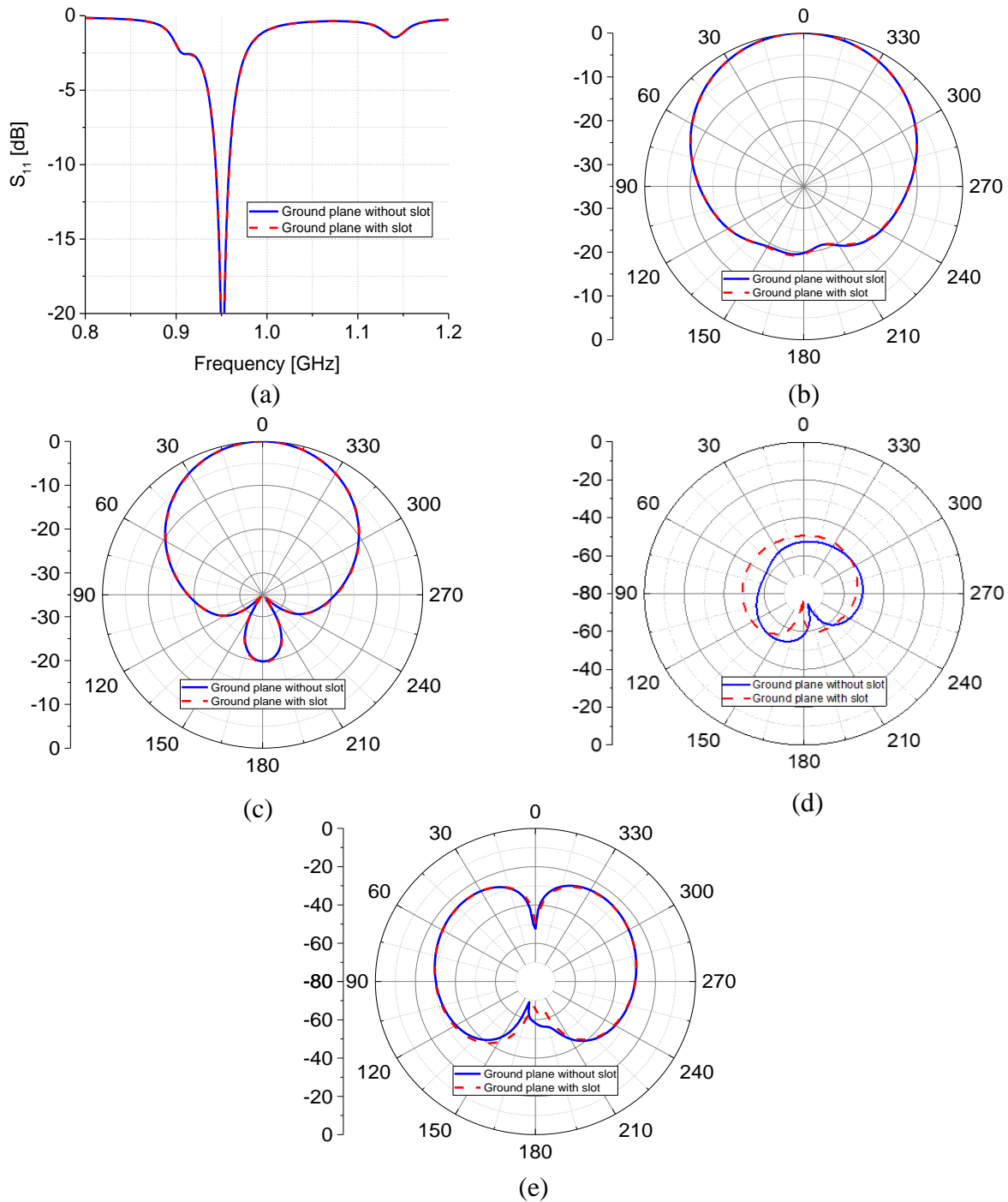
Figure 7: Simulated frequency-reconfigurable ESPAR with and without slot inside the ground plane for boresight radiation at 0.95 GHz. a) S11, b) E-plane Co-pol., c) H-plane Co-pol., d) E-plane X-pol., e) H-plane X-pol.

2.2.3 DC Biasing Network Design

In order to achieve independent control on the resonant frequency and coupling level, each frequency control varactor and each pair of coupling control varactors need to have their own bias voltage. As shown in Figure 5, the ground plane on the backside of the ESPAR is divided into four isolated regions by 6-mil-wide slots. To demonstrate the minimal impact of the slot inside the ground plane, the simulated S11 and boresight radiation patterns at 0.95 GHz with and without the slot are compared in Figure 7. The difference between the two cases is negligible. The coupling control varactors are biased by V_1-V_2 and V_3-V_2, respectively. The frequency control varactors are tuned by V_4-V_1, V_5-V_2, and V_6-V_3, respectively, from left to right in Figure 5. The bias voltages on the patches are provided by drilling 500-μm-diameter holes (patch voltage access) as shown in Figure 5 and connecting the patches to individual voltage supplies using insulated wires. The location of the patch voltage access is selected in the middle of the non-radiating edge where the electric field is minimum (virtual ground), which exhibits the least amount of adverse effects on RF performance. Three grounding vias are fabricated to connect the frequency control varactors to their respective ground plane section.

2.3   Design Procedure and Simulation Results

The frequency-reconfigurable ESPAR shown in Figure 5 is simulated using ANSYS High Frequency Structure Simulator (HFSS). Varactors are modeled by a lumped-element series RC network. The resistance for the varactor is set to be different values corresponding to various capacitance, which is extracted from the measurement results in the varactor datasheet. It is observed in Figure 8 that the varactor-loaded patch antenna is able to tune its center frequency

from 0.87 to 1.02 GHz. In order to quickly identify the desired coupling control capacitance combination for a certain beamscanning angle, the relationship between the coupling control capacitance and induced currents on the parasitic patches can be calculated from the Z-matrices of the frequency-reconfigurable microstrip patch ESPAR. A modified ESPAR structure with three ports as shown in Figure 9 is used to extract the Z-matrices. To validate the equivalency of the modified structure, the simulated H-plane radiation patterns for different beamscanning cases at 1 GHz are compared with the structure shown in Figure 5. It should be noted that the coupling control capacitors (C_CPL1 and C_CPL2) are set to be identical in both designs while the frequency tuning capacitors are slightly adjusted to maintain the same resonant frequency. It is observed in Figure 10 that the main lobes of both cases closely match each other while the side lobe levels are slightly different for some beamscanning cases. Therefore, it can be concluded that the modified structure is able to accurately predict the radiation direction with the capability of providing Z-matrices. With the help of the Z-matrices, the ratio of currents between the parasitic patches and the driven patch can be analytically analyzed as shown below.

$$\begin{bmatrix} Z_{11} & Z_{12} & Z_{13} \\ Z_{21} & Z_{22} & Z_{23} \\ Z_{31} & Z_{32} & Z_{33} \end{bmatrix} \begin{bmatrix} I_1 \\ I_2 \\ I_3 \end{bmatrix} = \begin{bmatrix} V_1 \\ V_2 \\ V_3 \end{bmatrix} \tag{1}$$

$$V_2 = -I_2 Z_{T2}, V_3 = -I_3 Z_{T3} \tag{2}$$

After applying the boundary conditions defined by V_2 and V_3, the current ratios can be found with (3) and (4).

$$\frac{I_2}{I_1} = \frac{(Z_{13}*Z_{23}) - Z_{12}*(Z_{33} + Z_{T3})}{-Z_{23}^2 + Z_{22}*Z_{33} + Z_{22}*Z_{T3} + Z_{33}*Z_{T2} + Z_{T2}*Z_{T3}} \tag{3}$$

21

$$\frac{I_3}{I_1} = \frac{(Z_{12}*Z_{23})-Z_{13}*(Z_{22}+Z_{T2})}{-Z_{23}^2+Z_{22}*Z_{33}+Z_{22}*Z_{T3}+Z_{33}*Z_{T2}+Z_{T2}*Z_{T3}} \qquad (4)$$

Finally, the array factor of the ESPAR can be calculated using (5):

$$AF = 1 + \left|\frac{I_2}{I_1}\right| e^{-jkd\cos\theta + ang\left[\frac{I_2}{I_1}\right]} + \left|\frac{I_3}{I_1}\right| e^{+jkd\cos\theta + ang\left[\frac{I_3}{I_1}\right]} \qquad (5)$$

In which, k is the wavenumber and d is the center-to-center distance between antenna elements. Z_{T2} and Z_{T3} are infinite at the ports on the parasitic patches, therefore, a different reference plane as shown in Figure 9 needs to be chosen in order to provide correct results using (3) and (4). As a result, the corresponding Z-matrices for different coupling control capacitance can be extracted from the modified structure to predict the radiation pattern instead of using the electric field from full-wave simulations, which can significantly reduce the design time.
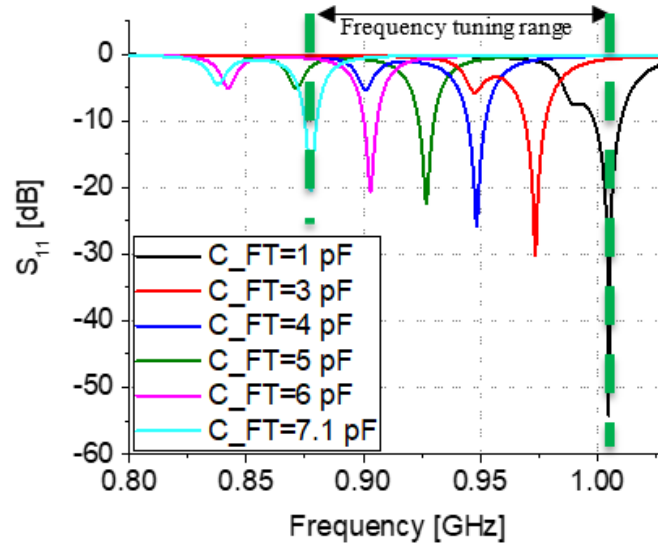
Figure 8: S_{11} vs. frequency control capacitance on the driven element for boresight radiation.
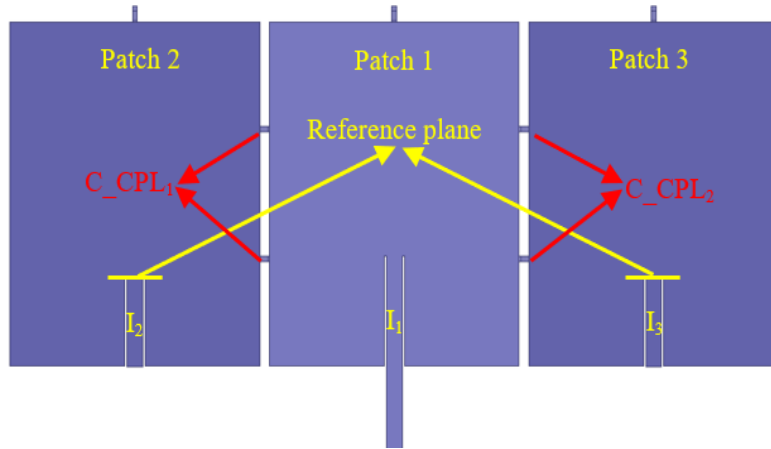
Figure 9: Schematic of the modified ESPAR structure.

(a)

(b)

(c)
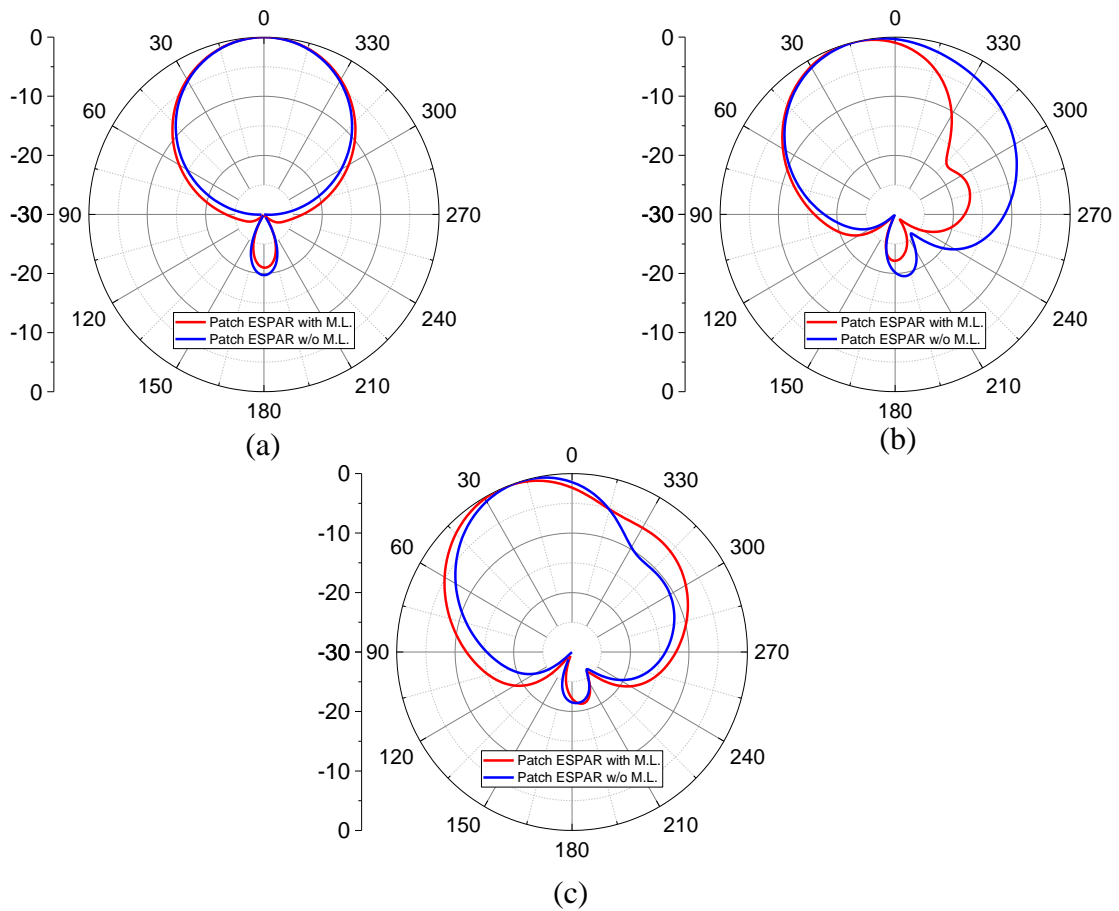
Figure 10: Simulated H-plane Co-pol. of frequency-reconfigurable ESPAR with and without microstrip line loading on the parasitic patches for a) 0°, b) 18°, and c) 24° beamscanning at 1.00 GHz.

For boresight radiation, the four coupling control capacitances are set to be identical. By adjusting *C_CPL1* and *C_CPL2* simultaneously, the relationship between the induced current and driven current vs. different coupling control capacitances from 0.5 to 4.5 pF at 1.00 GHz is displayed in Figure 11. It is observed that magnitude of the induced current on the parasitic patches increases as the coupling control capacitance increases. Meanwhile the phase difference between the induced current and driven current decreases from 175º to 25º as the *C_CPLs* increase from 0.5 to 2.0 pF. When the *C_CPLs* keep increasing beyond 2.0 pF, the phase difference stays around 0º. It can be quickly identified that 4.5 pF is the optimum coupling control capacitance for the boresight radiation by considering both the desired phase difference and uniform magnitude distribution.
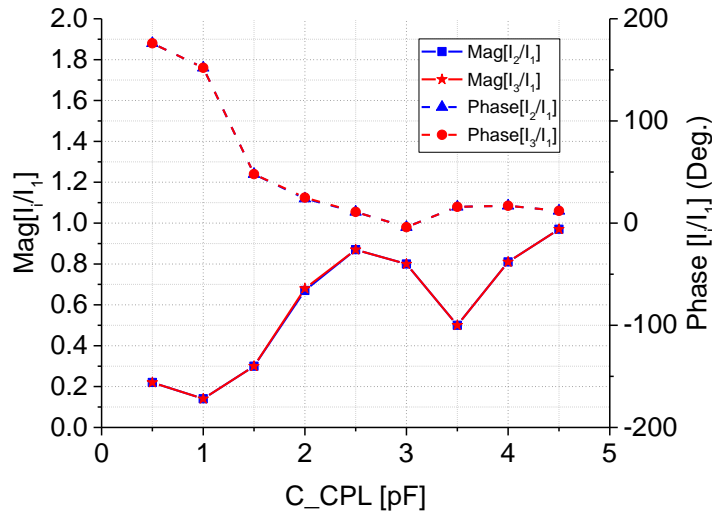
Figure 11: The magnitude ratio and phase difference between the induced currents and driven current vs. *C_CPL(C_CPL1=C_CPL2)*.

In order to investigate the beamscanning capability, the phase tuning range provided by the coupling control capacitors can be obtained by sweeping *C_CPL1* from 0.5 to 4.5 pF while the *C_CPL2* is fixed at 3.0 pF. The corresponding calculation results of the current ratios are displayed

in Figure 12. It is observed that the phase difference between patch 2 and patch 1 can be tuned from -50° to 175°. However, the -50° to 0° tuning range is not useful due to the small induced current magnitude on Patch 2. Since the *C_CPL2* is fixed at 3.0 pF all the time, the phase difference between Patch 3 and Patch 1 is maintained around 0°. To perform the beamscaning, it can be quickly calculated from the array factor that 152° phase difference is required for 24° beamscanning in the H plane. According to Figure 12, the corresponding phase difference can be achieved when *C_CPL1* equals to 1.7 pF. In order to find the optimum value of *C_CPL2*, a second simulation is performed where the *C_CPL2* is swept from 0.5 to 4.5 pF meanwhile the *C_CPL1* is fixed at 1.7 pF. It is noted in Figure 20 that only -60° phase difference can be reached for the negative phase difference. Moreover, the induced current magnitude is extremely low on Patch 3 at -60-degree phase difference due to the small value of *C_CPL2*. Therefore, *C_CPL2*=3.5 pF is found to be the optimum coupling control capacitance by considering both the phase difference and uniform magnitude distribution. As for the 18° beamscanning in the H plane, 74° phase difference is desired. Therefore, *C_CPL1* is found to be 2.0 pF from Figure 12. Similar simulations are performed by sweeping *C_CPL2* meanwhile *C_CPL1* is fixed at 2.0 pF. It can be easily found in Figure 14 that *C_CPL2*=3.0 pF is the optimum value for 18° beamscanning in the H plane. The same method can be applied to any combination of operating frequency and beamscanning angle.

The H-plane Co-pol. radiation patterns for different beamscaninng cases at 1.00 GHz can be calculated by multiplying the array factor and element radiation pattern as shown in Figure 15. There is a slight deviation (< 2°) from the designed main lobe direction. Therefore, the coupling control capacitances are further optimized to align the main lobe to the designed directions. The final values of all the capacitances are listed in Table 2. The radiation patterns using optimized

capacitance values and full-wave HFSS simulations are also shown in Figure 15. A lookup table like Table 2 can be created for this frequency-reconfigurable microstrip patch ESPAR.
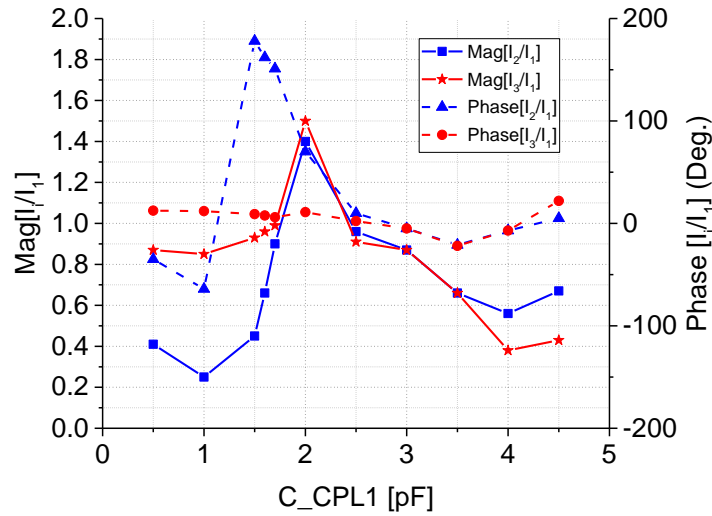
Figure 12: The magnitude ratio and phase difference between the induced currents and driven current vs. *C_CPL1* (C_CPL2=3.0 pF).
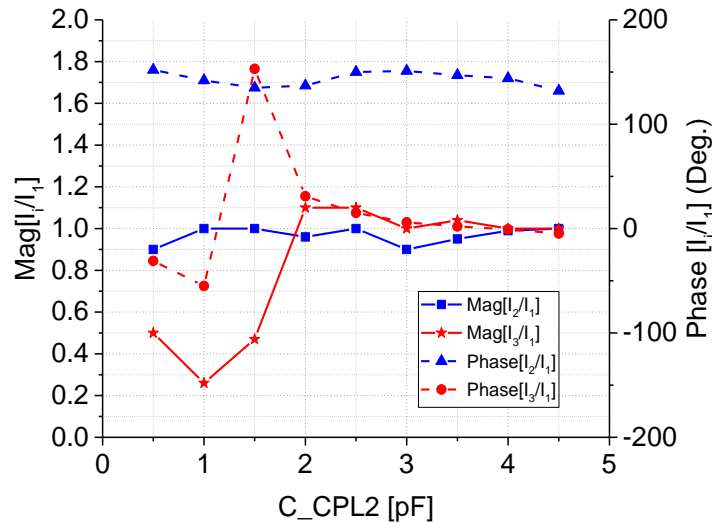
Figure 13: *The magnitude ratio and phase difference between the induced currents and driven current vs. C_CPL2 (C_CPL1=1.7 pF).*
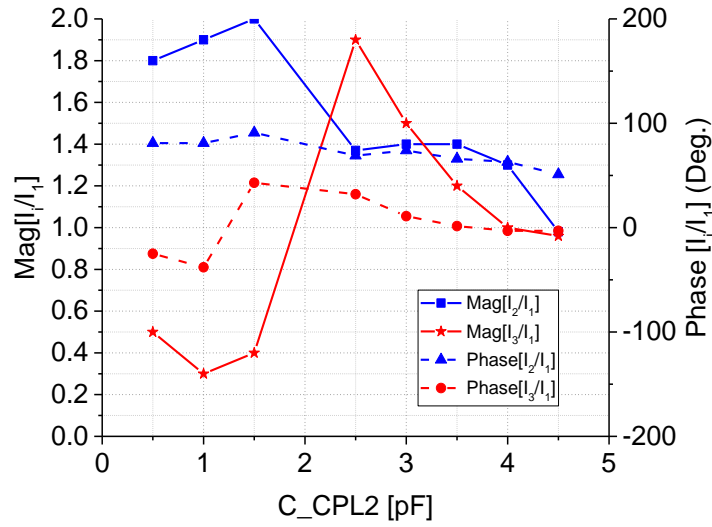
Figure 14: The magnitude ratio and phase difference between the induced currents and driven current vs. *C_CPL2* (C_*CPL1=2.0 pF*).

(a)

(b)

(c)
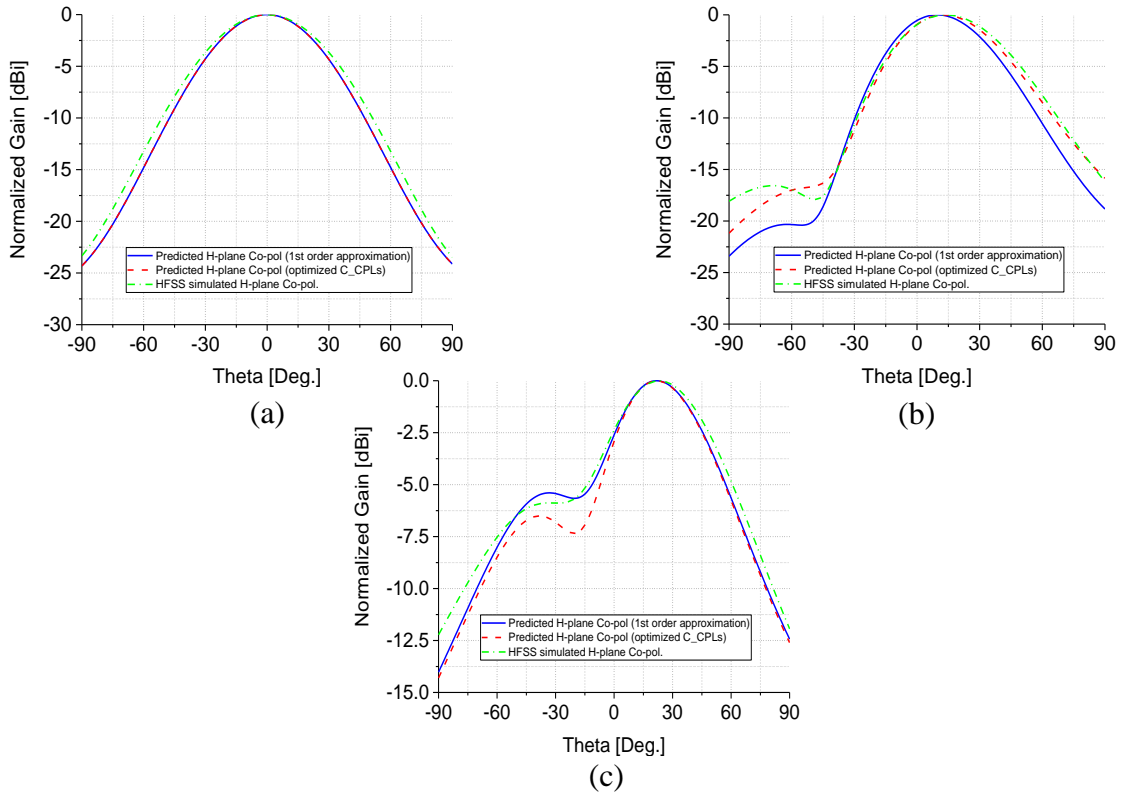
Figure 15: Predicted and simulated H-plane Co-pol. of frequency-reconfigurable patch ESPAR for a) 0° b) 18°, and c) 24° beamscanning at 1.00 GHz.

Table 2: Frequency-Reconfigurable ESPAR Design Table

Scan Angle [Deg.]	Gain and Varactor Values at Resonant Frequency of 0.92 GHz					
	Gain [dBi]	C_CPL1 [pF]	C_CPL2 [pF]	C_FT1 [pF]	C_FT2 [pF]	C_FT3 [pF]
0	0.72	3.5	3.5	6.5	4.5	6.5
10	0.2	2.5	4	4.5	5	6.5
20	-0.86	2.5	3.5	4.5	4.5	6.5
	Gain and Varactor Values at Resonant Frequency of 0.95 GHz					
0	3.80	3	3	5	3.3	5
10	3.0	2	4	3.8	3.4	5
20	1.87	2.5	4	3.3	2.8	5
	Gain and Varactor Values at Resonant Frequency of 1.00 GHz					
0	8.13	4.5	4.5	1.8	0.8	1.8
18	7.83	1.7	2.2	0.8	1	1.2
24	7.54	1.7	3	0.8	1	1.2

2.4   Fabrication and Measurement results

The frequency-reconfigurable ESPAR is fabricated on a 62-mil-thick Duroid 5880 substrate as shown in Figure 16 using standard PCB fabrication process. Infineon BB837 silicon tuning diode is used with a tuning range of 0.52-6.6 pF. The three-varactors grounding vias are copper electroplated. Three insulated bias wires are placed inside three small holes (not electroplated) and

soldered to the microstrip patches. To facilitate antenna pattern measurement in the anechoic chamber, a mounting bracket is made by a 3D printer and held on the backside of the ESPAR.
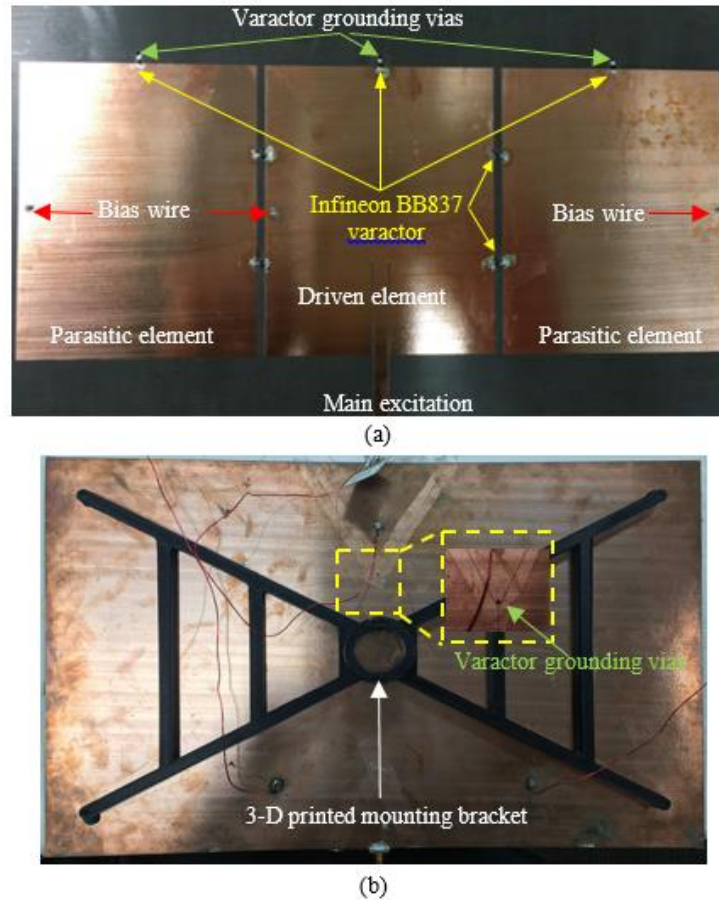
Figure 16: (a) Top and (b) bottom side of frequency-reconfigurable ESPAR.

The S_{11} corresponding to different beamscanning angles at the resonant frequency of 0.92, 0.95 and 1.00 GHz, respectively, is measured by an Agilent N5230A network analyzer and shown in Figure 17. Overall, the measured S_{11} matches the simulation except for some additional resonances outside the operating bandwidth. Moreover, it is observed that the S_{11} is maintained at different beamscanning angles for all resonant frequencies of the frequency-reconfigurable ESPAR.
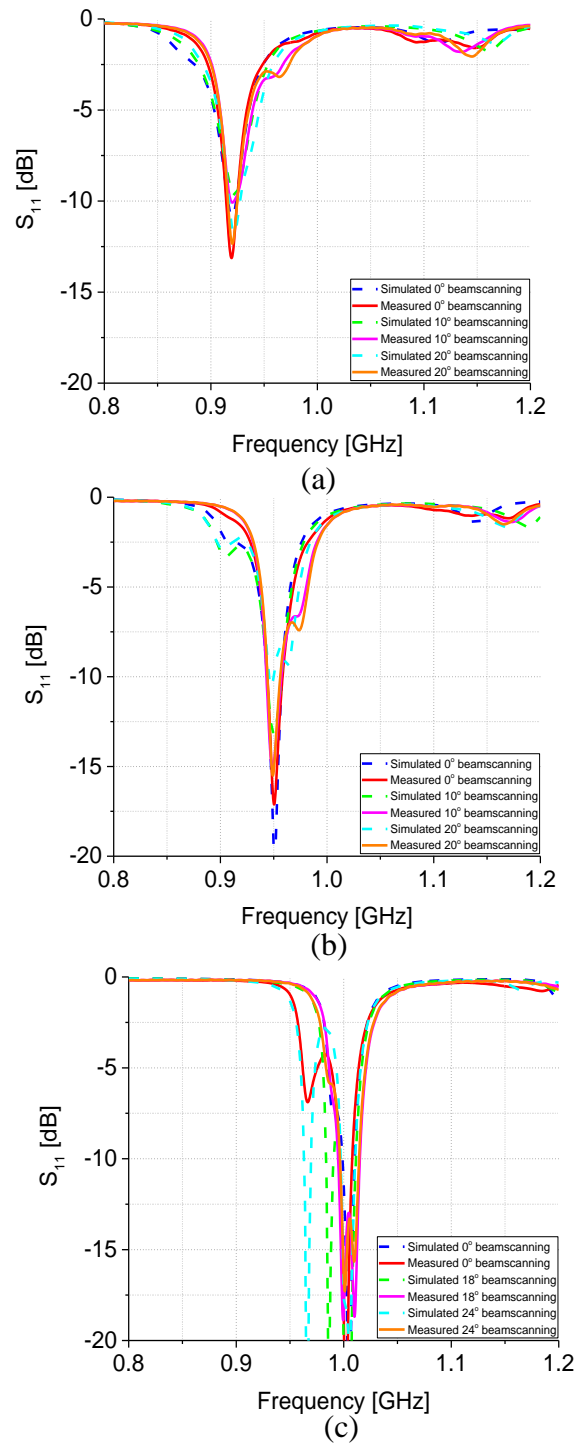
Figure 17: Simulated and measured S_{11} for different beamscanning angles at resonant frequency of (a) 0.92, (b) 0.95, and (c) 1.00 GHz, respectively.

The simulated and measured H-plane radiation patterns are compared from Figure 18 to Figure 20 for both co-pol. and cross-pol. Again, the agreement between the two is apparent. The measured cross-pol. level is less than -13 dB for all the cases. The measured backside lobe is below -13 dB for all the cases as well. The frequency-reconfigurable ESPAR presented in this chapter exhibits H-plane beamscanning capability only. When the beam scans in the H plane, the radiation pattern in the E plane maintains the same shape as shown in Figure 21. It is noted that the cross-pol. level is slightly larger in the E plane due to the asymmetric loading of the frequency-control varactors.
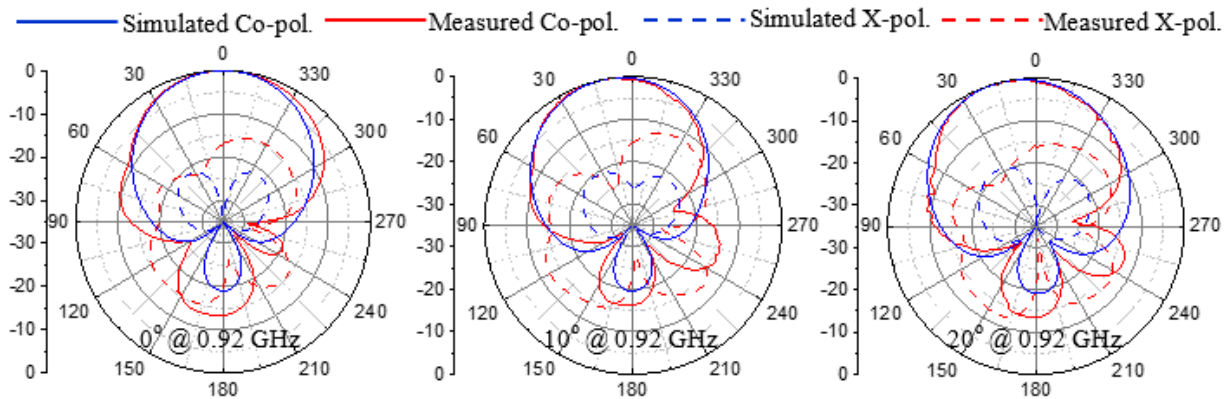
Figure 18 : Normalized H-plane radiation patterns for different beam scan angles at resonant frequency of 0.92 GHz.

The ESPAR gain at boresight vs. frequency for resonant frequencies of 0.92, 0.95 and 1.00 GHz, respectively, are plotted in Figure 22. The measured peak gain increases from -1.08 to 7.46 dBi when the frequency-reconfigurable ESPAR is tuned from 0.92 to 1.00 GHz. In HFSS simulations, the effective series resistances (ESRs) of the varactors are considered. These resistance values are extracted from the measured results of the Infineon BB837 varactor and found to be 3.15 ohm (0.92 GHz), 3.12 ohm (0.95 GHz), and 1.5 ohm (1.00 GHz), respectively. The discrepancies

between simulated and measured peak gains, particularly at lower resonant frequencies, are

possibly due to extra losses inside the varactors and interconnects which are unaccounted for.
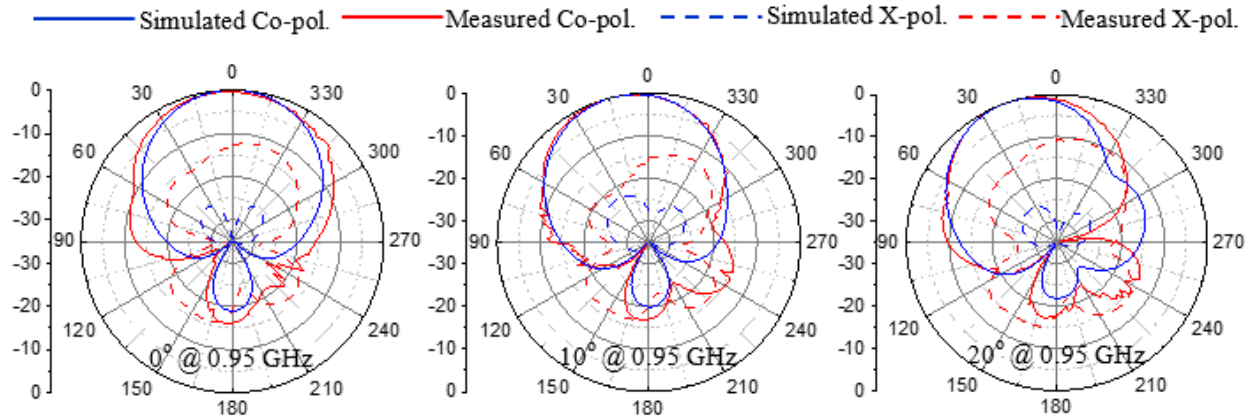
Figure 19: Normalized H-plane radiation patterns for different beam scan angles at resonant frequency of 0.95 GHz.
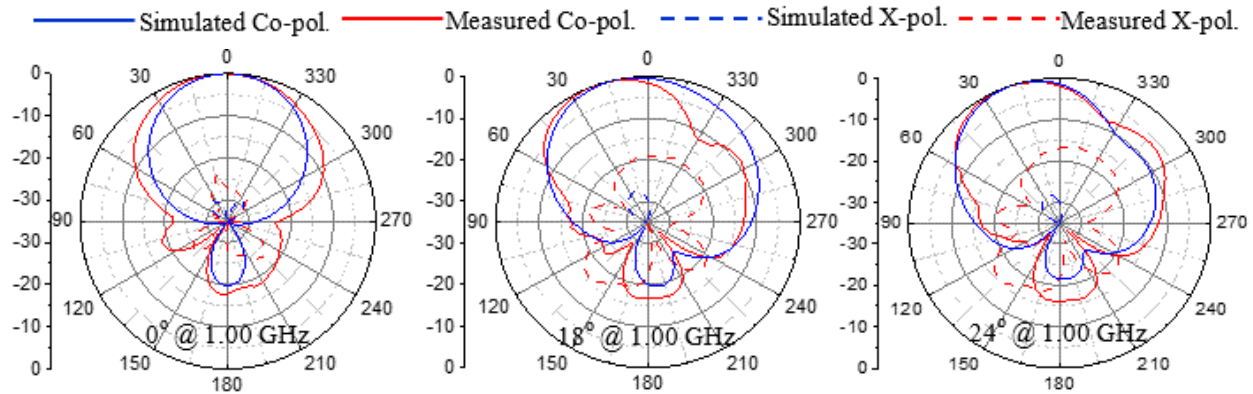
Figure 20: Normalized H-plane radiation patterns for different beam scan angles at resonant frequency of 1.00 GHz.

In order to understand how losses inside varactors reduce the antenna gain, HFSS simulations are

performed for the boresight radiation case where the ESR of the varactor is set to 0 ohm. The

realized gain at 1.00 and 0.92 GHz is found to be 8.82 and 8.28 dBi, respectively. This 0.54 dB

(8.82-8.28) reduction in gain can only be attributed to the reduced electrical size when the antenna

is reconfigured from 1.00 to 0.92 GHz. When the ESRs are set to be 1.5 ohm for 1 GHz operation or 3.15 ohm for 0.92 GHz operation, the simulated gain at 1.00 GHz and 0.92 GHz is found to be 8.13 and 0.72 dBi, respectively. It is found that at 1 GHz operation, the 1.5-ohm ESR caused a 0.69-dB (8.82-8.13) reduction in gain compared with the lossless varactor case. While at 0.92 GHz operation, the reduction in gain compared with the lossless varactor case is 7.56 dB (8.28-0.72), which is from the varactor loss (3.15 ohm ESR) at 0.92 GHz. To better understand the effect of ESR on the antenna efficiency of the ESPAR, full-wave simulation results are provided in Table 3. Therefore, high-Q varactors based on GaAs diodes or Micro-Electrical-Mechanical-System (MEMS) technology have great potentials to improve the antenna gain significantly. The antenna gain of this ESPAR is relatively low when the center frequency is below 0.95 GHz. However, the agility in both frequency and beam of this ESPAR is still critical in many modern communication and sensor systems in which a large spectrum is shared. There are many unlicensed commercial systems that are currently operating at low power levels over a spectrum that is already overcrowded, as shown in the United States Federal Communication Commission (FCC) Part 15 rules [85]. Even though each user uses a narrowband signal, however, this narrowband interference (NBI) significantly increases the bit-error probability (BEP) for other users who are using the same spectrum [86]. The proposed ESPAR is able to use the frequency agility to mitigate this NBI when the spatial diversity is impossible, i.e. the interference signal is from the same direction as the desirable communication links. When more and more wireless devices are connected in the future, this NBI issue becomes increasingly severe.

Table 3: Frequency-Reconfigurable ESPAR Radiation Efficiency vs. ESRs of the varactor

Efficiency	ESR in the varactor equivalent circuit [ohm]					
Freq. [GHz]	0.5	1.0	1.5	2.0	2.5	3.0
0.92	48.9%	37.1%	30.0%	24.7%	21.1%	18.6%
0.95	62.4%	53.1%	45.7%	40.1%	35.6%	31.7%
1.00	81.6%	79.8%	77.5%	75.3%	73.3%	71.6%
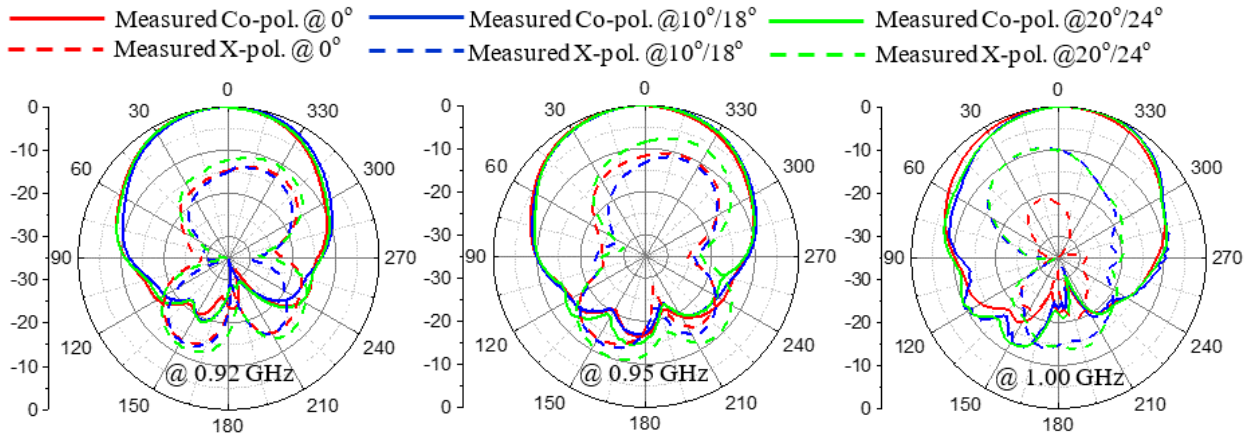
Figure 21: Normalized E-plane radiation patterns for different beam scan angles at resonant frequency of 0.92, 0.95, and 1.00 GHz, respectively.

The gain vs. scan angle for several resonant frequencies are shown in Figure 23. The scan losses for 0.92, 0.95 and 1.00 GHz from boresight to maximum scan angles are 1.92, 1.55 and 0.6 dB, respectively. The summary of the simulated and measured gains as well as simulated radiation efficiency is shown in Table 4.

34
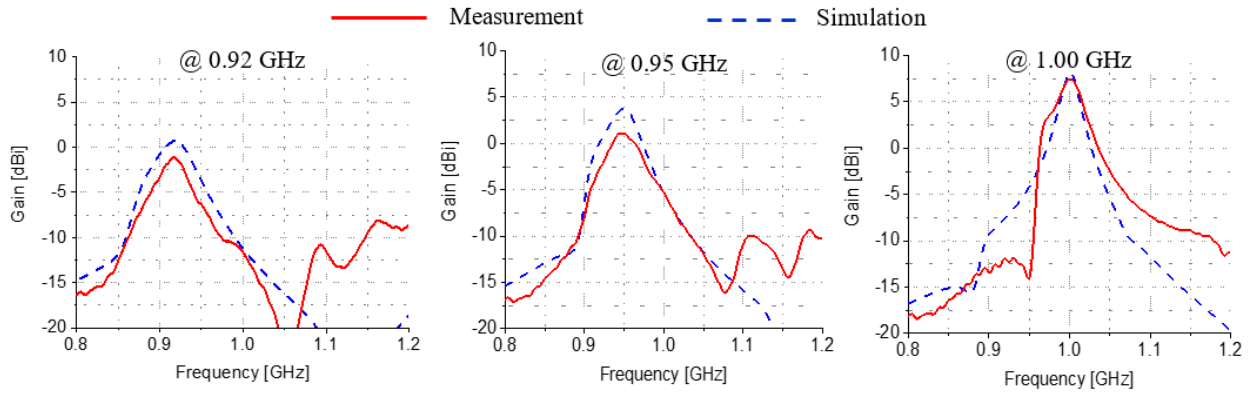
Figure 22: Gain vs. frequency at resonant frequency of 0.92, 0.95, and 1.00 GHz, respectively for boresight radiation.

Table 4: Simulated/Measured Gain and Simulated Radiation Efficiency

Scan Angle [Deg.]	Resonant Frequency of 0.92 GHz		
	Simulated Gain [dBi]	Measured Gain [dBi]	Radiation Efficiency
0	0.72	-1.08	18.36%
10	0.20	-1.36	17.36%
20	-0.86	-3.0	13.34%
	Resonant Frequency of 0.95 GHz		
0	3.8	1.1	31.56%
10	3.0	0.83	26.11%
20	1.87	-0.45	21.88%
	Resonant Frequency of 1.00 GHz		
0	8.13	7.46	77.5%
18	7.83	7.36	62.50%
24	7.54	6.86	62.03%
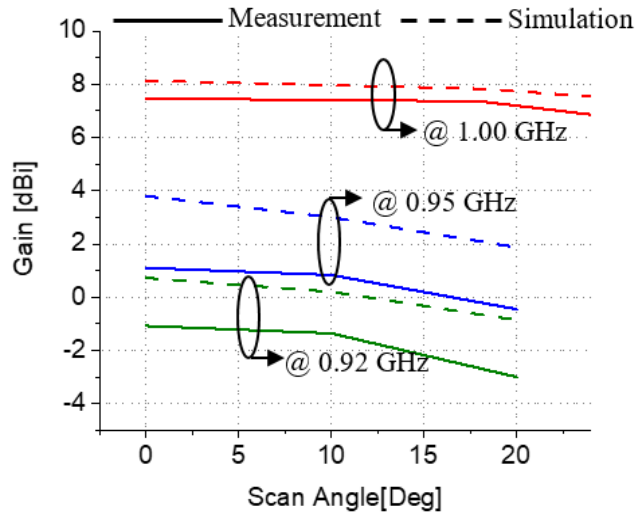
Figure 23: Simulated and measured gain vs. beam scan angle at resonant frequency of 0.92, 0.95, and 1.00 GHz, respectively.
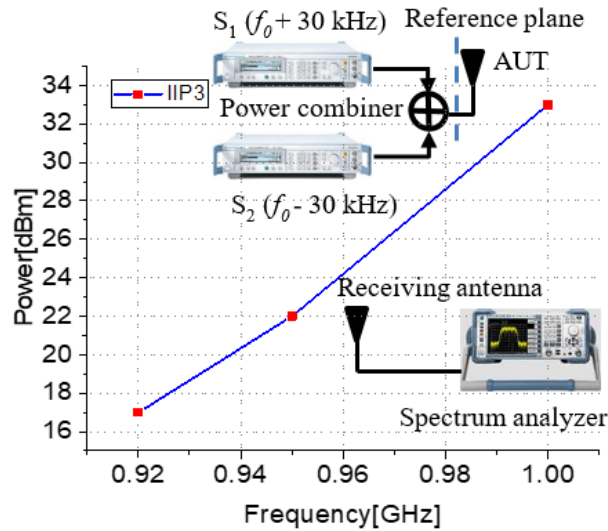
Figure 24: Measured IIP$_3$ at boresight vs. frequency.

The IIP$_3$ of the frequency-reconfigurable ESPAR is characterized using the measurement setup in

Figure 24 for boresight radiation cases at 0.92, 0.95 and 1.00 GHz, respectively. The frequency

difference between the two tones is set to be 60 kHz. The IIP$_3$ is 17 dBm at 0.92 GHz and 33 dBm

at 1.00 GHz. At lower resonant frequency, the nonlinearity performance is worse since larger

varactor values correspond to lower DC bias voltages. The IIP$_3$ performance of this ESPAR is better than that of the slot-ring antenna using similar semiconductor varactors [47], i.e. 30 dBm for the highest frequency operation (low capacitance) and -6 dBm for the lowest frequency operation (high capacitance).

2.5   Conclusion

A novel inexpensive frequency-reconfigurable microstrip patch ESPAR has been designed, fabricated and measured. This ESPAR exhibits 15% frequency tuning range. At any resonant frequency, this ESPAR can scan beam up to at least ±20 degree while maintaining good impedance matching. This frequency-reconfigurable ESPAR approach can significantly extend the useful frequency range from a fixed-frequency ESPAR, thereby increase the capacity of communication systems by providing both frequency and spatial diversity.

However, the efficiency of the frequency-reconfigurable ESPAR degraded due to the increased loss from the varactors at lower frequency operation. In addition, since it is difficult to control the mutual coupling in the E plane, the beamsteering of the patch ESPAR is limited in the H plane only. Because of the advantages in high antenna efficiency and ease of mutual coupling control, the CBS antenna are studied in the next chapter as a promising solution to improve the antenna efficiency and realize 2-D beamsteering

CHAPTER 3   CAVITY-BACKED SLOT (CBS) ESPAR E-Plane Array

The frequency-reconfigurable patch ESPAR presented in Chapter 2 can tune continuously over a frequency range from 0.92 to 1.05 GHz. In addition, the beamsteering ability is preserved at each operating frequency. However, the bandwidth of the patch ESPAR is very narrow (~1%) and its beamsteering is limited in the H plane only. In order to achieve E-plane beamsteering, an ESPAR using cavity-backed slot (CBS) antennas is introduced in this chapter. After that, a CBS ESPAR using wider slot and thicker substrate is designed to further extend the operational bandwidth of the CBS ESPAR.

As with conventional ESPAR antennas, the parasitic cavities are fed by mutually coupling to the center cavity and each parasitic cavity is terminated with a tunable capacitor that provides the necessary phase shift for the desired beam scanning performance. Due to the difficulty of achieving E-plane coupling while simultaneously controlling the coupling level and phase, there have been few reported E-plane ESPAR antennas in the literature. In this chapter, it is shown that these challenges can be overcome by exploiting the cavity geometry to achieve the desired coupling values; the required phase shift is achieved by changing the load impedance of the parasitic cavities. In full-wave simulations, it is observed that the proposed ESPAR E-plane array is able to steer the beam from -30 to 30 degrees, which is comparable to the beam-steering range of ESPAR antennas operating in the H-plane.

In addition, a CBS ESPAR using thick substrate and wide slot is fabricated and measured to extend impedance-matching FBW of a single CBS antenna to 6.0%. Moreover, it is found that a tunable

load which uses a fixed inductor, a varactor, and a delay line can provide a much larger impedance tuning range compared to that without the inductor. This tunable load is critical to enhance the FBW by considering beam squinting. The three-element ESPAR in this chapter is able to scan from -26 to 20 degrees in the E plane, operating around 5.15 GHz. The measured peak gain is between 5.52 and 6.05 dBi at all scan angles. The radiation patterns are measured at different scan angles in E plane. In addition, they are measured at different frequencies to demonstrate the beam squinting performance.

3.1   Introduction of the CBS ESPAR E-plane Array

Phased arrays are commonly used for satellite communication due to their outstanding beam steering performance [87], [88]. However, the required phase shifters and T/R modules are very expensive and usually take 50% of the total fabrication cost, which prevents phased arrays from being used for commercial applications. As modern wireless communications systems move forward, employing beam steerable antennas can improve the spectrum usage efficiency compared to omnidirectional antennas. Additionally, being able to scan a highly directional beam can help the system avoid noisy environment or line-of-sight issues; the system efficiency is significantly improved by the higher SNR and signal quality. As a result, a low-cost beam steerable antenna is desirable for commercial communication applications. Herein, the ESPAR antenna is introduced as a practical alternative to achieve phased array beam steering. Since the phase shifts are implemented using commercially available tunable capacitors instead of phase shifters, the fabrication cost is significantly reduced.

Most current planar microstrip patch ESPAR designs are limited to only H-plane coupling due to the difficulty of introducing and controlling the E-plane coupling level and phase [42]-[46]. To tackle these challenges, a new coupling method and antenna design are needed to preserve the radiation performance while achieving the desired E-plane coupling.

In this chapter, a three-element cavity-backed slot ESPAR E-plane array is presented. Unlike conventional phased arrays, only the center driven element is fed with RF power and all of the parasitic elements are fed by the driven element through mutual coupling. By properly designing the loading varactor (C_{Ti}) as shown in Figure 25, the required phase shift can be obtained for different beam scanning cases. It is noted that the H-plane radiation pattern is fixed at 0 degrees when the beam scans from -30 to 30 degrees in the E-plane.
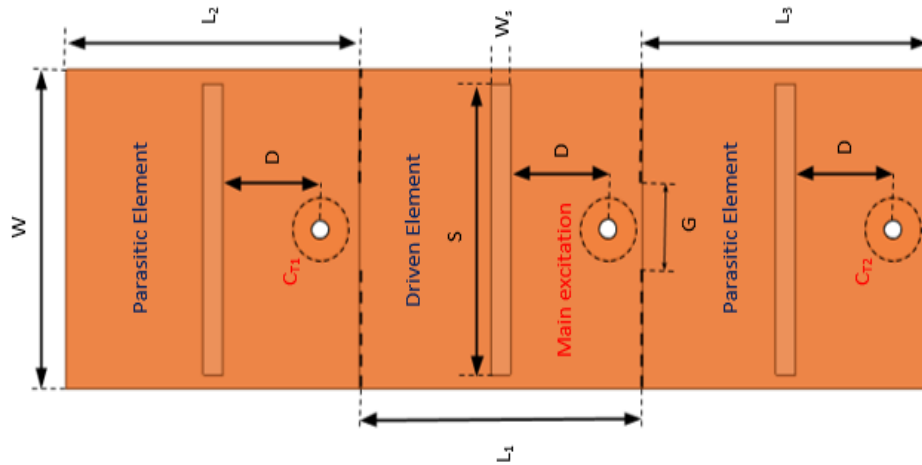
Figure 25: Schematic of the cavity-backed slot ESPAR cross array. *L_1=22, L_2=22.75, L_3=22.25, W=22, Ws=1.5, S=20, D=7.59, G=4. All dimensions are in mm.*

This proposed ESPAR array achieves E-plane beam steering performance comparable to patch ESPARs operating in the H-plane; it also provides E-plane beam steering capability on par with

planar ESPAR designs without sacrificing simultaneous H- plane beam steering. Additionally, this array can readily be extended to a full-scale array.

3.2 CBS Antenna Design

The three-element cavity-backed slot ESPAR E-plane array is designed on a 100-mil-thick Rogers RT Duroid 6006 (ε_r=6.15, tanδ=0.0019) substrate. The high dielectric constant material is used to reduce the antenna spacing, which eliminates grating lobes. As shown in Figure 25, the driven element is initially designed to resonate at 4.1 GHz and an SMA cable is used to feed the cavity with the center pin touching the cavity's bottom surface. Similar parasitic cavities are placed along the E-plane and receive the energy from the center driven element through coupling irises. The cavity sizes are made to be asymmetric to compensate for the off-center position of the feeding probe; modifying the cavity sizes individually also allows for control of the resonant frequencies. The radiating slots are etched at the center of the top of each cavity and the tuning varactors C_T are loaded on each parasitic cavity at the same location as on the driven cavity to achieve a maximum tuning range. By varying the capacitance C_T, both the coupling level and the phase can be changed to achieve the desired beam steering angles in the E-plane. Since the tuning capacitor is directly connected to the cavity and isolated from the slot antenna, the slot resonance is unaffected by different terminating capacitances.

3.3 Current Ratio between Parasitic and Driven Elements

This ESPAR can be modeled as a three-port reciprocal network with the reference planes shown in Figure 25. The Z matrix of the ESPAR can be extracted from ANSYS HFSS simulations, as described in [42]. Therefore, the currents at the three reference planes can be related using (6).

$$\begin{bmatrix} Z_{11} & Z_{12} & Z_{13} \\ Z_{21} & Z_{22} & Z_{23} \\ Z_{31} & Z_{32} & Z_{33} \end{bmatrix} \begin{bmatrix} I_1 \\ I_2 \\ I_3 \end{bmatrix} = \begin{bmatrix} V_1 \\ V_2 \\ V_3 \end{bmatrix}, V_2 = -I_2 Z_{T2}, V_3 = -I_3 Z_{T3} \qquad (6)$$

By solving the equation above, the current ratios I_2/I_1 and I_3/I_1 can be calculated as (7) and (8), where I_i and Z_{Ti} are the induced current and load impedance at the reference plane of port i, respectively. The array factor of the ESPAR can be easily calculated using the results from eqn. (7) and (8) [42].

$$\frac{I_2}{I_1} = \frac{(Z_{13}*Z_{23}) - Z_{12}*(Z_{33}+Z_{T3})}{-Z_{23}^2 + Z_{22}*Z_{33} + Z_{22}*Z_{T3} + Z_{33}*Z_{T2} + Z_{T2}*Z_{T3}} \qquad (7)$$

$$\frac{I_3}{I_1} = \frac{(Z_{12}*Z_{23}) - Z_{13}*(Z_{22}+Z_{T2})}{-Z_{23}^2 + Z_{22}*Z_{33} + Z_{22}*Z_{T3} + Z_{33}*Z_{T2} + Z_{T2}*Z_{T3}} \qquad (8)$$

It is found using HFSS simulations that a wider iris width G can provide smoother variations over frequency in terms of Z_{12} and Z_{13}, which is critical to minimize beam squinting for the ESPAR. At the same time, large G values lead to the deterioration of the impedance matching. A tradeoff must be made to achieve both good impedance matching and beam squinting performance.

3.4   Simulation Results of CBS ESPAR E-plane Array

The ESPAR E-plane array in Figure 25 is simulated using ANSYS HFSS and the tuning varactors are modeled as lumped-element ports. Figure 26 demonstrates the overall beam scanning performance in the E-plane of the ESPAR array. It is observed in Figure 27 that the return loss of the array is better than 15 dB for all scanning cases at 4.08 GHz. Due to the aforementioned asymmetry in the E-plane, a beam with a maximum gain of 6.6 dBi is able to be scanned from -30 degrees to 30 degrees. The maximum scan loss is directed in the boresight direction at a level of 1.2 dBi. In Figure 28, the H-plane and E-plane radiation patterns are plotted to show that the H-plane radiation pattern is fixed at boresight while the beam is scanning in the E-plane. The stability of the H-plane radiation characteristics allows beam steering in the H-plane without interfering with the E-plane beam steering performance. Further study will be performed to investigate the H-plane beam steering capability of current design.
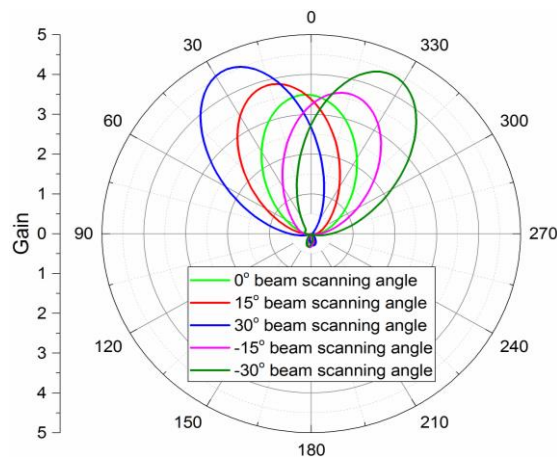
Figure 26: E-plane beam steering angles in linear scale at 4.08 GHz.

43
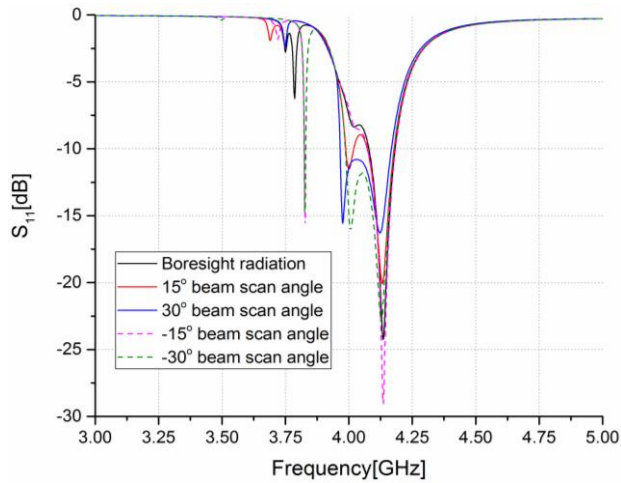
Figure 27: S_{11} for different beam scanning angles.
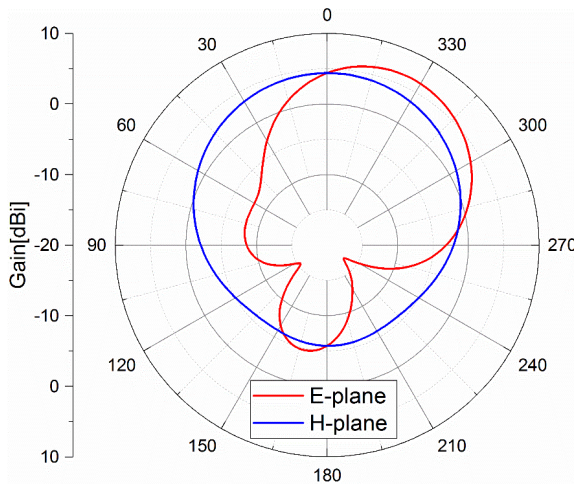
Figure 28: -30° beam steering angles in the E-plane at 4.08 GHz.

A novel cavity-backed slot ESPAR E-plane array has been demonstrated. A beam scanning range of ±30 degrees is observed in the E-plane; this breakthrough in ESPAR design introduces a new degree of freedom in spatial diversity that sets it apart from conventional ESPAR designs and significantly improves the antenna's flexibility over the current state of the art. Moreover, H-plane parasitic cavities can be easily coupled to the proposed design to form a cross array which is able to perform simultaneous E-plane and H-plane beam steering.

3.5   Introduction of the CBS ESPAR with Enhanced Bandwidth

Wireless communication systems have rapidly evolved over the past decade, which led to an explosion of mobile data traffic. More and more wireless devices and sensors need to be connected. Therefore, the transition from the current 4G/LTE mobile network to 5G is expected to happen within the next decade [7]. Though millimeter-wave (mmW) frequency spectrum can provide larger bandwidth, the sub-6 GHz spectrum is still desirable in applications when line of sight (LOS) is unavailable due to complex terrains or costly mmW beam-steerable antenna arrays are not affordable. Thus, the proposed 5G standards will contain sub-6 GHz frequency spectrum. The ESPAR can provide low-cost beam steering capability without using expensive phase shifters, which can enhance the link budget of sub-6 GHz wireless communication systems and reduce interference in a densely-populated user environment by offering spatial diversity.

Based on the radiation pattern, ESPARs can be divided into two categories: azimuthal directions using monopole antennas [34] and boresight directions with microstrip patches [42]-[46] or dielectric resonator antennas (DRAs) [57]. ESPARs using microstrip patches have a very narrow FBW of approximately 1.0% and scan in H plane only [42]-[46]. An E-plane DRA ESPAR was reported to have a 3.5% impedance matching FBW [57]. However, the beam squinting performance was not demonstrated. In the same paper [57], a DRA ESPAR with both E- and H-plane beam steering capability was presented. Nevertheless, its impedance matching FBW is only 1.0%. It is highly desirable to explore ESPARs with wider FBWs by considering both impedance matching and beam squinting. In addition, it is interesting to demonstrate E-plane beam steering capabilities. In [90], an E-plane ESPAR using cavity-backed slot antennas was shown to have 2.4%

S_{11} FBW. In [91], a five-element ESPAR using cavity-backed slot antennas exhibits 5.8% S_{11} FBW with both E- and H-plane beam steering capability. However, only simulation results were presented. In addition, the usable FBWs in [90] and [91] are reduced to 1.0% and 2.0%, respectively, by considering beam squinting.

In this section, the S_{11} and usable FBWs for the three-element E-plane ESPAR using cavity-backed slot antennas are extended to 8% and 4%, respectively, by using wider slots and custom-designed tunable loads. In the past, a continuously-impedance-tunable load for ESPARs was often realized by a varactor only. Even though the varactor can provide the necessary impedance for ESPAR matching and beam steering, it was found herein that due to the limited load impedance tuning range, severe beam squinting issues can occur. Therefore, by designing a tunable load which incorporates a fixed inductor, a varactor and a delay line, the impedance tuning range can be significantly increased. The ESPAR using this new tunable load exhibits wider FBW by considering not only S_{11} but also beam squinting performance, which has been experimentally verified. Alternatively, non-foster loads can be exploited to extend the operational FBW of ESPARs [92]. This three-element ESPAR can be readily extended to a large array, with 66% reduction in the number of phase shifters compared to a conventional phased array.
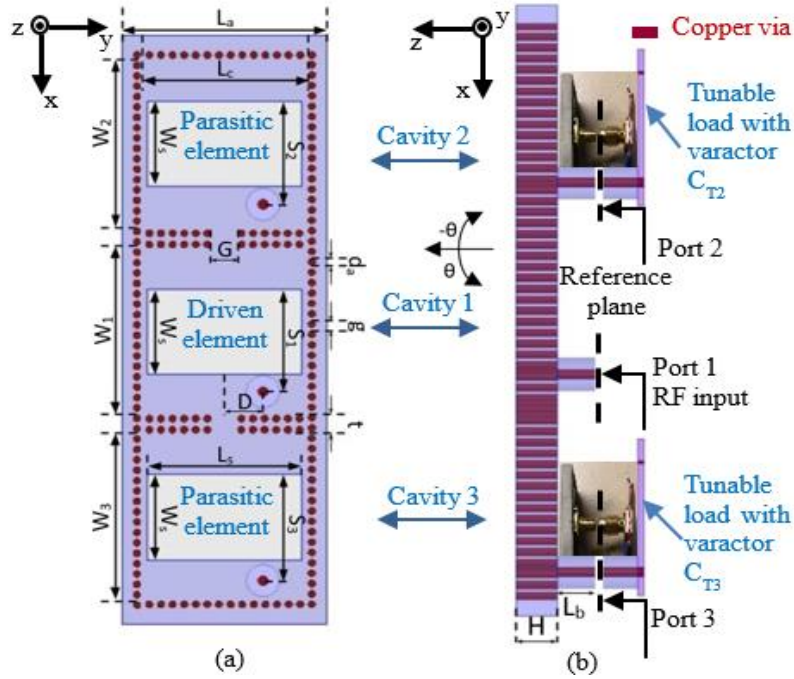
Figure 29: (a) Top and (b) side view of the three-element E-plane ESPAR using cavity-backed slot antennas. *(L_a=26.5, L_b=7.7, L_c=21.7, L_s=20.0, W_s=11.5, W_1=22.6, W_2=23.2, W_3=22.8, S_1=13.8, S_2=13.9, S_3=14.3, D=5.0, G=3.5, H=5.1, d_a=0.9, g=1.4, t=2.4. All dimensions are in mm.)*

3.6   Antenna Theory and Design

3.6.1   CBS Antenna Design

The cavity-backed slot antennas are designed on a 200-mil-thick Rogers TMM6 ($\varepsilon_r = 6$, tanδ =

0.0023) substrate as shown in Figure 29. The choice of this dielectric constant renders the spacing

between antenna elements to be 0.41 λ_0, which can avoid grating lobes in beam steering. A slot

with length L_s and width W_s is formed at the center of the cavity on the top surface. The FBW of

the cavity-backed slot antenna is enhanced by using a thicker substrate thickness H and wider slot

47

width W_s, compared with the designs in [90] and [91]. The antennas are fed by short-ended subminiature version A (SMA) connectors. The location of the inner conductor of the SMA connector is chosen to achieve critical coupling to the antenna. Two parasitic elements are coupled to the driven element through irises in the metallic walls between them. The driven element is initially designed to resonate 5% higher than 5.10 GHz. Due to the loading effects from parasitic elements, the final resonant frequency of the ESPAR will be close to the design frequency, i.e. 5.10 GHz. The iris width G and the widths of the parasitic elements, W_2 and W_3, need to be slightly adjusted in order to maximize the impedance matching bandwidth. S_2 and S_3 are also adjusted to achieve critical coupling for the parasitic elements.

3.6.2 Tunable Load Design

In addition to the iris width, the frequency-dependent load impedance is an important factor to cause beam squinting. To investigate this phenomenon, two cases regarding the tunable load are studied: Case 1) a varactor terminating a 21.5-mm-long delay line similar to Figure 30 (a); Case 2) a varactor in series with a fixed inductor terminating an 18-mm-long delay line as shown in Figure 30 (c). The delay line is introduced to rotate the impedance of 1) the varactor or 2) varactor + fixed inductor on the Smith Chart to achieve the required tuning range of Z_{Ti}.
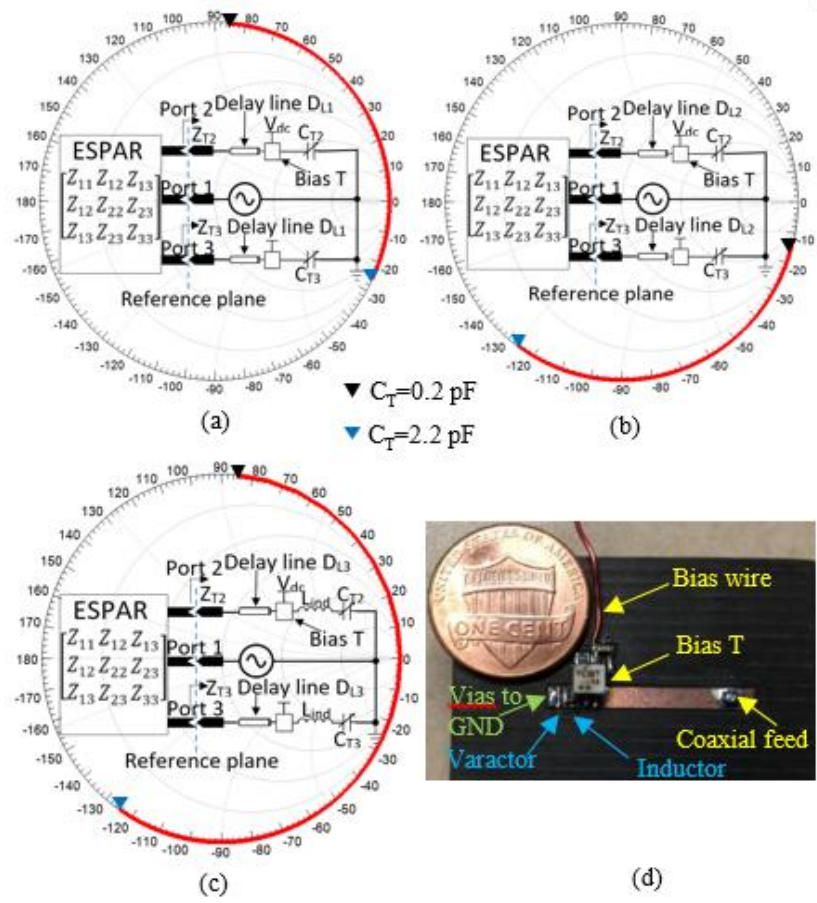
Figure 30: Tunable load with (a) varactor and D_{L1}, (b) varactor and D_{L2}, (c) varactor and D_{L3} with fixed inductor $L_{ind.}$ The simulations in (a)-(c) are performed at 5.10 GHz with varactor C_T tuning from 0.2 to 2.2 pF. d) Fabricated tunable load shown in (c). (D_{L1}=19 mm, D_{L2}=25 mm, D_{L3}=18 mm. L_{ind}=2 nH)

49
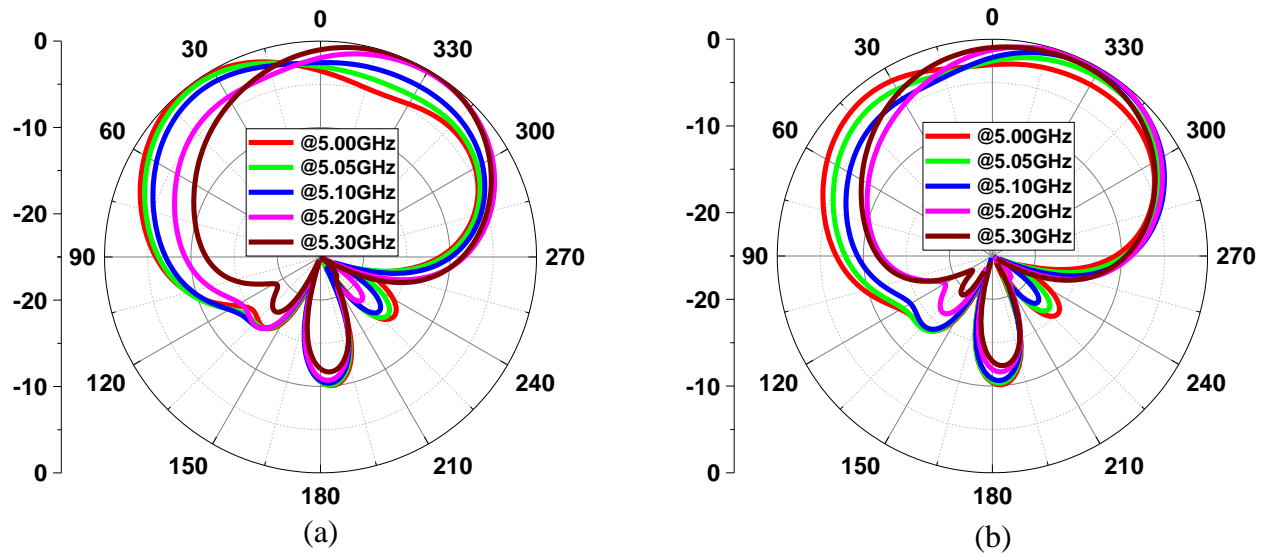
Figure 31: Simulated normalized E-plane radiation patterns at different frequencies for -26° scan angle with (a) case 1 and (b) case 2 tunable loads.
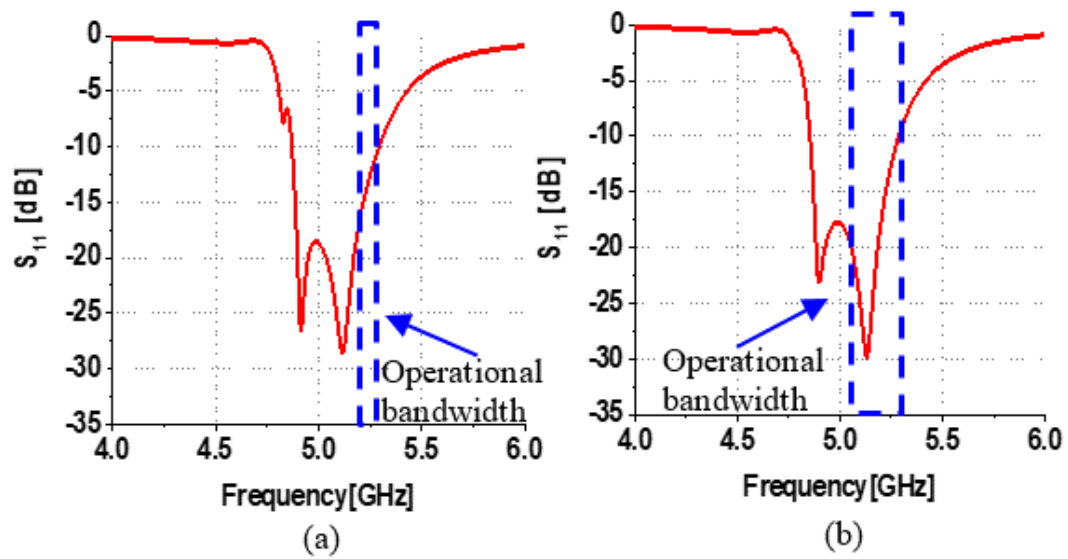
Figure 32: Simulated ESPAR S_{11} for -26° scan angle with (a) case 1 and (b) case 2 tunable loads.

To study the beam squinting performance, the ESPAR is steered to -26° in the E plane for both cases. It is observed in Figure 31 (a) that for Case 1, the ESPAR main beam is towards -26° only within 5.20-5.30 GHz, which is 25% of the S_{11} FBW as shown in Figure 32 (a). In contrast, for Case 2 as shown in Figure 31 (b), the ESPAR main beam is maintained at -26° from 5.05 to 5.30 GHz, which is 63% of the S_{11} FBW as shown in Figure 32 (b). Therefore, it is apparent that though the S_{11} FBW is similar for both cases, the usable operational bandwidth is very different by considering the beam squinting performance for this ESPAR. The beam squinting is mainly due to the induced currents on the parasitic elements. The phase difference and magnitude ratio of I_i/I_1 (i=2, 3) are plotted in Figure 33. Since Z_{23} is a very small quantity compared with other Z parameters, I_i/I_1 is approximately equal to $-Z_{1i}/(Z_{ii}+Z_{Ti})$. Im[Z_{22}] is approximate -50 Ω from HFSS simulations. Due to the limited impedance tuning range, Im[Z_{T2}] is around -150 Ω in Case 1 compared to -20 Ω in Case 2. Therefore, $|Z_{22}+ Z_{T2}|$ is much larger in Case 1, leading to a much smaller $|I_2/I_1|$ in Case 1. For Case 1, due to the small $|I_2/I_1|$ and decreased $|I_3/I_1|$ below 5.20 GHz, the beam squinting occurs below 5.20 GHz. While in Case 2, either $|I_2/I_1|$ or $|I_3/I_1|$ remains sufficiently large from 5.05 to 5.30 GHz. Therefore, the squint-free bandwidth is much wider for Case 2.
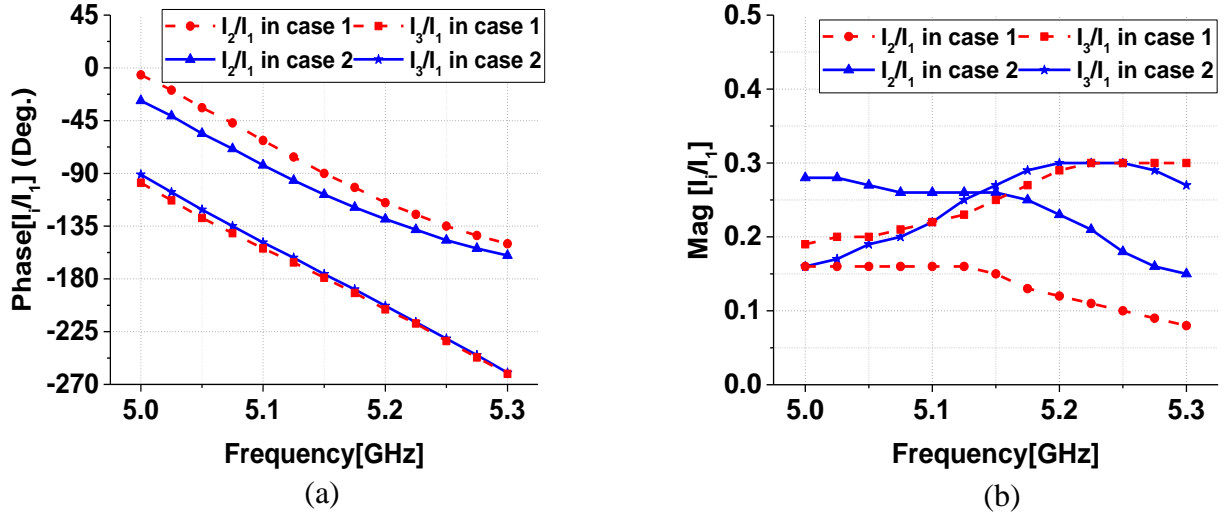
Figure 33: (a) Phase difference and (b) magnitude ratio between the induced current at port *i* and driven current at port 1 for both tunable load cases.

The impedance of the tunable load for both cases is presented in Figure 30 (a)-(c) for three different configurations. Herein the same varactor (MACOM 46580 beam lead constant gamma GaAs tuning varactor) with 0.2-2.2 pF tuning range and bias tee (TCBT-14+) are used for all three cases. For Case 2, the total effective reactance of the inductor and varactor can be calculated by (3).

$$X_{effect} = \omega L_{ind} - \frac{1}{\omega C_T} \tag{9}$$

As seen in (3), the existence of the fixed inductor can improve the reactance tuning range in the +jX_{effect} region. In Figure 30 (a) and (b), two different delay lines are studied to illustrate the impedance tuning range for Case 1. Compared with Case 2 shown in Figure 30 (c) in which L_{ind} = 2 nH, the impedance tuning range of the Case 1 tunable load is always less than Case 2. The Case 2 tunable load is fabricated using a 31-mil-thick Rogers 5880 (ε_r = 2.2,tanδ = 0.0009) substrate as shown in Figure 30 (d).
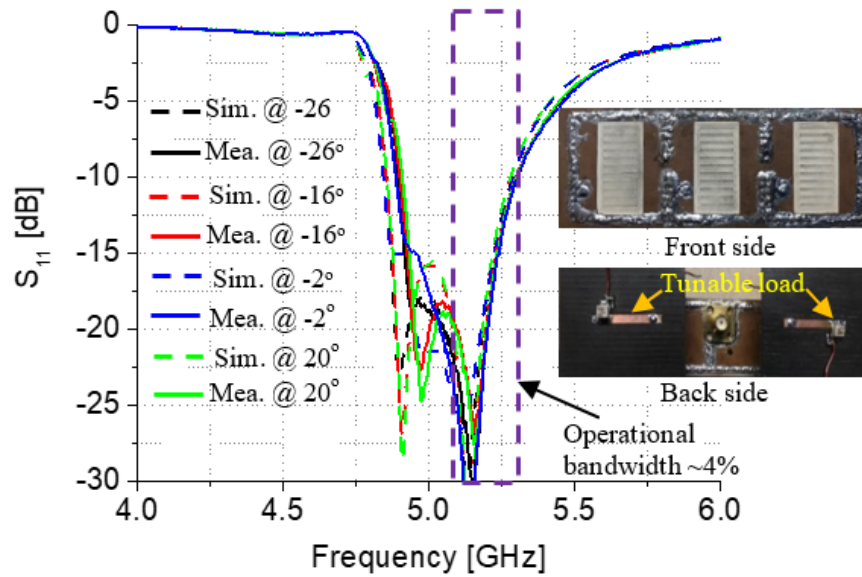
Figure 34: Simulated and measured ESPAR S_{11} for -26°, -16°, -2° and 20° scan angles. Inset: photos of the fabricated ESPAR.

3.7   Fabrication and Measurement Results

The ESPAR using the cavity-backed slot antennas is fabricated using an LPKF S100 milling machine as shown in the Figure 34. The vias are formed using 0.9-mm-diameter copper wires to realize the substrate integrated waveguide (SIW) cavity. The tunable load is connected to the ESPAR through an SMA connector at the backside of each parasitic cavity.
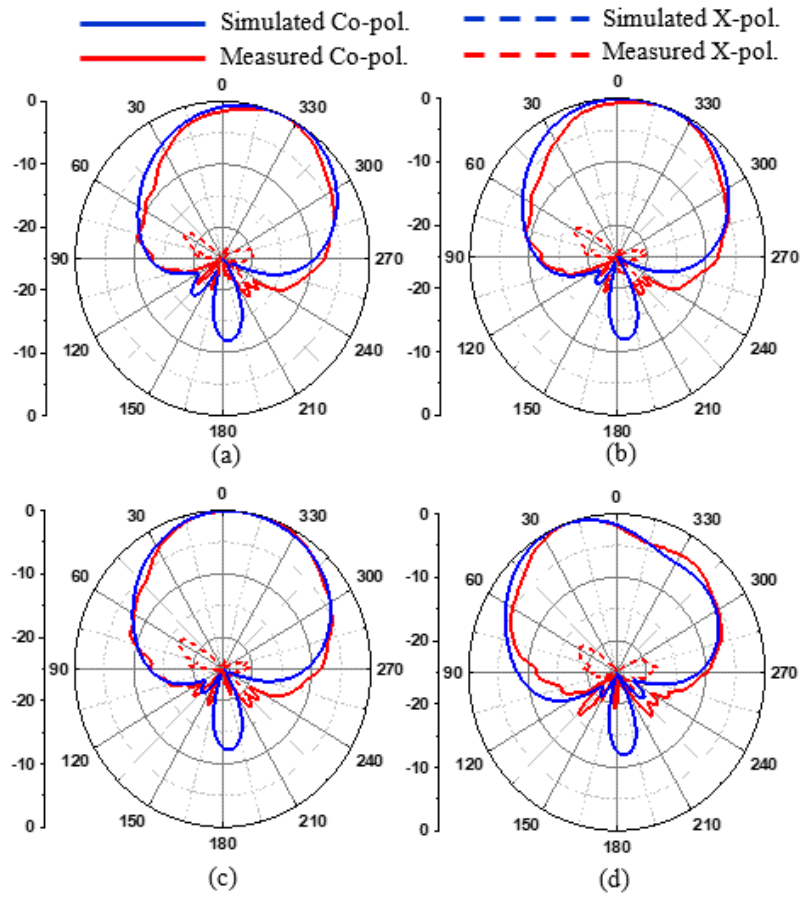
Figure 35: Simulated and measured normalized E-plane radiation patterns of the ESPAR for (a) -26º, (b) -16º, (c) -2º and (d) 20º scan angles at 5.20 GHz.
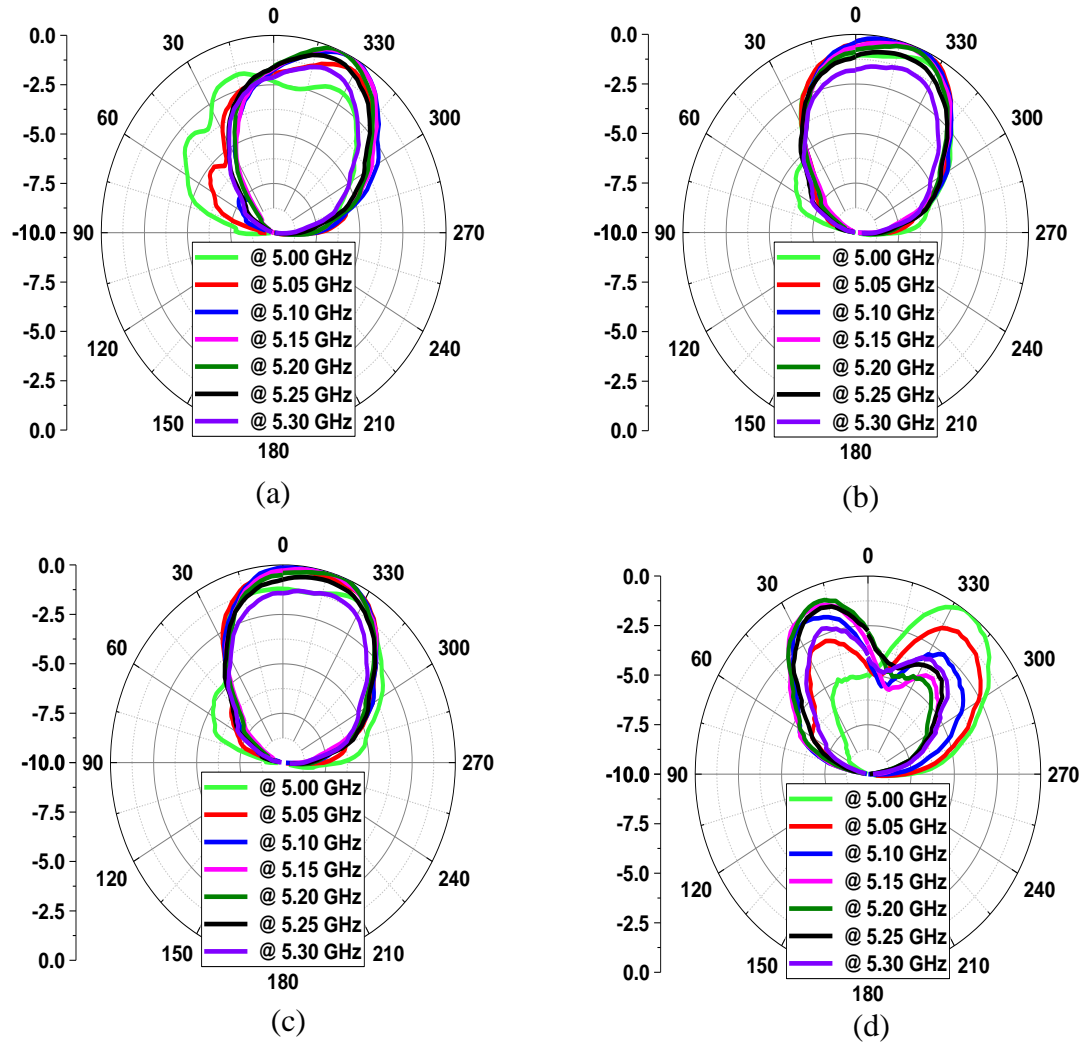
Figure 36: Measured normalized E-plane Co-pol. radiation patterns of the ESPAR for (a) -26°, (b) -16°, (c) -2°, and (d) 20° scan angles at seven different frequencies.

The measured S_{11} corresponding to -26°, -16°, -2° and 20° scan angles are compared to the simulations in Figure 34. The close agreement between the simulation and measurement results is apparent. In addition, the S_{11} is maintained below -10 dB from 4.89 to 5.30 GHz for all scan angles, which corresponds to 8% FBW.

The simulated and measured E-plane radiation patterns are compared in Figure 35 in terms of both Co-pol. and X-pol. It is observed that the measured E-plane radiation patterns match the simulation results. The measured X-pol. level is better than -17 dB in all cases. The simulated X-pol. levels are less than -25 dB so that they are not shown in the plots. When the beam scans in the E plane, the H-plane radiation patterns are fixed at the boresight. This feature provides the potential for this ESPAR to achieve independent control of E- and H-plane beam steering when two additional parasitic cavities in the H plane are added [91].
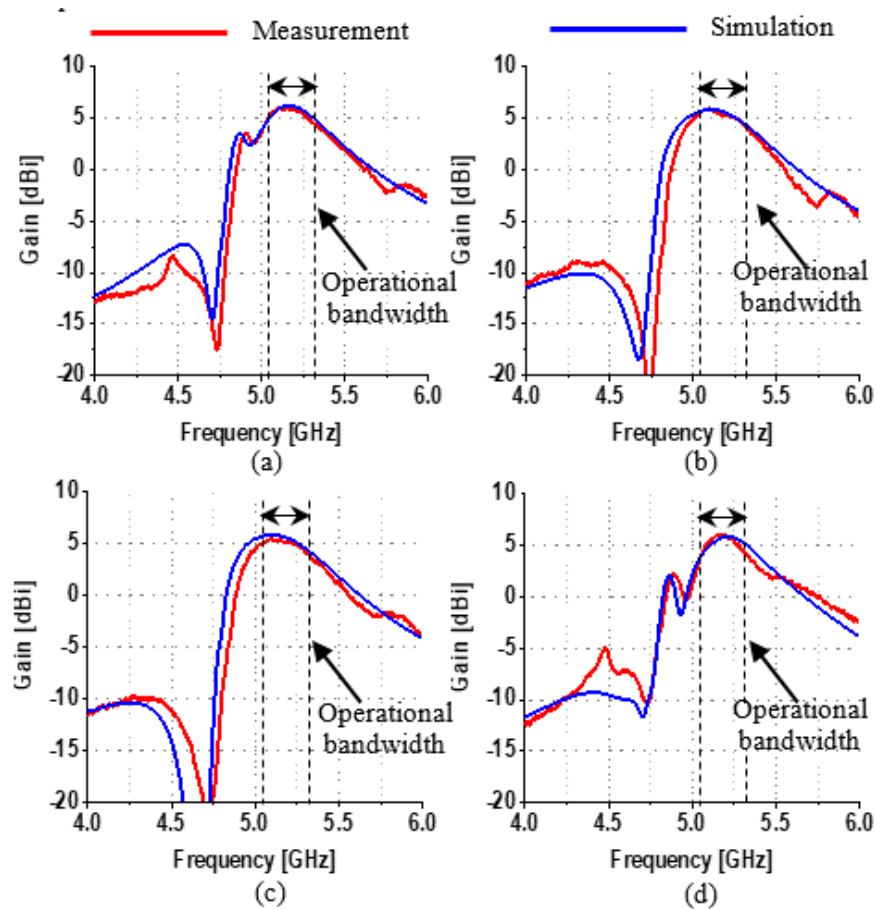
Figure 37: Simulated and measured realized gain vs. frequency of the ESPAR for (a) -26°, (b) -16°, (c) -2° and (d) 20° scan angles.

To demonstrate the beam squinting performance, the E-plane radiation patterns at seven different frequencies are plotted in Figure 36. It is noted that all the radiation patterns at different frequencies are normalized to the peak gain at each scan angle, respectively. At -16° and -2° scan angles, the beam squinting is not obvious from 5.00 to 5.30 GHz. However, at 20° scan angle, the beam squinting appears when the frequency is below 5.10 GHz. At -26° scan angle, the beam squinting shows up at frequencies below 5.05 GHz. Therefore, by taking the worst-case scenario, the usable operational bandwidth of the ESPAR is 5.10-5.30 GHz, which is approximately 4%, as shown in Figure 37.

Table 5: Summary of Load Inductance/Capacitance, Simulated and Measured Realized Gain and Efficiency η

Scan Angle [Deg.]	C_{T2} [pF]	Equ. L_2 or C_2	C_{T3} [pF]	Equ. L_3 or C_3	Sim. Gain [dBi]	Mea. Gain [dBi]	Sim.η	Meas.η
-26	2.2	1.3 pF	0.3	3.0 nH	6.16	6.05	95%	93%
-16	2.2	1.3 pF	0.8	0.5 pF	5.80	5.94	95%	98%
-2	1.5	1.0 pF	2.2	1.3 pF	5.84	5.52	95%	88%
20	0.3	3.0 nH	2.2	1.3 pF	5.82	5.93	95%	97%

The ESPAR realized gains versus frequency for the -26°, -16°, -2°, and 20° scan angles are plotted in Figure 37. The gain-bandwidth performance is consistent with the results found in Figure 36. The gain is relatively flat at -16° and -2° scan angles. While at 20° scan angle, the gain quickly reduces below 5.10 GHz, which is due to the beam squinting. The measured peak gain is found to be 6.05 dBi at -26°. Across all beam scan angles, the realized gain of the ESPAR is maintained to

be greater than 5.52 dBi. The varactor values, the equivalent inductance/capacitance of the tunable loads, the simulated and measured gains, and efficiency η, are summarized in Table 5.

3.8   Conclusion

A novel ESPAR using the cavity-backed slot antennas has been designed, fabricated and measured. This ESPAR is able to achieve 8% impedance FBW and scan from -26° to 20° in the E plane with fixed H-plane radiation pattern. The beam squinting performance is studied for this ESPAR. With a tunable load composed of a varactor and a delay line only, the operational FBW is reduced to 2%. In this paper, an improved tunable load which incorporates a fixed inductor can enhance the operational FBW to 4%. Efficiencies as high as 88% were realized in this ESPAR due to the low-loss SIW cavities. In order to realize 2-D beamsteering, a CBS ESPAR cross array is studied in next chapter. Additionally, several critical parameters are systematically studied to understand and optimize the beam squinting performance so that the useful operational FBW can match the S_{11} FBW.

CHAPTER 4   CBS ESPAR CROSS ARRAY WITH 2-D BEAMSTEERING

In previous chapters, the ESPAR is just considered specifically as individual three-element array. However, many applications require reconfigurable radiation characteristics that may not be achievable with the three-element ESPAR. In order to achieve 2-D beamsteering, a novel cavity-backed slot ESPAR cross array with plane-independent beam scanning capability is presented in this chapter. Independent E- and H-plane beam steering control is achieved by dynamically changing the load impedance of corresponding parasitic elements. It is shown that this ESPAR cross array is able to steer the beam from -24 to 24 degrees in the E-plane and -20 to 20 degrees in the H-plane; the demonstrated beam steering performance in either plane is comparable to ESPAR antennas only able to operate in a single plane.

In order to demonstrate the implantation of ESPAR to large planar array, a 20-element cavity-backed slot (CBS) antenna array is presented herein based on the five-element CBS ESPAR cross subarray. This ESPAR array is able to steer the main beam within $\pm45^\circ$ in the E plane and $\pm40^\circ$ in the H plane, respectively, without grating lobes. Inside each subarray, the beamsteering is realized by tuning the reactance of the loads on the four parasitic elements. Therefore, only four phase shifters are needed for this 20-element array to achieve 2-D beamsteering, corresponding to an 80% reduction on the number of phase shifters compared to a classic phased array. The subarray is optimized to exhibit minimum beam squint within the impedance-matching bandwidth. This 20-element ESPAR array is designed, fabricated and measured. The impedance matching is maintained below -10 dB from 6.0 to 6.4 GHz (6.4% fractional bandwidth) at all scan angles. The

radiation patterns are measured at five different scan angles in the E- and H-planes. At each scan angle, the measured radiation patterns at five frequencies across the impedance-matching bandwidth exhibit very small beam squint. The gain vs. frequency responses are measured at five different scan angles with the highest value of 14.0 dBi occurring at 6.2 GHz at the boresight direction. IIP_3 of the ESPAR cross subarray is also measured.

4.1   Introduction of the CBS ESPAR Cross Array with 2-D Beamsteering

As the development of modern wireless communication systems and sensor networks move forward, spatial diversity plays an important role in the system's efficiency. There are significant obstacles in the operational environment such as a dense frequency spectrum, line-of-sight issues, and a noisy environment; having a highly directional beam can significantly improve the SNR and communication quality. It is known that traditional phased arrays can easily achieve the desired beam scanning performance [87]-[89] however the required phase shifters and T/R modules for the phased arrays are extremely expensive, close to 50% of total phased array cost, which is a barrier for commercial applications. For these reasons, the ESPAR antenna is accepted as a practical alternative for achieving beam steering performance in phased array design. Unlike traditional phased arrays, only the center driven element is fed with RF power; all of the parasitic elements are fed by the driven element. The required phase delay for beam scanning is provided by changing the parasitic element's load impedance. By replacing the phase shifters with commercially available tunable capacitors in conventional phased arrays, the fabrication cost can be significantly reduced. Most current ESPAR designs are limited to the H-plane [42]-[46] due to the difficulty of introducing and controlling E-plane coupling in planar microstrip patch designs.

60

To address these challenges, a new coupling method is required to independently control E- and H-plane beam scanning.
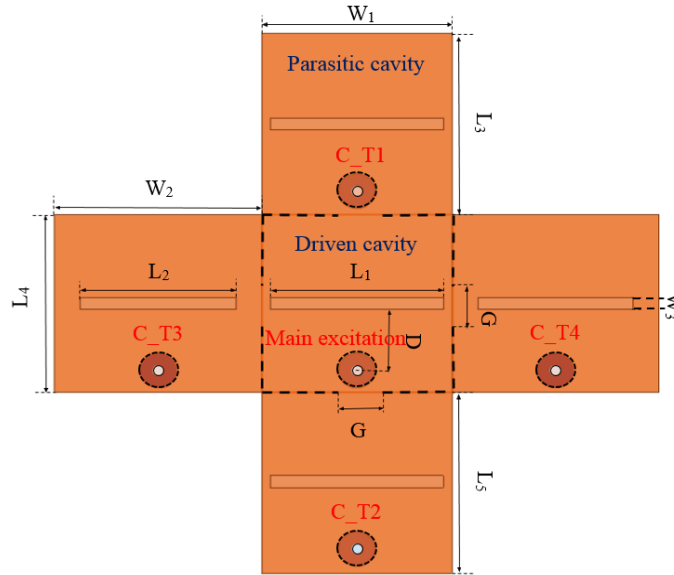
Figure 38: Schematic of the cavity-backed slot ESPAR cross array. *L_1=20, L_2=18, L_3=22.5, L_4=22.25, W_1=22, W_2=24, W_3=1.5, D=7.59, G=4. All dimensions are in mm.*

In this section, a five-element cavity-backed slot ESPAR cross array with separate E- and H-plane beam steering control is presented. The required phase shift of each parasitic element is provided by a loading tunable capacitor (varactor) as shown in Figure 38. Due to the small cross coupling between the H- and E-plane parasitic cavities, separate beam steering control in either plane is achieved. By properly designing the values of the varactors, a beam scanning range of -24 to 24 degrees is achieved in the E-plane and -20 to 20 degrees in the H-plane.

This cavity-backed ESPAR cross array introduces E-plane beam steering control without sacrificing performance in the H-plane. Such beam steering performance is comparable to another

three-dimensional design demonstrated in [57] but that work uses only capacitance to achieve all beam scanning angles. Moreover, this array can readily be extended to a full-scale array.

4.2 CBS ESPAR Cross Array Design

The five-element cavity-backed slot ESPAR cross array is designed on a 100-mil-thick Rogers RT Duroid 6006 (ε_r=6.15, tanδ=0.0019) substrate. As shown in Figure 38, the driven element is first designed to resonate at 4.1GHz; the cavity is fed by an SMA cable with the center pin touching the cavity's bottom surface. Similar parasitic cavities are placed surrounding the driven element and receive energy through coupling irises. Slots are etched at the center of the top of each cavity and a shorter slot length is used on the H-plane parasitic cavity to reduce mutual coupling with the slot on the driven cavity. The tuning varactors C_T are loaded on each parasitic cavity at the same location as on the excited cavity to achieve a maximum tuning range. By varying the capacitance C_T, the phase shift required to independently steer the beam in either the E- or H-plane is achieved.

4.3 Current Ratio between Parasitic and Driven Elements

The CBS ESPAR cross subarray is a five-port reciprocal network. The voltages and currents at the five reference planes are related by the Z matrix of this network. The current ratios I_i/I_1 can be derived from (1), where Z_{Ti} is the load reactance at the i_{th} load.

$$\begin{bmatrix} Z_{11} & Z_{12} & Z_{13} & Z_{14} & Z_{15} \\ Z_{12} & Z_{22} & Z_{23} & Z_{24} & Z_{25} \\ Z_{13} & Z_{23} & Z_{33} & Z_{34} & Z_{35} \\ Z_{14} & Z_{24} & Z_{34} & Z_{44} & Z_{45} \\ Z_{15} & Z_{25} & Z_{35} & Z_{45} & Z_{55} \end{bmatrix} \begin{bmatrix} I_1 \\ I_2 \\ I_3 \\ I_4 \\ I_5 \end{bmatrix} = \begin{bmatrix} V_1 \\ V_2 \\ V_3 \\ V_4 \\ V_5 \end{bmatrix}, V_i = -I_i Z_{Ti}(i = 2,3,4,5) \quad (\,10\,)$$

$$
\begin{bmatrix} \frac{I_2}{I_1} \\ \frac{I_3}{I_1} \\ \frac{I_4}{I_1} \\ \frac{I_5}{I_1} \end{bmatrix} = \begin{bmatrix} Z_{22} + Z_{T2} & Z_{23} & Z_{24} & Z_{25} \\ Z_{23} & Z_{33} + Z_{T3} & Z_{34} & Z_{35} \\ Z_{24} & Z_{34} & Z_{44} + Z_{T4} & Z_{45} \\ Z_{25} & Z_{35} & Z_{45} & Z_{55} + Z_{T5} \end{bmatrix}^{-1} \begin{bmatrix} -Z_{12} \\ -Z_{13} \\ -Z_{14} \\ -Z_{15} \end{bmatrix} \qquad (\,11\,)
$$

The Z matrix of the ESPAR is first extracted from ANSYS HFSS full-wave simulations. Then the radiation pattern of the subarray can be calculated by multiplying the CBS element pattern with the array factor [58]. This allows us to quickly compute the radiation pattern for different Z_{Ti} combinations and plot radiation patterns at different frequencies.

4.4   Simulation Results of the CBS ESPAR Cross Array

The ESPAR cross array in Figure 38 is simulated using ANSYS HFSS. Tuning varactors are modeled in HFSS as lumped-element ports. Figure 39 and Figure 40 illustrates the overall beam scanning performance of the ESPAR cross array. It is noted in Figure 41 that the return loss of the array is better than 10 dB for all scanning cases. The performance of the antenna in the H-plane from 0 to -20 degrees is identical to 0 to 20 degrees due to geometric symmetry. There is slight asymmetry observed in E-plane of the design which can be compensated for using asymmetric cavity dimensions. Due to the tilted radiation pattern in E-plane, the maximum gain occurs at 24 degrees and is found to be 7.31 dBi.
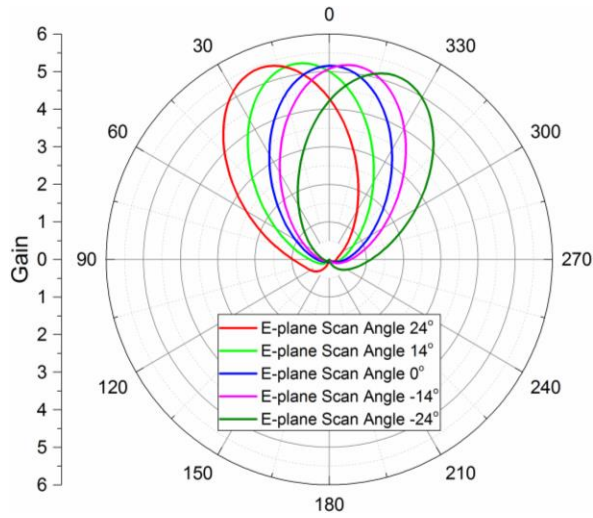
Figure 39: E-plane beam steering angles in linear scale at 4.1 GHz.
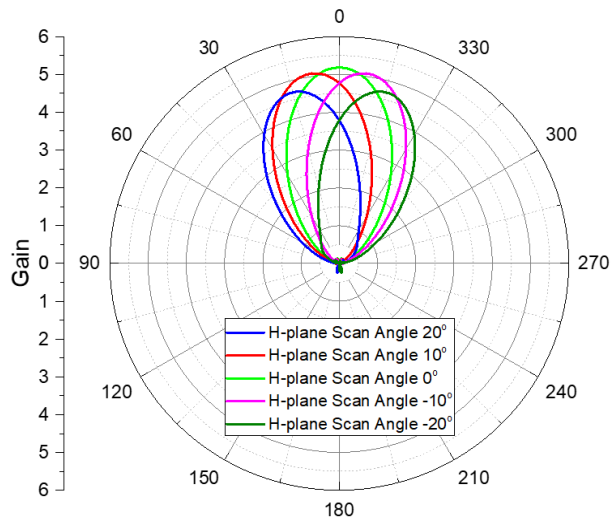
Figure 40: H-plane beam steering angles in linear scale at 4.1 GHz.
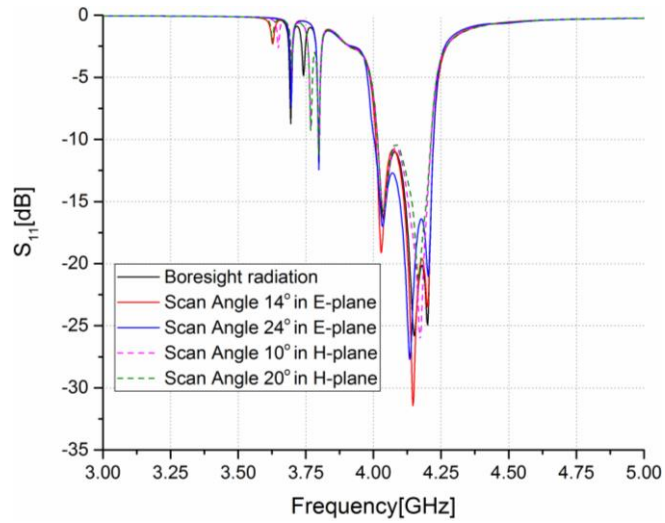
Figure 41: S_{11} for different beam scanning angles.

A novel cavity-backed slot ESPAR cross array has been demonstrated. Two-dimensional beam scanning performance is observed in E-plane and H-plane; this independent beam scanning capability significantly improves the flexibility of the current ESPAR design without compromising the maximum beam scanning range. This novel ESPAR cross array can enable more powerful wireless communication systems with its fast beamsteering capability. It should be noted that the impedance-matching FBW is only 2% for a single CBS antenna presented in this chapter. Although the impedance-matching FBW of ESPAR is much larger than a single antenna element, this increased impedance-matching bandwidth comes at the cost of poor pattern shapes and cross-polarization levels. As a result, wideband CBS antennas are studied to improve the usable FBW of the ESPAR in the next section.

4.5 Introduction of the 20-Element CBS ESPAR

Phased arrays have found their use in various applications such as radar systems [93], [94], satellite communications [1], [2], radio-frequency identification (RFID) [95], [96], and microwave imaging [11], [97]. By taking advantage of spatial selectivity and high directivity, phased arrays are able to improve signal-to-noise ratio (SNR), system capacity and link budget.

In conventional phased arrays, each antenna element requires one phase shifter or transmit/receive (T/R) module [98], [99], which are typically expensive. However, the growing demands for high data rate and large system capacity in modern communications systems such as 5G make phased arrays highly desirable. There have been research works to reduce the number of phase shifters by grouping several antenna elements into one subarray and using one phase shifter for each subarray [23]-[25]. However, this approach has a few inherent disadvantages such as many crossovers in the feeding network, limited beam scan angles, large scan losses, and narrow FBWs due to the use of long transmission lines connecting antenna elements. Akbar [26] presented a scalable phased array technique with reduced number of phase shifters. However, this approach requires the use of multiple amplifiers with limited scan angles of $\pm 18.5^{\circ}$.

Alternatively, Harrington [27] proposed to realize low-cost beamsteering by using ESPARs. The basic concept for ESPAR is to feed the parasitic antenna elements through the mutual coupling between the driven and parasitic antennas and to control the phase of the parasitic elements through tuning the reactive load on the parasitic elements. The earlier works in ESPAR focused on azimuthal beamsteering using monopoles [33]-[36]. Later, microstrip patch ESPARs were demonstrated with boresight beamsteering capability [42]-[46], however, with very limited FBW

around 1%. In addition, the beamsteering of microstrip patch ESPARs is limited to the H plane due to the difficulty of using the mutual coupling in the E plane without disturbing the radiating mode of the patch. Dielectric resonator antennas (DRAs) were shown to be able to achieve 2-D boresight beamsteering with wider impedance-matching FBW [56]-[59]. Nevertheless, the element spacing in the E plane needs to be much larger than that in the H plane in order to achieve the proper phase shift, which reduces the energy coupled to the E-plane parasitic elements and ultimately compromises the antenna gain [57]. The beam squint performance was not directly reported for DRA ESPARs. However, the 3-dB gain FBW of 5.7% for a 240-element DRA ESPAR is much narrower than its impedance-matching FBW of 13.6% [58].

Cavity-backed slot (CBS) ESPARs can achieve proper phase shifts in the E plane without the aforementioned element spacing issue [90], [100], with the benefit of high radiation efficiency using substrate integrated waveguide (SIW) technology. This concept was extended to a five-element cross array but with simulations only [91]. It should be noted that in these CBS ESPARs, the actual operational FBW is approximately half of the impedance-matching FBW due to beam squinting issues.

In this paper, several critical parameters, which affect the beam squint for a CBS ESPAR, are systematically studied. For the first time, the actual operating bandwidth for CBS ESPARs can reach the impedance-matching FBW. In addition, a 20-element CBS ESPAR using a five-element cross subarray is demonstrated herein using a triangular lattice to efficiently use the antenna aperture, as illustrated in Figure 42(a). This 20-element CBS ESPAR is able to scan ±45° and ±40° in the E- and H-plane, respectively, without grating lobes. The impedance matching is maintained

at all scan angles. The radiation patterns at each scan angle are measured at different frequencies within the operational bandwidth to ensure minimum beam squint.

4.6   CBS ESPAR Subarray Design

The five-element CBS cross subarray, as shown in Figure 42(b), is designed on a 200-mil-thick Rogers TMM6 ($\varepsilon_r = 6$, $\tan\delta = 0.0023$) substrate. First, the SIW CBS is designed to resonate at 6.2 GHz [101]. A short-ended semi-rigid coaxial cable with 0.047" outer diameter is used to feed the antenna as shown in Figure 50 (c). The maximum coupling from the coax occurs when the feeding location is very close to the SIW cavity sidewall. Critical coupling can be realized by moving the coax feed towards the center of the cavity. Four parasitic CBS antennas are coupled to the driven CBS through the irises between SIW cavities. The amount of energy coupling is determined by the width (G) and length (t) of the irises. All four parasitic cavities are terminated with a reactive load to achieve phase shifts. In the following subsections, the detailed analysis regarding the choice of critical parameters such as feeding location (S_1) and iris dimensions (t_1, G_1, t_2 and G_2) will be presented and discussed.

Compared with the subarray design in [91], the substrate is thicker and the slot is wider. Even though the S_{11} of the five-element ESPAR [91] exhibits 5.8% FBW, there are beam squinting issues within this impedance-matching FBW. It was found that the impedance-matching FBW for a single CBS antenna in [91] is actually 2%. Using the dimensions presented in this paper, the impedance-matching FBW for a single CBS is increased to 6.0%.
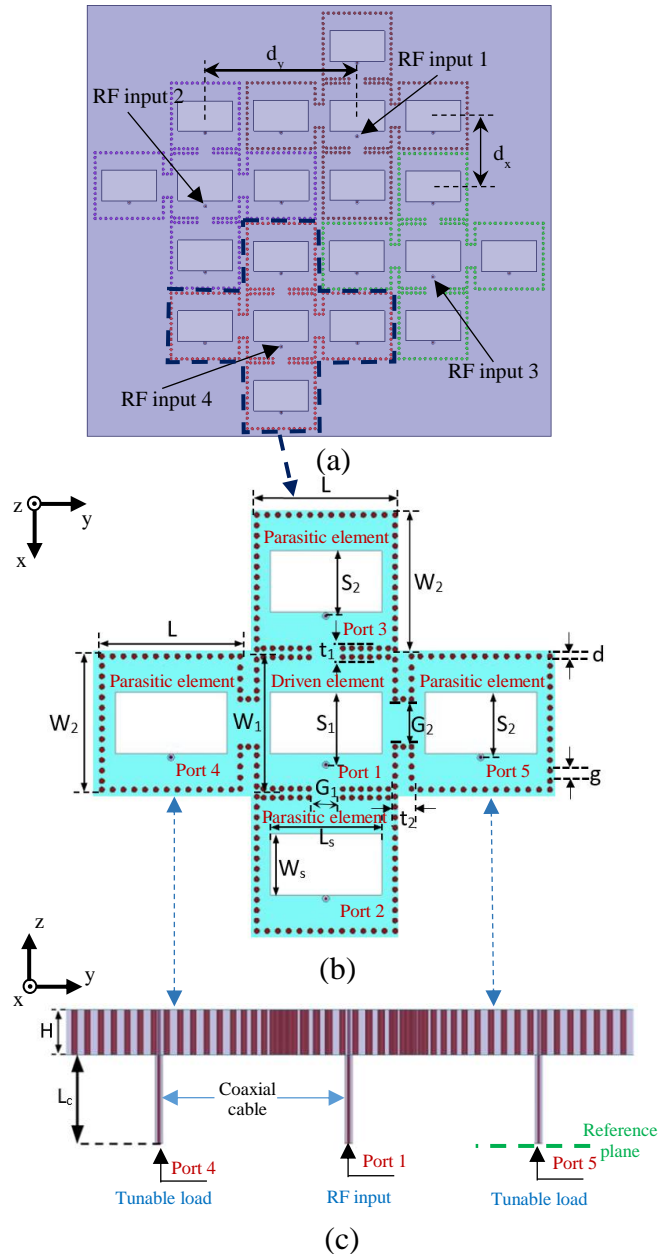
Figure 42: (a) 20-element CBS ESPAR. (b) Top and (c) side view of a cross subarray. Ports 2 and 3 are omitted in (c) since they overlap with Port 1. *L=19.5 Ls=15.5, Lc=15.8, W1=18.9, W2=19.2, Ws=8.5, S1=10.0, S2=9.0, t1=1.6, t2=3.4, G1=4.0, G2=5.5, H=5.1, d=0.7, dx=19.6, dy=42.4, g=1.3. All dimensions are in mm.*

4.6.1   Effects fom the Coax Size

When a subminiature version A (SMA) connector is used, the critical coupling is achieved when the SMA connector is placed at a location as shown in Figure 43(a). As mentioned earlier, the SMA connector needs to be moved towards the center of the cavity to achieve critical coupling. However, the wider slot prevents the SMA connector from moving further. As a result, the SMA connector is moved away from the symmetry plane of the SIW cavity, which leads to asymmetric beam scan angles in the H plane as shown in Figure 43(a). Instead, a 0.047"-diameter semi-rigid coaxial cable is used herein for the CBS ESPAR as shown in Figure 43(b). Critical coupling can still be achieved at the symmetry plane of the cavity.
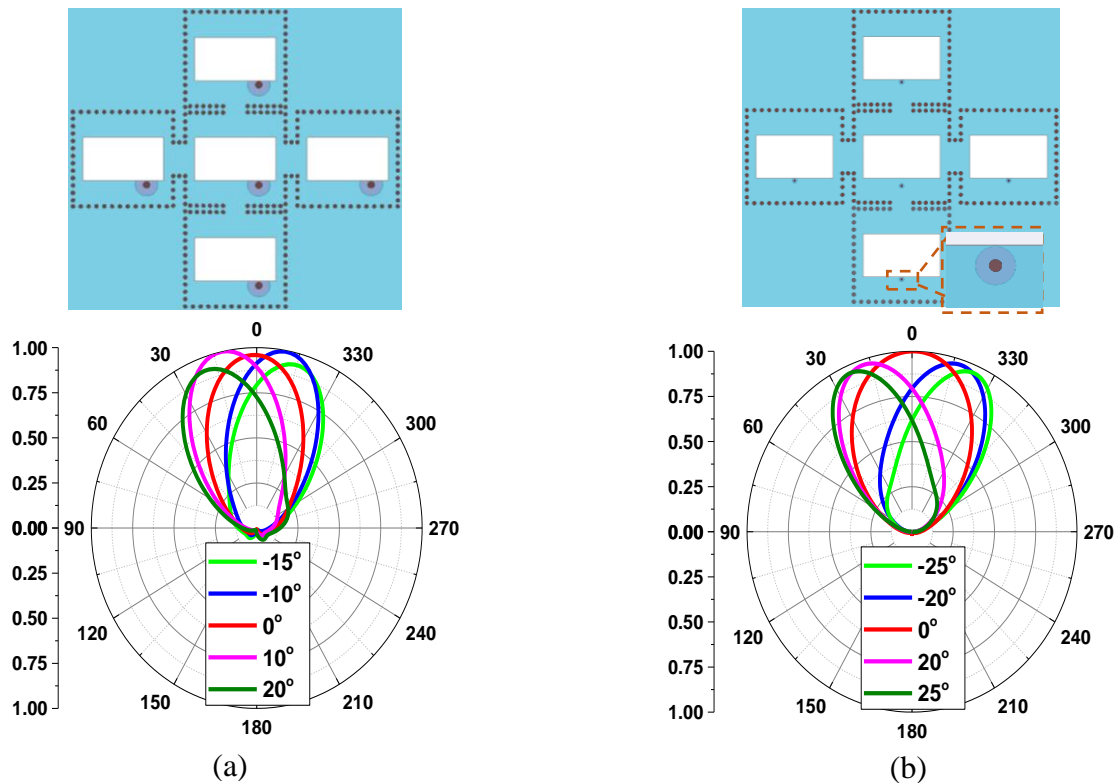
Figure 43: Simulated normalized H-plane radiation patterns of five-element CBS ESPAR cross subarray for different scan angles using (a) SMA and (b) 0.047"-diameter semi-rigid coaxial cables at 6.2 GHz in linear scale.

4.6.2 Effects from the Feeding Location

The CBS ESPAR cross subarray is a five-port reciprocal network. The voltages and currents at the five reference planes are related by the Z matrix of this network.

$$
\begin{bmatrix}
Z_{11} & Z_{12} & Z_{13} & Z_{14} & Z_{15} \\
Z_{12} & Z_{22} & Z_{23} & Z_{24} & Z_{25} \\
Z_{13} & Z_{23} & Z_{33} & Z_{34} & Z_{35} \\
Z_{14} & Z_{24} & Z_{34} & Z_{44} & Z_{45} \\
Z_{15} & Z_{25} & Z_{35} & Z_{45} & Z_{55}
\end{bmatrix}
\begin{bmatrix} I_1 \\ I_2 \\ I_3 \\ I_4 \\ I_5 \end{bmatrix}
=
\begin{bmatrix} V_1 \\ V_2 \\ V_3 \\ V_4 \\ V_5 \end{bmatrix}, V_i = -I_i Z_{Ti}(i = 2,3,4,5) \quad (\,12\,)
$$

In which Z_{Ti} is the load reactance at the i_{th} load. The current ratios I_i/I_1 can be derived from (1) and shown as follows.

$$
\begin{bmatrix}
\frac{I_2}{I_1} \\
\frac{I_3}{I_1} \\
\frac{I_4}{I_1} \\
\frac{I_5}{I_1}
\end{bmatrix}
=
\begin{bmatrix}
Z_{22} + Z_{T2} & Z_{23} & Z_{24} & Z_{25} \\
Z_{23} & Z_{33} + Z_{T3} & Z_{34} & Z_{35} \\
Z_{24} & Z_{34} & Z_{44} + Z_{T4} & Z_{45} \\
Z_{25} & Z_{35} & Z_{45} & Z_{55} + Z_{T5}
\end{bmatrix}^{-1}
\begin{bmatrix}
-Z_{12} \\
-Z_{13} \\
-Z_{14} \\
-Z_{15}
\end{bmatrix}
\quad (\,13\,)
$$

The Z matrix of the ESPAR is first extracted from ANSYS HFSS full-wave simulations. Then the radiation pattern of the subarray can be calculated by multiplying the CBS element pattern with the array factor [58]. This allows us to quickly compute the radiation pattern for different Z_{Ti} combinations and plot radiation patterns at different frequencies.

It should be noted that there are infinite number of solutions if the antenna performance is only evaluated at a single frequency. In order to minimize the beam squint, it is critical to reduce variations of the Z parameters vs. frequency. Therefore, Z_{ii} ($i=2, 3, 4, 5$) and Z_{mn} ($m=1$ or 2; $n=4$

71

or 5) are analyzed here for different feeding locations and iris dimensions since they exhibit

significantly different frequency responses.
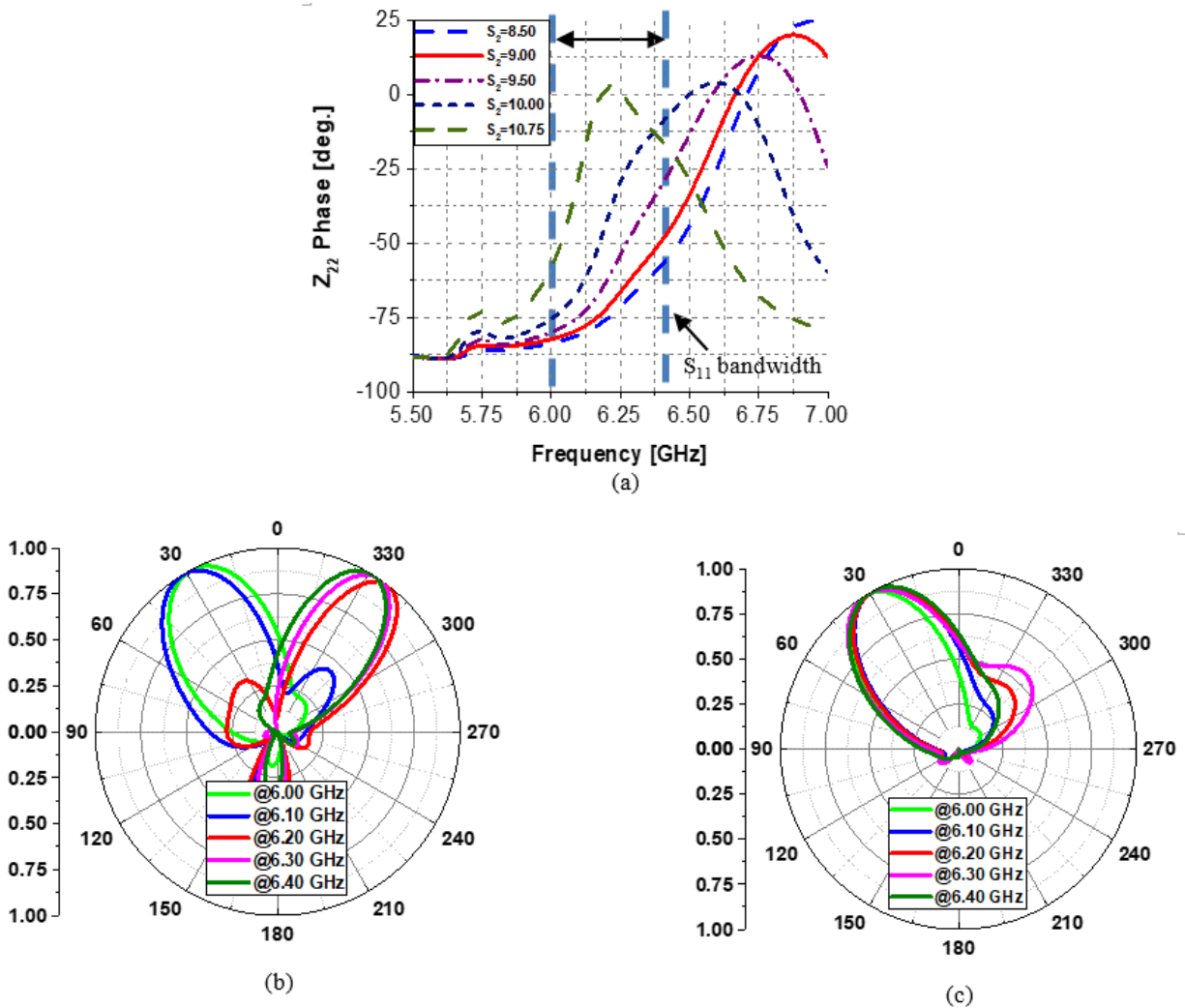
Figure 44: (a) Simulated Z_{22} phase vs. frequency for different S_2. Simulated normalized E-plane co-pol. radiation patterns for 30° scan angle with $S_2 =$ (b) 10.75 and (c) 9 at different frequencies in linear scale. *All dimensions are in mm.*

Z_{ii} (i=2, 3, 4, 5) is primarily affected by the feeding location S_2. Since all four parasitic antenna

elements are identical in size, only Z_{22} responses are presented here for brevity. In Figure 44(a),

Z_{22} phase vs. frequency is shown for several S_2 values ranging from 8.50 to 10.75 mm. Between

6.0 and 6.4 GHz, all solutions can satisfy $|S_{11}| < -10$ dB, which defines the impedance-matching FBW of the ESPAR subarray. However, the Z_{22} phase sensitivity vs. frequency is quite different for various S_2 values, ultimately affecting the I_i/I_1 response vs. frequency. The beam squinting issue for the 30° scan case in the E plane can be analyzed using (2) and the aforementioned method to calculate the radiation pattern for the subarray. When $S_2 = 10.75$ (9) mm, the I_2/I_1 phase changes by 158° (82°) within the impedance-matching FBW. The normalized radiation patterns at five discrete frequencies from 6.0 to 6.4 GHz are plotted in Figure 44(b), (c) for these two cases. It is apparent that $S_2 = 9$ mm can significantly improve beam squint performance. Though $S_2 = 8.5$ mm exhibits even better beam squint performance, the coax feeding is too close to the slot, which will create fabrication tolerance issues.

4.6.3   Effects from Iris Dimensions

Similarly, there are infinite number of combinations of t_i and G_i (i=1, 2) to provide the desirable amount of energy coupling between the driven element and parasitic elements. However, the phase response vs. frequency for Z_{mn} (m=1 or 2; n=4 or 5) is quite different. In this study, the magnitude and phase responses vs. frequency for both Z_{12} and Z_{13} ($Z_{12} \approx Z_{13}$) are found to be very similar for different G_1 and t_1 values, therefore they are not shown here.

The mutual coupling between the driven and parasitic elements in the H plane is represented by Z_{14} and Z_{15}. Owing to the geometry symmetry, $Z_{14} = Z_{15}$. The Z_{14} magnitude response vs. frequency is illustrated in Figure 45(a). It is noted that (1) all the t_2 and G_2 values must ensure $|S_{11}| < -10$ dB from 6.0 to 6.4 GHz, and (2) the Z_{14} phase response vs. frequency is very similar for different cases therefore it is not shown here. The radiation patterns at five different frequencies from 6.0 to 6.4

GHz for the 25° scan angle in the H plane are compared in Figure 45(b) and 4(c) for (1) t_2=1.4 mm, G_2=4.5 mm and (2) t_2=3.4 mm, G_2=5.5 mm, respectively. In Figure 45(a), it is observed that the Z_{14} magnitude variation vs. frequency is less for Case 2, which leads to better beam squint. There are two other cases, which also exhibit relatively smooth variations versus frequency below the trace for Case 2 in Figure 45(a). However, the beam scan range is limited, therefore they are not chosen for this design.

(a)

(b)

(c)
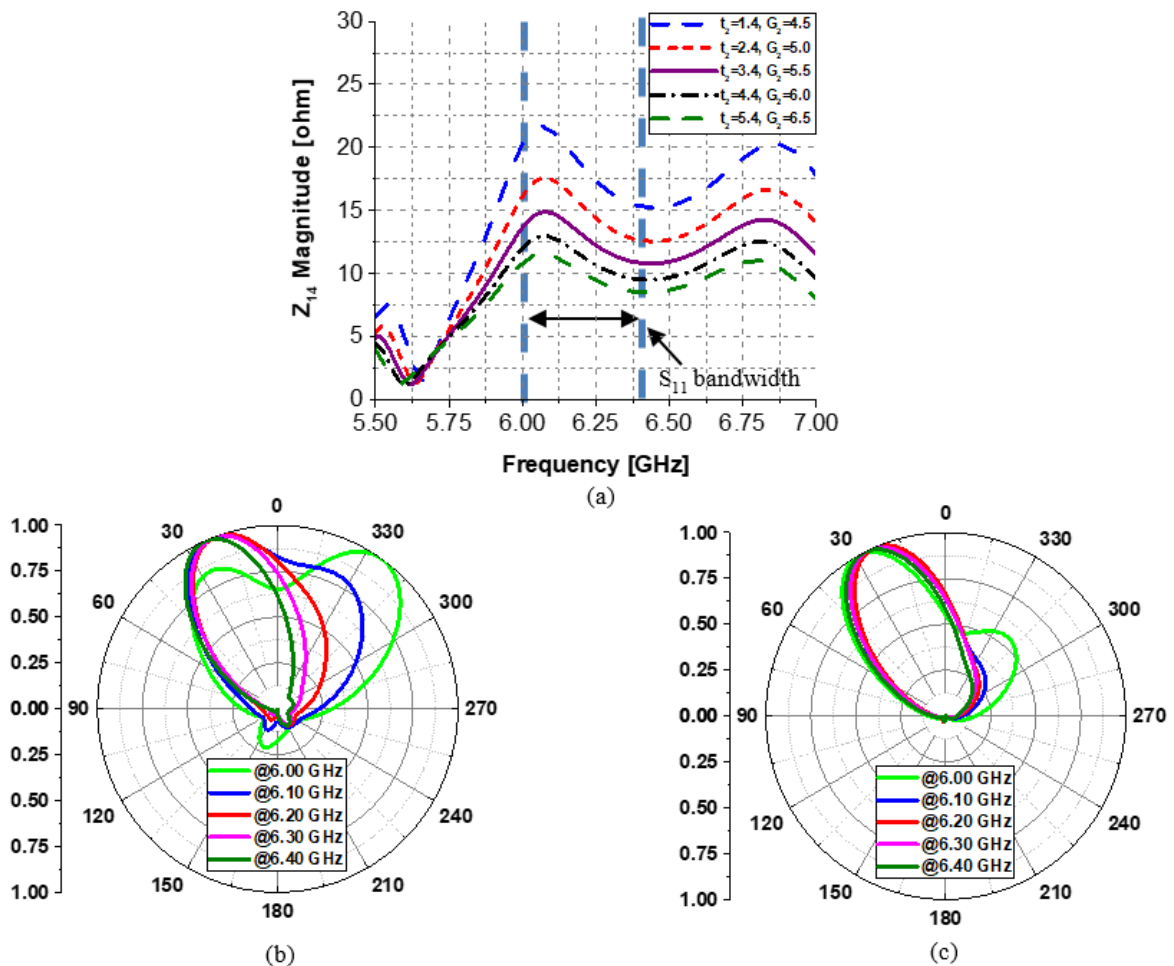
Figure 45: Simulated Z_{14} magnitude vs. frequency for different iris dimensions t_2 and G_2. Simulated normalized H-plane co-pol. radiation patterns for 25° scan angle with (b) t_2=1.4, G_2=4.5, and (c) t_2=3.4, G_2=5.5 at different frequencies in linear scale. *All dimensions are in mm.*
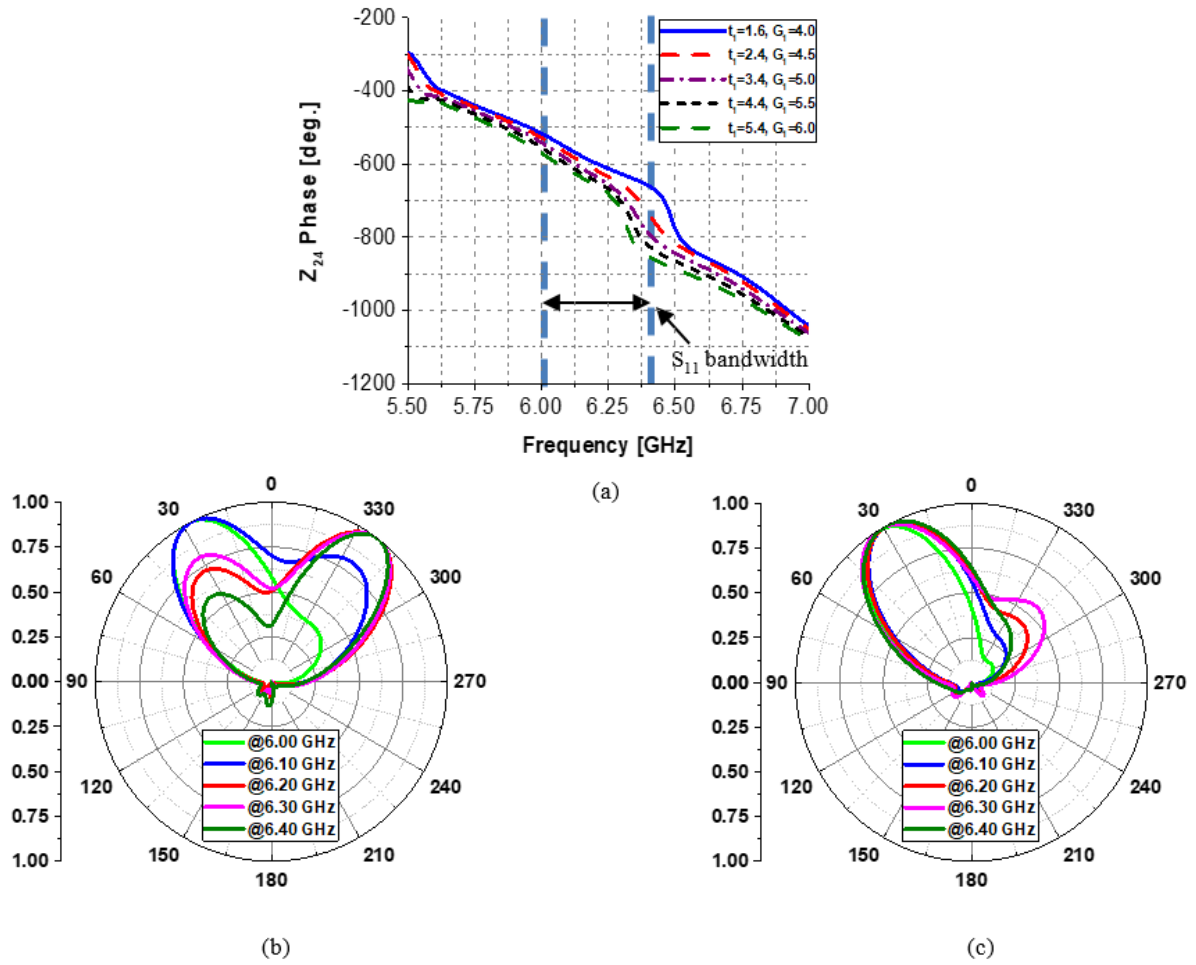
Figure 46: (a) Simulated Z_{24} phase vs. frequency for different iris dimensions of t_1 and G_1. Simulated normalized E-plane co-pol. radiation patterns for 30° scan angle with (b) t_1=5.4, G_1=6.0, and (c) t_1=1.6, G_1=4.0 at different frequencies in linear scale. *All dimensions are in mm.*
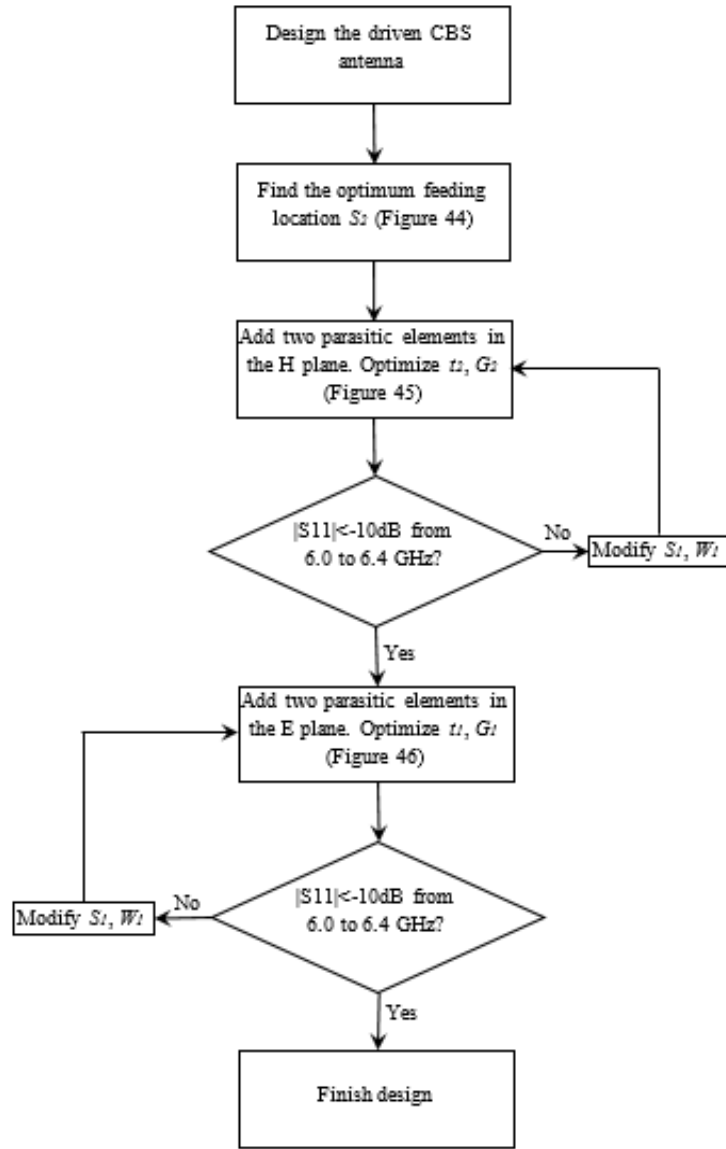
Figure 47: Design flowchart for the five-element CBS ESPAR subarray.

As mentioned earlier, Z_{12} and Z_{13} magnitude and phase responses vs. frequency are similar for different combinations of t_1 and G_1. However, it is desirable to design $|Z_{12}| \approx |Z_{14}|$ in order to evenly distribute the power from the driven element to every parasitic element. It is observed in this study that the different t_1 and G_1 values affect the $Z_{24} (= Z_{25})$ phase response vs. frequency, consequently

leading to different beam squinting performance. As a result, the parametric study on Z_{24} phase vs. frequency for different t_1 and G_1 combinations is presented in Figure 46(a). It is noted that for all cases in Figure 46(a): (1) $|S_{11}| < -10$ dB from 6.0 to 6.4 GHz, (2) $|Z_{12}| \approx |Z_{14}|$, and (3) $|Z_{24}|$ magnitude vs. frequency is similar. It is observed in Figure 46(a) that $t_1=1.6$ mm and $G_1=4.0$ mm provide the smoothest variation over the frequency range, which gives rise to the best beam squinting performance at 30° scan angle in the E plane. The I_2/I_1 phase changes by 291° and 82° from 6.0 to 6.4 GHz for the cases in Figure 46(b) and (c), respectively.

Overall, the iris thickness in the H plane, t_2, needs to be larger for smaller $|Z_{14}|$ variations. However, further increasing t_2 will limit the scan angle since the amount of energy coupled to the parasitic elements in the H plane is too small. The iris thickness in the E plane, t_1, should be as small as possible. In this design, t_1 is the smallest dimension for two rows of vias.

The design flow of the five-element CBS ESPAR subarray is illustrated in Figure 47. The feeding location S_1 and cavity width W_1 for the driven element need to be slightly adjusted during the design process in order to ensure good impedance matching from 6.0 to 6.4 GHz. The final dimensions for the subarray are listed in Figure 42.

4.7   CBS ESPAR Subarray Simulation Results

To simulate the CBS ESPAR cross subarray designed in Section II, each parasitic element is terminated with a tunable reactive load at the reference plane illustrated in Figure 42(c). This tunable reactive load incorporates a varactor (0.2-2.2 pF), an inductor (2 nH), a bias tee and a microstrip delay line with a length of 8.3 (7.3) mm for the parasitic elements in the H (E) plane.

77

This tunable reactive load can provide either an equivalent inductance or capacitance by varying the bias voltage on the varactor. Compared with a varactor-only load, it can reduce the amount of beam squint. The details on how to design such tunable reactive loads are in [27].
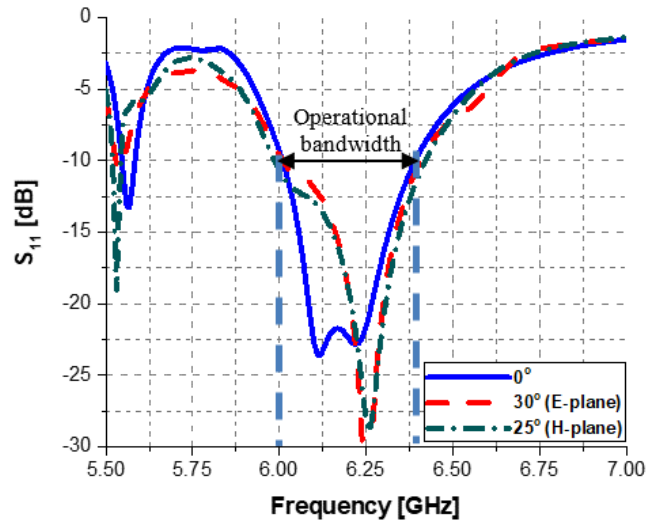
Figure 48: Simulated S_{11} of the ESPAR cross subarray for different scan angles.

The reflection coefficients at Port 1 for the boresight, the maximum scan angle in the E plane of 30 degree, and the maximum scan angle in the H plane of 25 degree are plotted using HFSS, demonstrating $|S_{11}|<-10$ dB for all scan angles from 6.0 to 6.4 GHz, corresponding to a 6.4% FBW. The radiation patterns for the boresight and extreme scan angles in both E and H planes are shown in Fig 8, for five discrete frequencies across the entire operational bandwidth. Very minor beam squint is observed for all scan angles. The maximum realized gain for the subarray is found to be 7.6 dBi at the boresight. The maximum scan losses are 0.4 and 0.3 dB in the E and H plane, respectively.
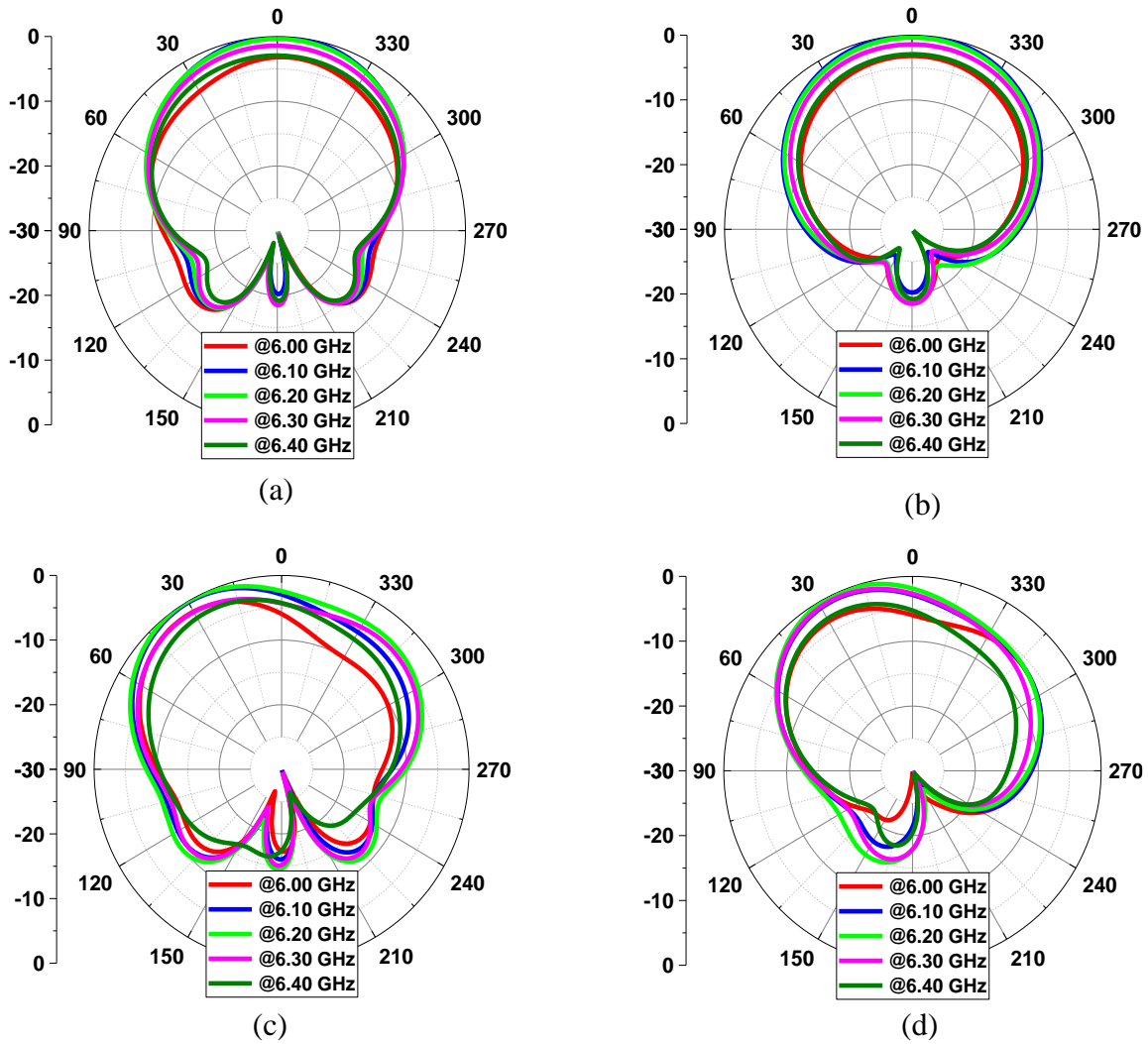
Figure 49: Simulated normalized subarray radiation patterns for 0° scan angle in the (a) E and (b) H plane, (c) 30° scan angle in the E plane, and (d) 25° scan angle in the H plane at five discrete frequencies.

4.8   Array Formation

In order to reduce grating lobes at large scan angles, the subarrays are arranged to form a triangular lattice as shown in Figure 42(a). The radiation pattern of the entire 20-element ESAPR is equal to the product of the radiation pattern of the subarray and the array factor for the four driven elements.

This array formation is similar to the DRA ESPAR array in [24] since both ESPAR subarrays use a five-element cross shape. As discussed in [23], if a classic rectangular lattice is adopted for this cross subarray, grating lobes appear when the beam is scanned.

(a)

(b)

(c)
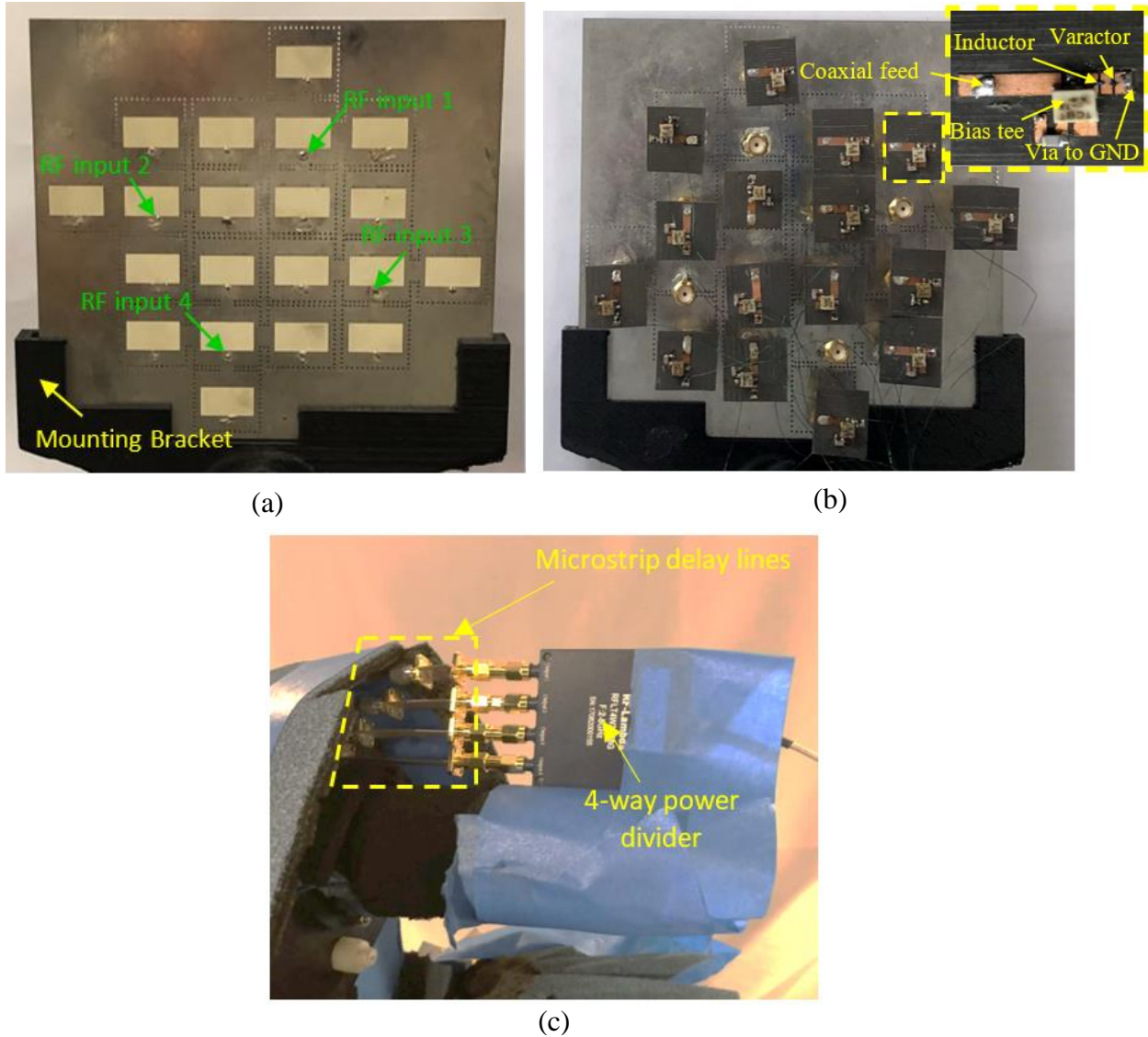
Figure 50: (a) Front and (b) back side of the 20-element ESPAR array. (c) Four-way power divider and microstrip delay lines for the driven elements. MACOM 46580 beam lead constant gamma GaAs tuning varactor, Murata LQP03TN chip inductor, Mini-Circuits surface mount bias tee (TCBT-14+) are used here.

4.9 Fabrication and Measurement

4.9.1 Antenna Fabrication and Measurement Setup

The CBS ESPAR array is fabricated using standard PCB fabrication process by Hughes Circuits Inc. as shown in Figure 50. The 0.7-mm-diameter vias are drilled and then copper electroplated to form the SIW cavities. The inner conductors of the 0.047"-diameter coax lines, which are made by Taoglas Ltd., are placed inside the non-plated 0.4-mm-diameter feed vias and soldered to the top surface of the antenna. The tunable loads are connected to the parasitic elements at the backside using SMA connectors as shown in Figure 50(b). For the boresight radiation measurement, the four driven elements are combined together using a four-way power divider (RF-Lambda RFLT4W2G08G). In order to measure the radiation patterns scanned in either E or H plane, four microstrip delay lines are inserted in the power-combining network to provide the required phase shifts for the driven elements, as illustrated in Figure 50(c).

4.9.2 Measurement Results

The S_{11} of each subarray is measured using an Agilent N5230A PNA-L. To verify the maintained impedance matching at different scan angles, the simulated and measured S_{11} corresponding to boresight radiation, 20°, 45° scan angles in the E plane, and 20°, 40° scan angles in the H plane are compared in Figure 51. The close agreement between the simulation and measurement, as well as stable impedance matching within the entire scan range is apparent. The operational bandwidth of this ESPAR subarray is from 6.0 to 6.4 GHz, which corresponds to a 6.4% FBW.
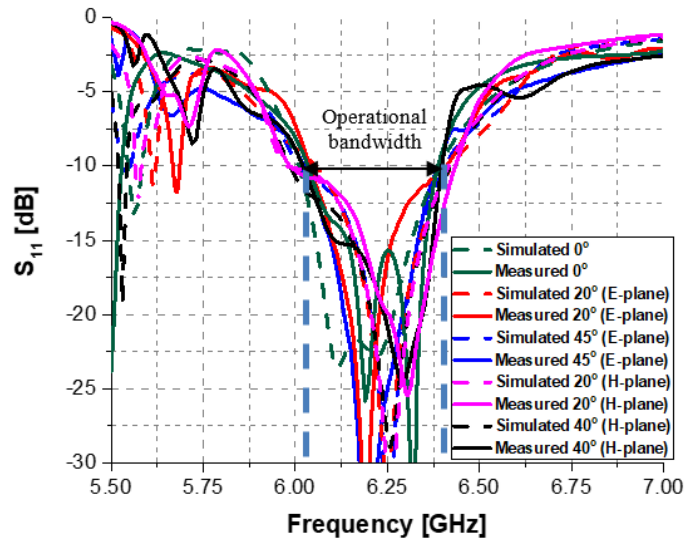
Figure 51: Simulated and measured S_{11} of the subarray for different scan angles.

To facilitate the radiation pattern and gain measurement, a mounting bracket is fabricated by a 3-D printer to hold the antenna aperture as shown in Figure 50(a). The far field measurement is performed in an anechoic chamber in the ARMI laboratory at the University of Central Florida. The simulated and measured E-plane radiation patterns for 0°, 20°, and 45° scan angles in the E plane are plotted in Figure 52(a)-(c). It is observed that the measured E-plane radiation patterns agree with the simulation results. The X-pol. levels are less than -25 dB for all scan cases. The simulated and measured H-plane radiation patterns for 0°, 20° and 40° scan angles in the H plane are displayed in Figure 52(d)-(f). The X-pol. levels are 20 dB below the Co-pol. for all scanning cases, with the highest X-pol. level at 40° scan angle. Overall, the agreement between the simulation and measurement is very good. The measured sidelobe levels (SLLs) at the boresight are slightly, i.e. 5 dB, higher than the simulation. However, the measured SLLs are below -12.5 dB in all cases shown Figure 52.
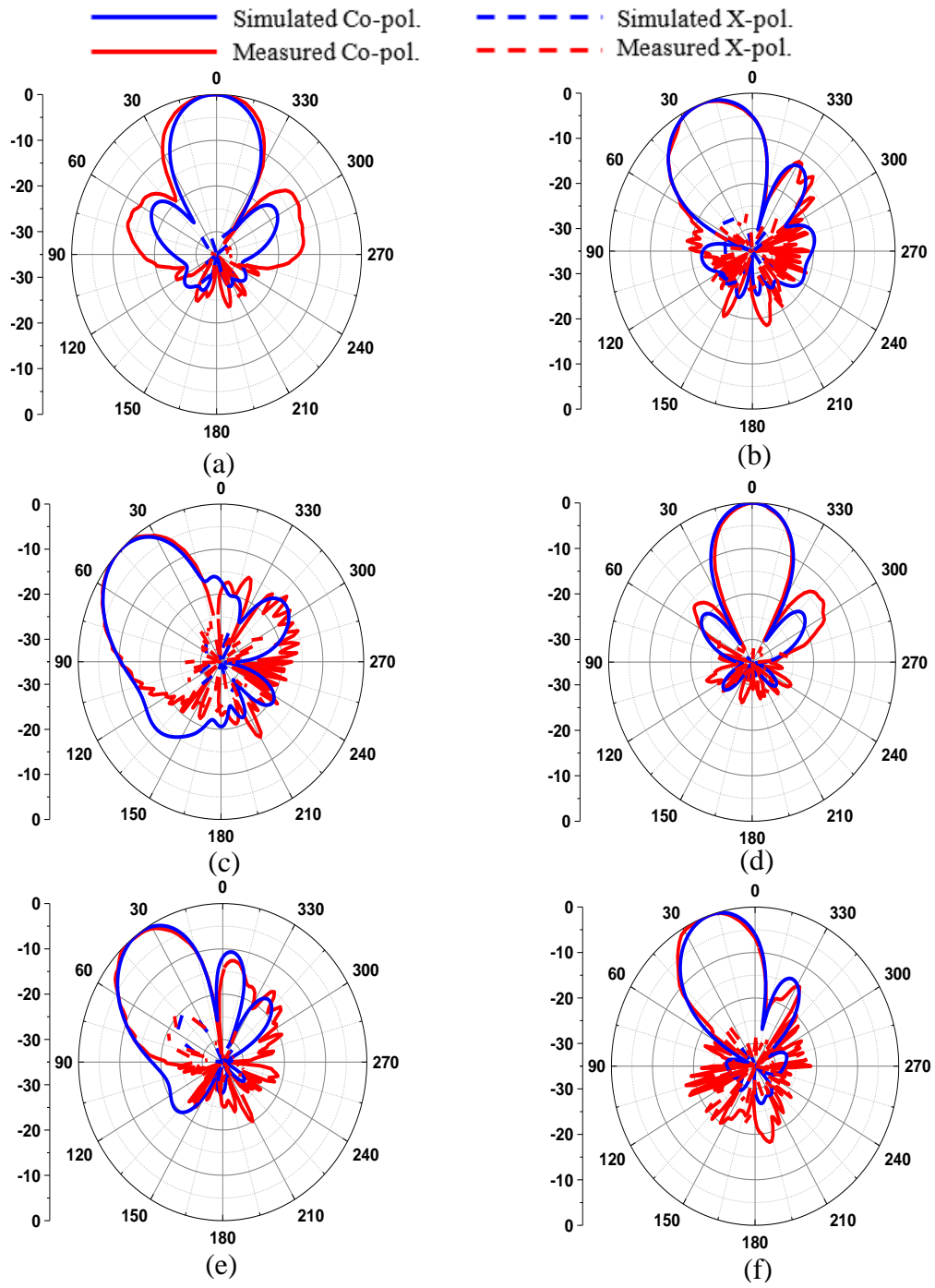
Figure 52: Simulated and measured normalized E-plane radiation patterns of the ESPAR for (a) 0º, (b) 20º, (c) 45º scan angles for E-plane scanning, and H-plane radiation patterns of the ESPAR for (d) 0º, (e) 20º, and (f) 40º scan angles for H-plane scanning at 6.2 GHz.
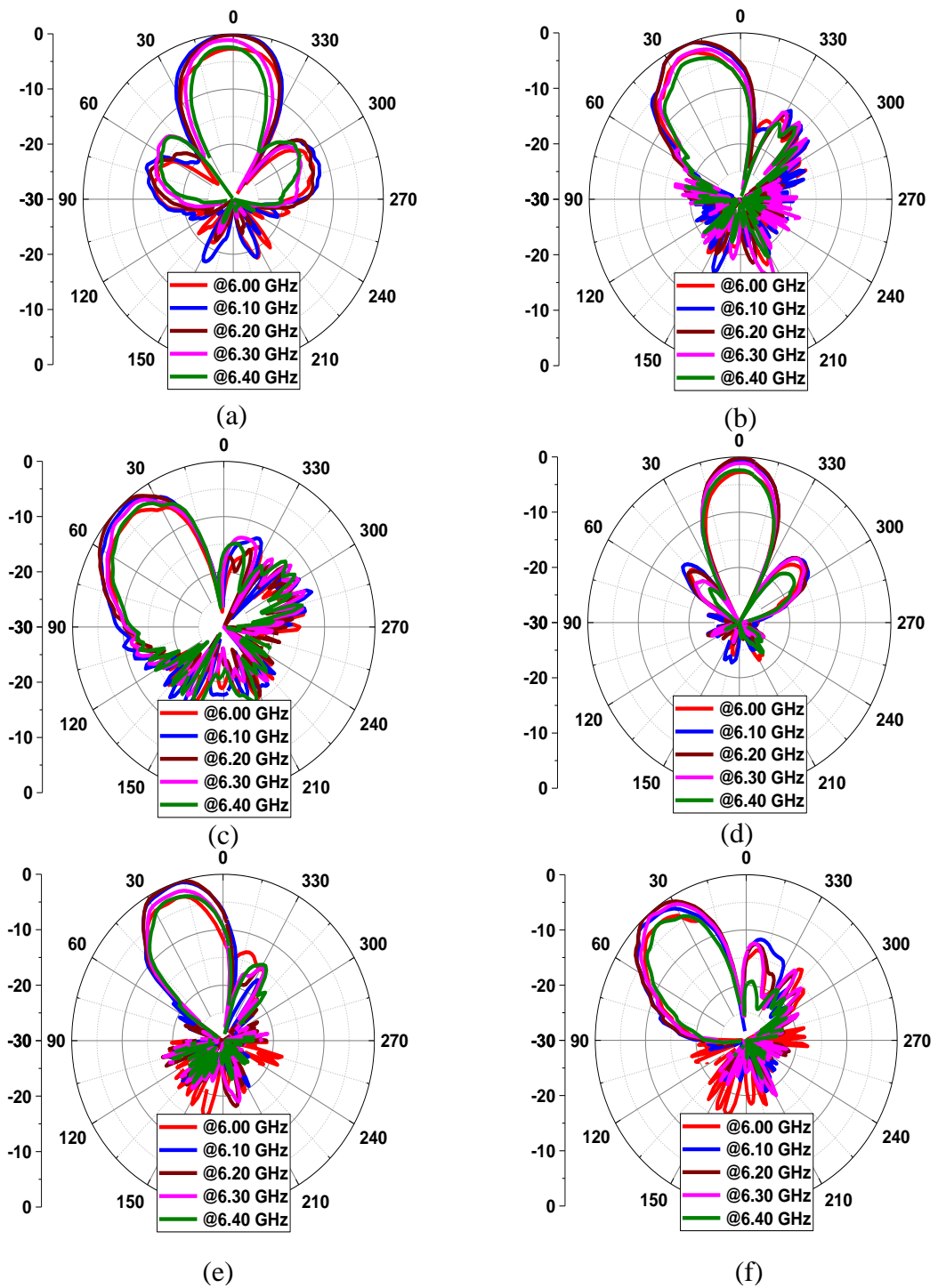
Figure 53: Measured normalized E-plane radiation patterns for (a) 0º, (b) 20º, (c) 45º scan angles and H-plane radiation patterns for (d) 0º, (e) 20º, and (f) 40º scan angles of the ESPAR at five discrete frequencies.

The E- and H-plane Co-pol. radiation patterns are also plotted at five discrete frequencies from 6.0 to 6.4 GHz for the aforementioned scan angles in Figure 53. It is observed that the maximum radiation directions are maintained for all scan angles within the operational bandwidth. The variations of the realized gain are less than 3 dB across the antenna bandwidth.

The realized gains of the ESPAR versus frequency for five different scan angles are plotted in Figure 54. The measured peak gain is found to be 14.0 dBi at 0°. The scan loss is 1.51 and 1.53 dB for the E and H plane, respectively. The equivalent inductance or capacitance of the tunable loads at the reference planes and the simulated and measured gains are summarized in Table 6.

Table 6: Summary of Equivalent Load Inductance/Capacitance, Simulated and Measured Realized Gain

Scan Angle (ϕ, θ) [deg.]	Eq. L_2 or C_2	Eq. L_3 or C_3	Eq. L_4 or C_4	Eq. L_5 or C_5	Sim. Gain [dBi]	Meas. Gain [dBi]
(0, 0)	1.0 nH	1.0 nH	0.2 pF	0.2 pF	14.1	14.0
(0, 20)	0.1 pF	2.0 nH	0.2 pF	0.2 pF	13.6	13.4
(0, 45)	0.3 pF	0.5 nH	0.2 pF	0.2 pF	12.5	12.5
(90, 20)	1.0 nH	1.0 nH	3.0 nH	0.4 pF	13.3	13.2
(90, 40)	1.0 nH	1.0 nH	1.0 nH	0.5 pF	12.5	12.5

The input third-order intercept point (IIP_3) of the CBS ESPAR subarray is characterized using the measurement setup as shown in Figure 55(a). Two isolators (ISOs) (RF-Lambda RFLI-402-4) and one two-way power divider (RF-Lambda RFLT2W2G08G) are used to combine two main tones with 100 kHz frequency separation at a center frequency f_0 of 6.2 GHz and feed the CBS ESPAR subarray. As shown in Figure 55(b) and (c), the measured IIP_3 is 44.3 (46.2) dBm for 0° (30°) scan angle in the E plane. The tunable slot-ring antenna presented in [47] exhibits IIP_3 values ranging from -5 to 30 dBm depending on the bias voltage. It should be noted that the antenna in [47] uses a different varactor (M/A-Com MA46H071-1056, 2.5-0.45 pF from 0-20V) and operates from 0.95 to 1.8 GHz. The high IIP_3 for the CBS ESPAR is due to the fact that (1) a significant portion of energy incident into the driven element is coupled to the four parasitic elements, and (2) not all the energy coupled to the parasitic elements enters the reactive loads. In HFSS simulations, it is found the $S_{i,1}$ (i=2, 3, 4, 5) is between -15 and -12.5 dB, which represents the percentage of the incident power that is coupled to the ports on the parasitic elements.
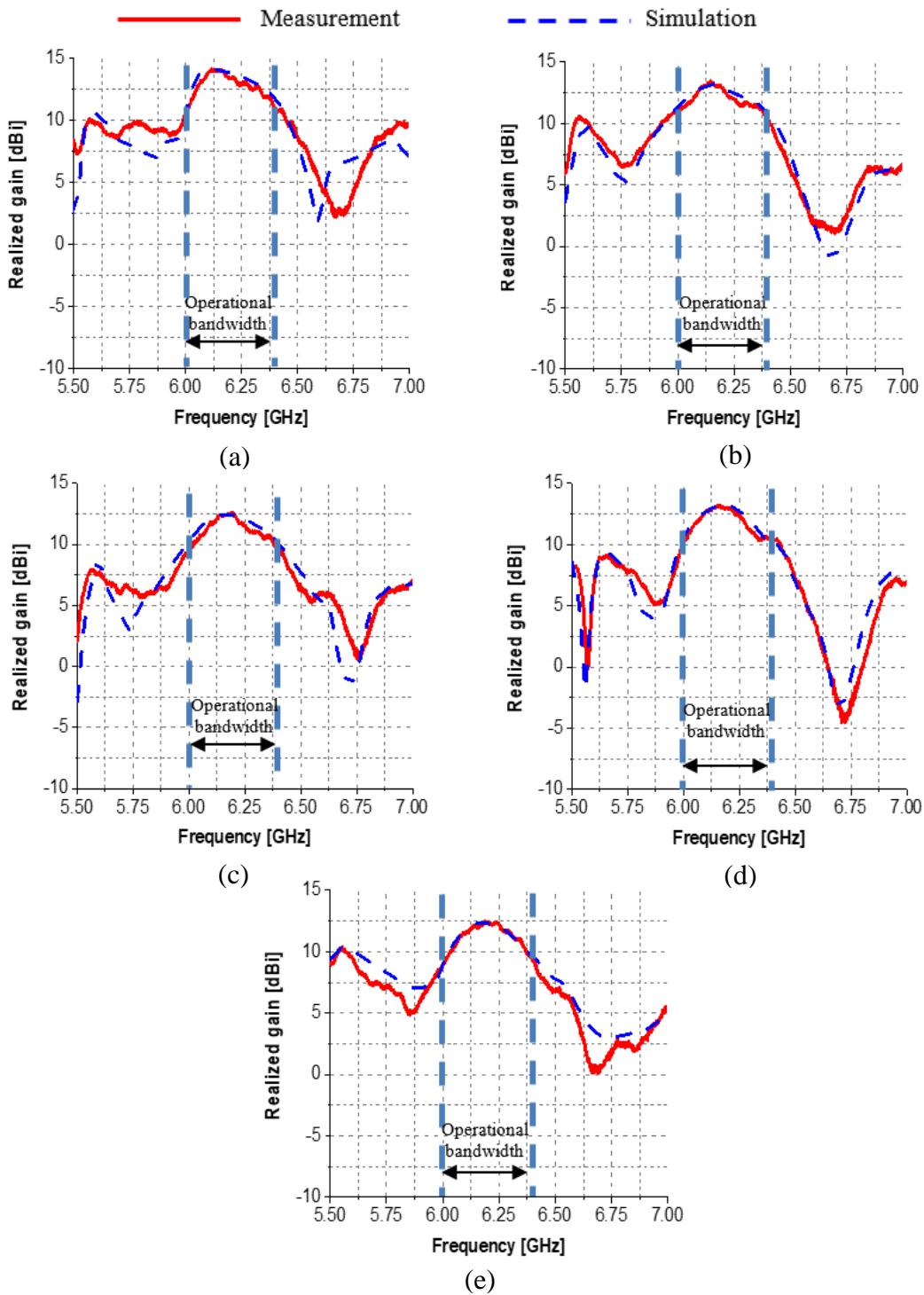
Figure 54: Simulated and measured realized gain of the ESPAR for (a) 0º, (b) 20º, (c) 45º scan angles in the E plane and (d) 20º, (e) 40º scan angles in the H plane.
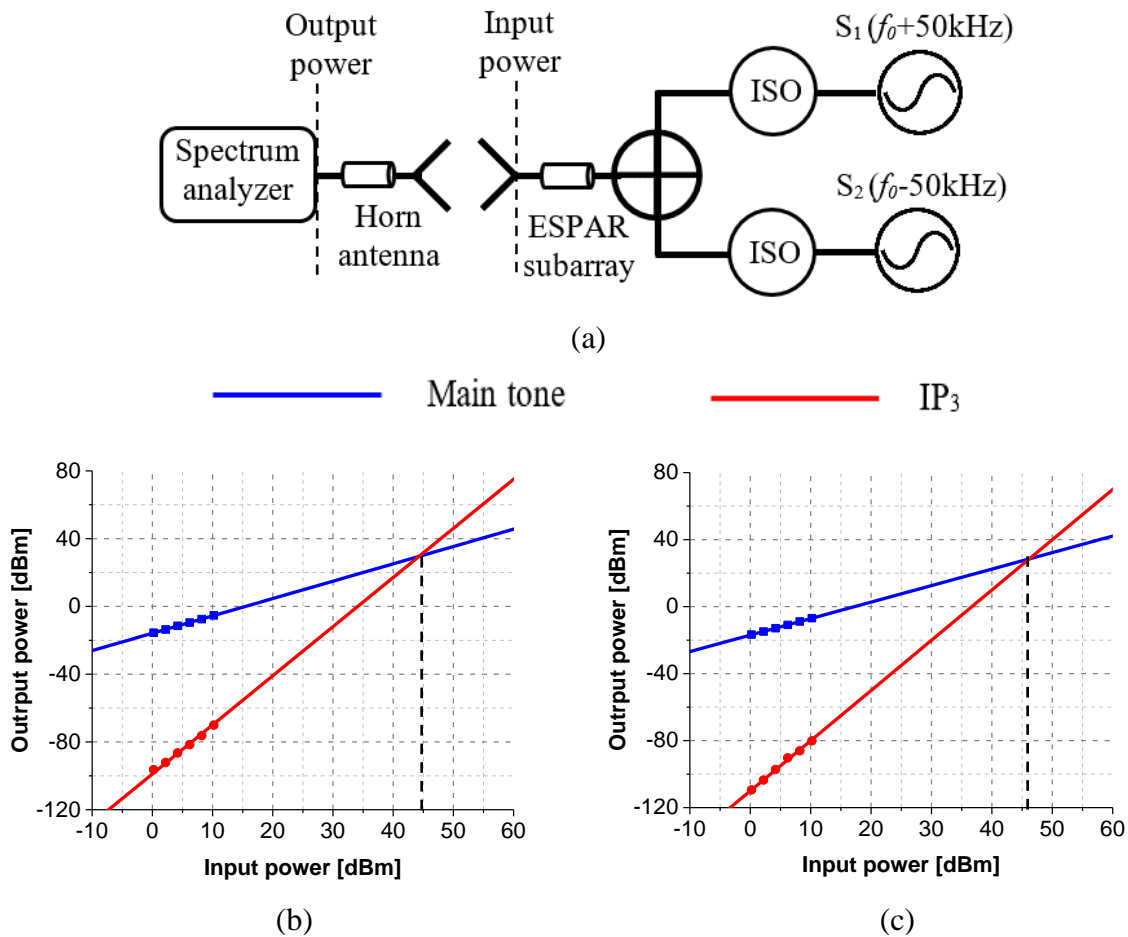
Figure 55: (a) Measurement setup for IIP$_3$. IIP$_3$ of CBS ESPAR subarray for (b) 0° and (c) 30° scan angle in the E plane at 6.2 GHz.

Table 7 compares the proposed CBS ESPAR and other passive phased arrays with reduced number of phase shifters. In contrast to the patch [46] and DRA [58] ESPARs, the CBS ESPAR exhibits much wider scan angles, higher antenna efficiency, and larger 3-dB gain FBW. [25] uses an interwoven feeding network to achieve 50% phase shifter reduction. However, its beamscanning range, FBW and scan loss are inferior to the CBS ESPAR presented herein.

Table 7: Comparison of phased array antennas with reduced number of phase shifters (PSs)

	This work	[46]	[58]	[25]
Radiating element	CBS	Patch	DRA	Patch
Beamsteering capabilities	2-D	1-D	2-D	1-D
PS reduction (%)	80	67	80	50
Center freq. (GHz)	6.2	1.0	10.5	7.8
Aperture size (λ_0^2)	2.4×2.6*	2.0×1.7	7.0×9.4	14.9×2.6
Gain (dBi)	14.0	12.1	22.4	26.4
Antenna efficiency (%)	85	N/A	56	N/A
Aperture efficiency (%)	32*	38	20	88
Max. scan angles (deg.)	±45	±20	±25	±24
Scan loss (dB)	1.5	0.5	0.5	3.0
S_{11} FBW (%)	6.4	1.0	13.6	3.6
3-dB Gain FBW (%)	6.4	1.5	5.7	3.6
Max. SLL (dB)	-10	-7	-10	-10

*The aperture size is defined by the smallest rectangle that can include the 20 cavities. If the total area of 20 cavities is used as the aperture size, then the aperture efficiency increases to 58%.

4.10 Conclusion

A 20-element CBS ESPAR has been demonstrated in both simulations and measurements to operate at 6.2 GHz with 6.4% FBW. Minimum beam squint exists within the entire impedance matching FBW through rigorous studies on the feeding location and coupling iris. This array is able to scan within $\pm 45^o$ and $\pm 40^o$ in the E and H plane, respectively, with the maximum scan loss of 1.5 dB. At all scan angles, the impedance-matching FBW is maintained. The maximum realized gain of 14.0 dBi indicates an 85% antenna efficiency, which is attributed to the use of low-loss SIW cavities. The IIP_3 is found to be above 44.3 dBm. This CBS ESPAR provides an alternative way to develop high-efficiency phased array antennas with large scan angles and reduced costs.

CHAPTER 5   MICROSTRIP-LINE-FED CBS ESPAR

In order to further increase the impedance-matching bandwidth of the CBS antenna presented in chapter 5, a three-element ESPAR using a microstrip-line-fed cavity-backed slot in the E plane is presented in this chapter. The driven element at the center is fed by an open-ended microstrip line and the two parasitic cavities lying in the E-plane are fed by the center driven cavity through coupling irises. The microstrip line coupled to the parasitic cavity is terminated with varactors to provide variable load reactance. By properly designing the load reactance, continuous E-plane beam steering capability can be achieved. The proposed design is able to achieve a 27.2% impedance-matching fractional bandwidth. Additionally, the tunable load can be integrated into the same layer as the microstrip line, which reduces the size of the CBS ESPAR. It is shown that the proposed ESPAR can steer its beam from -30 to 30 degrees in the E plane. The return loss is maintained from 5.00 to 6.58 GHz for all scan angles.

5.1   Introduction of the Microstrip-Line-Fed CBS ESPAR

The 5G mobile network is expected to deploy within the next decade to resolve the significantly increased demand on mobile data traffic. The millimeter-wave (mmW) spectrum has attracted much interest by providing larger allocated signal bandwidth in a densely-populated environment. However, the sub-6 GHz frequency spectrum is still desirable for offering broad 5G coverage within a complex terrain. Therefore, the sub-6 GHz spectrum plays an important role in the future 5G network. In order to further improve the system capacity in the overcrowded sub-6 GHz spectrum, a wideband antenna array with beam scanning capability is desired.

ESPARs are known to be an economical way to achieve beam scanning capability by replacing phase shifters with low-cost varactors but most ESPARs with boresight radiation exhibit a narrow instantaneous FBW. For example, a three-element ESPAR formed by microstrip patches exhibits only 1% FBW and similar bandwidth is observed for a five-element DRA ESPAR in [57]. In [90], an E-plane ESPAR using cavity-backed slot antennas using coaxial feeding was reported to have only 2.4% S_{11} FBW. An ESPAR with a larger FBW is desired to further improve the system capacity for future 5G applications.

In this section, a three-element ESPAR using microstrip-line-fed cavity-backed slot antennas in the E plane is demonstrated to achieve a wide operational bandwidth as shown in Figure 56. By properly designing the load impedance, ±30-degree continuous beam steering capability is realized in the E plane. In addition, the impedance matching of the proposed ESPAR is maintained from 5.00 to 6.58 GHz for all beam scan angles. Compared to [90], the tunable load can be easily integrated with the microstrip line on top of the parasitic element, which reduces the size of the CBS ESPAR.
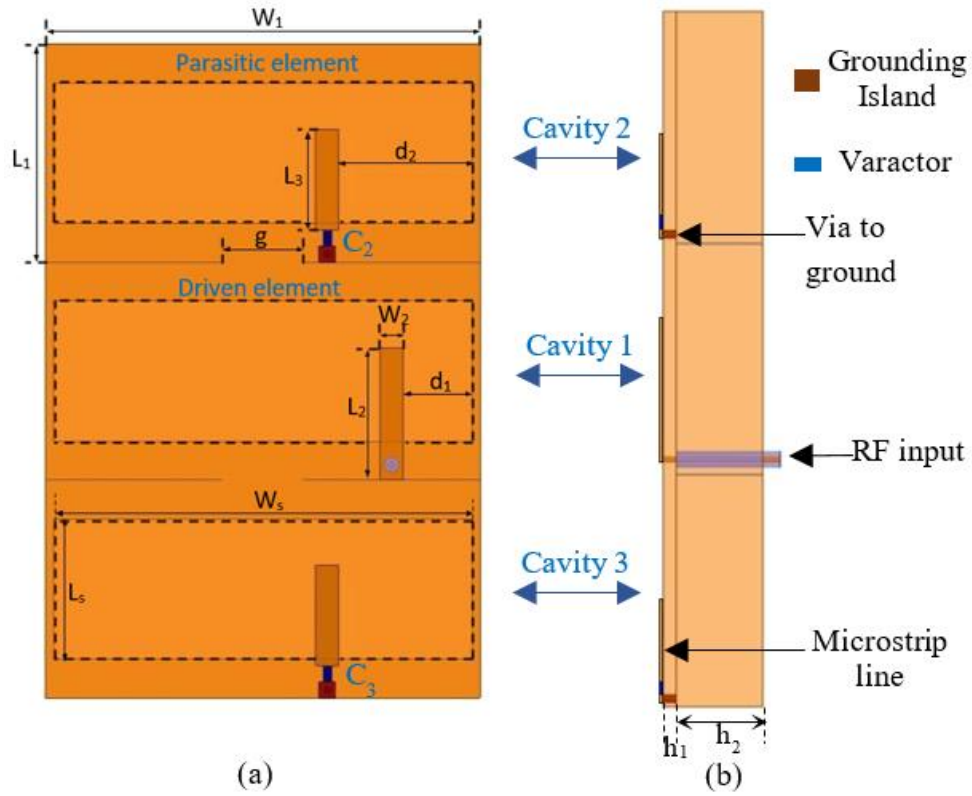
Figure 56: (a) Top and (b) side view of the three-element ESPAR in the E plane. $L_1=13.5$, $L_2=8.2$, $L_3=6.2$, $L_s=8.7$, $W_1=27.0$, $W_2=1.4$, $W_s=26.0$, $d_1=4.3$, $d_2=8.3$, $g=5.0$, $h_1=0.8$, $h_2=5.1$. All dimensions are in mm.

5.2   Microstrip-Line-Fed CBS ESPAR Design

The cavity-backed slot antenna is designed on a 200-mil-thick Rogers TMM 3 ($\varepsilon_r = 3.27$, $\tan\delta = 0.002$) substrate and the microstrip line is designed on a 30-mil-thick Rogers TMM 4 ($\varepsilon_r = 4.5$, $\tan\delta = 0.002$) on top of the cavity as shown in Figure 56. The driven cavity is initially designed to resonate at 5% higher than 6.5 GHz and a slot with length L_s and width W_s is cut at the center of its top surface. The driven element is fed by an open-ended microstrip line which is offset by d_1 to achieve critical coupling to the antenna. A 0.047" semi-rigid cable is used to feed the

microstrip line from the bottom of the cavity. Two parasitic elements are coupled to the driven element through coupling irises in the E plane. The coupling iris width g and offset distance d_2 are slightly adjusted to maximize the impedance matching bandwidth. The microstrip line on top of the parasitic element is terminated by a varactor to provide a variable load impedance for different beam scanning angles. The Z-matrix of the ESPAR is extracted from full-wave simulations and imported into the ANSYS circuit simulator. A co-simulation can be performed to obtain the desired load impedance for different scan angles.

5.3 Microstrip-Line-Fed CBS ESPAR Simulation Results

The ESPAR array shown in Figure 56 is simulated using ANSYS HFSS. The tunable loads are modeled as lumped elements and the equivalent series resistance (ESR) is set to be 1.5 ohm. The impedance matching for different scan angles is displayed in Figure 57. It is observed that S_{11} is maintained below -10 dB from 5.00 to 6.58 GHz for all scan angles. It is observed in Figure 58 that the proposed ESPAR is able to scan from -30° to 30° in the E plane. It is noted that the simulated peak gain is found to be 6.77 dBi at -30° and the realized gain of the ESPAR is maintained to be larger than 5.72 dBi for all beam scan angles. To demonstrate the squint-free bandwidth, the E-plane radiation patterns are plotted in Figure 59 at five different frequencies for boresight radiation. Approximately 93% simulated antenna efficiency is obtained with metallic walls and ideal varactors. The simulated antenna efficiency is reduced to 87% when the ESR is increased to 3.0 ohm. To achieve high antenna efficiency, high-Q Microelectromechanical systems (MEMS) could be used in place of varactors.
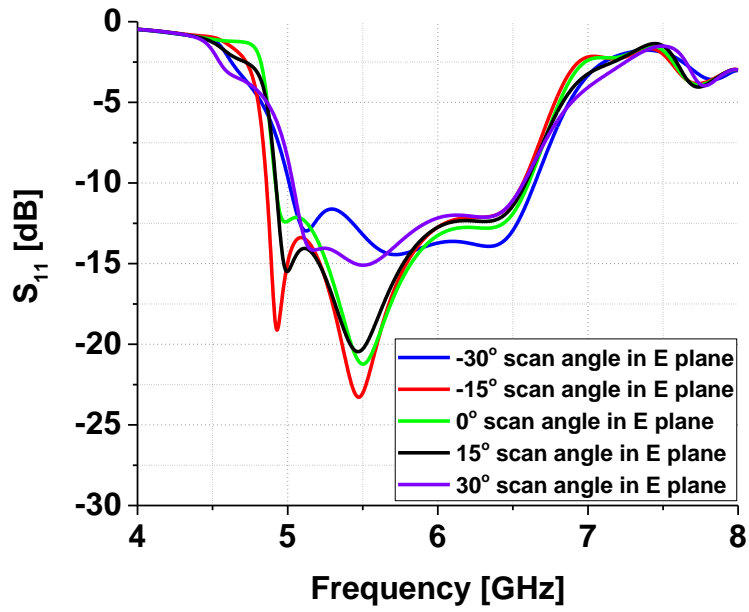
Figure 57: Simulated S_{11} of the ESPAR for different scan angles.
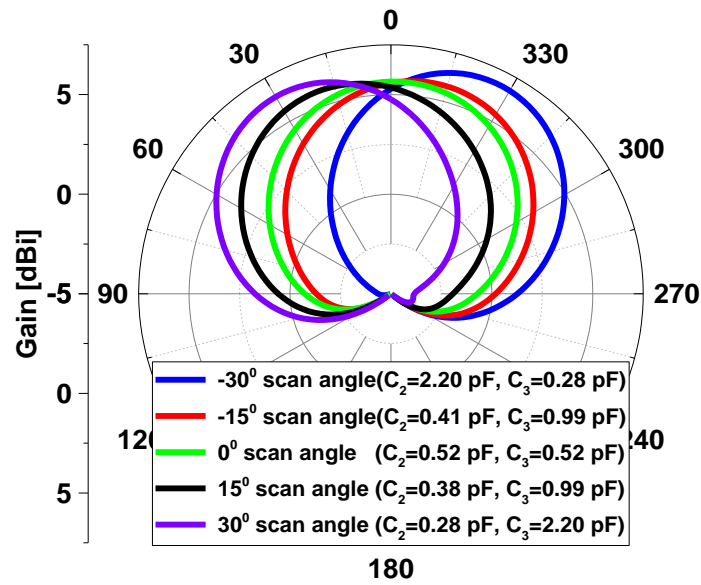
Figure 58: Simulated E-plane radiation patterns for different scan angles at 6.0GHz in linear scale.
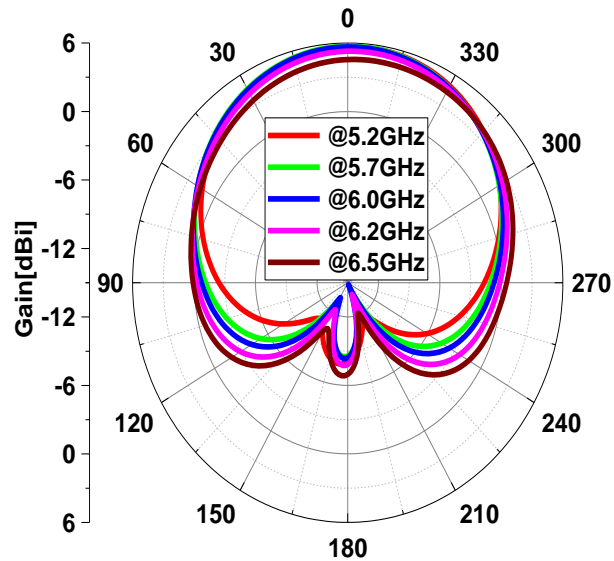
Figure 59: Simulated E-plane radiation patterns at different frequencies for boresight radiation.

5.4   Conclusion

A novel ESPAR using microstrip-line-fed cavity-backed slot antennas in the E plane has been demonstrated. This ESPAR exhibits a 27.2% FBW and ±30-degree beam steering capability in the E-plane. The size of the ESPAR using cavity-backed slot antennas is also further reduced by integrating the tunable load into the same layer as the microstrip line. Moreover, it can be readily extended to a large array with 66% reduction in the number of phase shifters compared to conventional phased arrays.

CHAPTER 6   SUMMARY AND FUTURE WORK

6.1   <u>Summary</u>

The low-cost benefit associated with reducing the number phase shifters and uncomplicated PCB fabrication process has inspired the development of planar ESPARs in the past decade. In order to design an ESPAR with 2-D beamsteering, large scan angles, wide FBW, high efficiency, and minimum beam squint, different antennas are studied in this dissertation. A number of contributions are made in these ESPARs, which are summarized as follows.

First, the introduction of a frequency-reconfigurable microstrip patch ESPAR has enabled frequency diversity of ESPARs without sacrificing the beamsteering performance. The measured results showed that the proposed frequency-reconfigurable patch ESPAR can scan up to $\pm20^\circ$ at each operating frequency, which extends the operational bandwidth by 15 times compared to a frequency-fixed ESPAR. The introduction of DC isolation slits gives explicit control for both mutual coupling and frequency tuning. The simple fabrication associated with the single-layer microstrip patch has made the proposed patch ESPAR readily extendable to large arrays.

In order to achieve E-plane beamsteering, a CBS ESPAR in the E plane was demonstrated. Since the mutual coupling can be easily controlled by adjusting the dimension of the irises in between the cavities, the proposed CBS ESPAR can achieve proper phase shifts in the E plane without the element spacing issue of the DRA ESPARs while maintaining high antenna efficiency as a result of using SIW technology. Moreover, 2-D beamsteering was achieved by coupling two additional parasitic cavities to the driven cavity in the H plane. Since the mutual coupling between the E- and

H-plane parasitic cavities is minimal, independent E- and H-plane beam steering control is achieved by dynamically changing the load reactance of corresponding parasitic elements. The proposed ESPAR cross array is able to steer the beam up to $\pm24^{\circ}$ in the E plane and $\pm20^{\circ}$ in the H plane; the demonstrated scan ranges in either plane are comparable to the CBS ESPAR with 1-D beamsteering.

To further extend the impedance-matching FBW of CBS ESPARs, a three-element CBS ESPAR using a thick substrate and wide slot was designed and measured. In order to suppress the beam squinting within the impedance-matching bandwidth, a customized tunable load which incorporates a delay line, a fixed inductor, and varactor was designed. The measurement results showed that this CBS ESPAR is able to scan from -26° to 20° in the E plane with 4% operational FBW by considering beam squinting.

In addition, a 20-element cavity-backed slot (CBS) ESPAR with 2-D beamsteering and minimized beam squint was designed to demonstrate the implementation of ESPAR in large planar arrays. This 20-element CBS ESPAR is able to scan $\pm45^{\circ}$ and $\pm40^{\circ}$ without grating lobes in the E- and H-planes, respectively; the impedance matching is maintained at all scan angles. The radiation patterns at each scan angle were measured at five discrete frequencies within the operational bandwidth to ensure minimum beam squint.

Finally, a novel microstrip-line-fed CBS ESPAR was shown to further improve the impedance-matching FBW of the CBS ESPARs in simulations.

6.2   Future Work

6.2.1   ESPAR Using Stacked Patch Antennas

Enabling frequency reconfigurability of the patch ESPAR has significantly extended its operational bandwidth but the loss of the varactor increases at lower operating frequencies, degrading the efficiency of patch ESPAR. The introduction of stacked patch antennas has opened up a new solution to achieve wideband patch ESPARs [102]-[104]. In order to achieve the phase shift, tunable loads similar to those presented in chapter 4 can be used to terminate the parasitic stacked patches. As a result, the operational bandwidth of the patch ESPAR can be significantly improved without sacrificing the antenna efficiency.

6.2.2   Circularly Polarized CBS ESPAR

Circularly polarized antenna arrays are desirable for various applications such as satellite navigation and target tracking systems due to their advantages in high link reliability and resistance to the change of atmospheric conditions. The introduction of circularly polarized ESPARs can provide low-cost solutions for the aforementioned applications. Circularly polarized slot backed by cavities has been an active research area for the past decade [105]-[107]. Therefore, it is promising to achieve circularly polarized ESPARs by employing the circular polarized CBS technique. Moreover, sequential feeding can be utilized on the parasitic elements to further improve the axial ratio bandwidth of the ESPAR [59].

LIST OF REFERENCES

[1]   M. Fakharzadeh, S. H. Jamali, P. Mousavi, and S. Safavi-Naeini, "Fast beamforming for mobile satellite receiver phased arrays: Theory and experiment," *IEEE Trans. Antennas Propag.*, vol. 57, no. 6, p. 1645, Jun. 2009.

[2]   G. Han, B. Du, W. Wu and B. Yang, "A novel hybrid phased array antenna for satellite communication on-the-move in Ku-band," *IEEE Trans. Antennas Propag.*, vol. 63, no. 4, pp. 1375-1383, Apr. 2015.

[3]   H. Al-Saedi *et al*., "A low-cost Ka-band circularly polarized passive phased-array antenna for mobile satellite applications," *IEEE Trans. Antennas Propag.*, vol. 67, no. 1, pp. 221-231, Jan. 2019.

[4]   B. P. Kumar, C. Kumar, V. S. Kumar, and V. V. Srinivasan, "Active spherical phased array design for satellite payload data transmission," *IEEE Trans. Antennas Propag.*, vol. 63, no. 11, pp. 4783–4791, Nov. 2015.

[5]   H. Chou, M. Lee and C. Yu, "Subsystem of Phased Array Antennas With Adaptive Beam Steering in the Near-Field RFID Applications," *IEEE Antennas Wireless Propag. Lett.*, vol. 14, pp. 1746-1749, Apr. 2015.

[6]   G. R. MacCartney, T. S. Rappaport, S. Sun, and S. Deng, "Indoor office wideband millimeter-wave propagation measurements and channel models at 28 and 73 GHz for ultra-dense 5G wireless networks," *IEEE Access*, vol. 3, pp. 2388–2424, Dec. 2015.

[7]   J. G. Andrews et al., "What will 5G be?" *IEEE J. Sel. Areas Commun.*, vol. 32, no. 6, pp. 1065–1082, Jun. 2014.

[8]   T. S. Rappaport et al., "Millimeter wave mobile communications for 5G cellular: It will work!", *IEEE Access*, vol. 1, no. 1, pp. 335-349, Aug. 2013.

[9]   W. Roh et al., "Millimeter-wave beamforming as an enabling technology for 5G cellular communications: Theoretical feasibility and prototype results", *IEEE Commun. Mag.*, vol. 52, no. 2, pp. 106-113, Feb. 2014.

[10]   F. Boccardi, R. W. Heath, A. Lozano, T. L. Marzetta, P. Popovski, "Five disruptive technology directions for 5G", *IEEE Commun. Mag.*, vol. 52, no. 2, pp. 74-80, Feb. 2014.

[11]   M. A. Tanha, P. V. Brennan, M. Ash, "Phased array antenna for avalanche FMCW radar", *Proc. Loughborough Antennas Propag. Conf. (LAPC)*, pp. 51-55, Nov. 2013.

[12] M. A. Tanha, M. Ash, P. V. Brennan, "Phased-array antenna feed network for geophysical FMCW radar", *Proc. 8th Eur. Conf. Antennas Propag. (EuCAP)*, pp. 1847-1851, Apr. 2014.

[13] M. Ardeshir Tanha, P. V. Brennan, M. Ash, A. Köhler and J. McElwaine, "Overlapped phased array antenna for avalanche radar," *IEEE Trans. Antennas Propag.*, vol. 65, no. 8, pp. 4017-4026, Aug. 2017.

[14] G. W. Stimson, Introduction to Airborne Radar, West Perth, WA, Australia:SciTech, 1998.

[15] M. Sazegar, "Low-cost phased-array antenna using compact tunable phase shifters based on ferroelectric ceramics", *IEEE Trans. Microw. Theory Techn.*, vol. 59, no. 5, pp. 1265-1273, May 2011.

[16] P. Loghmannia, M. Kamyab, M. R. Nikkhah, R. Rezaiesarlak, "Miniaturized low-cost phased-array antenna using SIW slot elements", *IEEE Antennas Wirel. Propag. Lett.*, vol. 11, pp. 1434-1437, 2012.

[17] X. Ding, B.-Z. Wang, G.-Q. He, "Research on a millimeter-wave phased array with wide-angle scanning performance", *IEEE Trans. Antennas Propag.*, vol. 61, no. 10, pp. 5319-5324, Oct. 2013.

[18] M. Nikfalazar, "Steerable dielectric resonator phased array antenna based on inkjet-printed tunable phase shifter with BST metal-insulator-metal varactors", *IEEE Antennas Wireless Propag. Lett.*, vol. 15, pp. 877-880, 2016.

[19] M. Nikfalazar et al., "Two-dimensional beam-steering phased-array antenna with compact tunable phase shifter based on BST thick films", *IEEE Antennas Wireless Propag. Lett.*, vol. 16, pp. 585-588, 2017.

[20] A. S. Nagra and R. A. York, "Distributed analog phase shifters with low insertion loss," *Microwave Theory and Techniques, IEEE Transactions on,* vol. 47, pp. 1705-1711, 1999.

[21] M. Fakharzadeh, P. Mousavi, S. Safavi-Naeini, and S. H. Jamali, "The effects of imbalanced phase shifters loss on phased array gain," *Antennas and Wireless Propagation Letters, IEEE,* vol. 7, pp. 192-196, 2008.

[22] J. T. Nemit, "Network approach for reducing the number of phase shifters in a limited scan phased array," U.S. Patent 380 362 5, 1974.

[23] A. Abbaspour-Tamijani and K. Sarabandi, "An affordable millimeter-wave beam-steerable antenna using interleaved planar sub arrays," *IEEE Trans. Antennas Progag.*, vol. 51, no. 9, pp. 2193–2202, Sep. 2003.

[24]   B. Avser, J. Pierro, and G. M. Rebeiz, "Random feeding networks for reducing the number of phase shifters in limited-scan arrays," *IEEE Trans. Antennas Propag.*, vol. 64, no. 11, pp. 4648–4658, Nov. 2016.

[25]   B. Avser, R. F. Frazita and G. M. Rebeiz, "Interwoven feeding networks with aperture sinc-distribution for limited-scan phased arrays and reduced number of phase shifters," *IEEE Trans. Antennas Propag.*, vol. 66, no. 5, pp. 2401-2413, May 2018.

[26]   F. Akbar and A. Mortazawi, "Scalable phased array architectures with a reduced number of tunable phase shifters," *IEEE Trans. Microw. Theory Techn.*, vol. 65, no. 9, pp. 3428–3434, Sep. 2017.

[27]   R. Harrington, "Reactively controlled directive arrays," *IEEE Trans. Antennas Propag.*, vol. 26, no. 3, pp. 390-395, May 1978.

[28]   W. Ouyang and X. Gong, "Frequency-Reconfigurable Single-Layer Design of Microstrip Patch Electrically-Steerable Parasitic Array Radiator (ESPAR)", *2016 International Workshop on Antenna Technology (iWAT)*, Orlando, FL., pp. 154-156, Feb. 2016.

[29]   A. Dec, K. Suyama, "Micromachined electro-mechanically tunable capacitors and their applications to RF ICs", *IEEE Trans. Microw. Theory. Tech.*, vol. 46, no. 12, pp. 2587-2596, Dec. 1998.

[30]   L. Dussopt, G. M. Reibeiz, "An X-to Ku-band 3-bit digital MEMS varactor", *IEEE Microw. Wireless Compon. Lett.*, vol. 13, no. 9, pp. 361-363, Sep. 2003.

[31]   Y. Lu, L. P. B. Katehi, D. Peroulis, "High-power MEMS varactors and impedance tuners for millimeter-wave applications", *IEEE Trans. Microw. Theory Tech.*, vol. 53, no. 11, pp. 3672-3678, Nov. 2005.

[32]   G. Kahmen, H. Schumacher, "Interactive design of MEMS varactors with high accuracy and application in an ultralow noise MEMS-based RF VCO", *IEEE Trans. Microw. Theory Techn.*, vol. 65, no. 10, pp. 3578-3584, Aug. 2017.

[33]   T. Ohira and K. Gyoda, "Electronically steerable passive array radiator antennas for low cost analog adaptive beamforming," in *Phased Array Systems and Technology, 2000. Proceedings. 2000 IEEE International Conference on*, 2000, pp. 101-104.

[34]   R. Schlub, J. Lu, T. Ohira, "Seven element ground skirt monopole ESPAR antenna design using a genetic algorithm and the finite element method", *IEEE Trans. Antennas Propag.*, vol. 51, no. 11, pp. 3033-3039, 2003.

[35]   C. Plapous, J. Cheng, E. Taillefer, A. Hirata, T. Ohira, "Reactance domain MUSIC algorithm for electronically steerable parasitic array radiator antenna", *IEEE Trans. Antennas Propag.*, vol. 52, no. 12, pp. 3257-3264, Dec. 2004.

[36] H. Kawakami, T. Ohira, "Electrically steerable passive array radiator (ESPAR) antennas", *IEEE Antennas Propag. Mag.*, vol. 47, no. 2, pp. 43-49, 2005.

[37] D. V. Thiel, "Tin-can antenna a switched parasitic monopole antenna on a finite ground plane with a conductive sleeve", *Proc. CSIRO 7th Australian Symp. Antennas*, pp. 19, 2001.

[38] Y. Ojiro, H. Kawakami, K. Gyoda, T. Ohira, "Improvement of elevation directivity for ESPAR antennas with finite ground plane", *Proc. IEEE 2001 Antennas Propagat. Soc. Symp.*, pp. 18-19, 2001.

[39] J. Lu, D. Ireland, and R. Schlub, "Dielectric Embedded ESPAR (DE-ESPAR) Antenna Array for Wireless Communications," *IEEE Trans. Antennas Propag.,* vol. 53, pp. 2437-2443, 2005.

[40] D. Pozar, "Input impedance and mutual coupling of rectangular microstrip antennas," *IEEE Trans. Antennas Propag,* vol. 30, pp. 1191-1196, 1982.

[41] G. Kumar and K. C. Gupta, "Broad-band microstrip antennas using additional resonators gap-coupled to the radiating edges," *IEEE Trans. Antennas Propag.,* vol. 32, pp. 1375-1379, 1984.

[42] Y. Yusuf and X. Gong, "A low-cost patch antenna phased array with analog beam steering using mutual coupling and reactive loading," *IEEE Antennas Wireless Propag. Lett.*, vol. 7, pp. 81–84, 2008.

[43] J. J. Luther, S. Ebadi, and X. Gong, "Single-layer design of microstrip patch electrically-steerable parasitic array radiator (ESPAR) with integrated DC isolation," in *IEEE MTT-S Int. Microw. Symp. Dig.*, 2012, pp. 1–3.

[44] J. J. Luther and X. Gong, "A microstrip patch phased array antenna with parasitic elements and reactance-tuned coupling," in *IEEE AP-S Int. Symp.*, 2011, pp. 3291–3294.

[45] J. J. Luther, S. Ebadi, and X. Gong, "A microstrip patch electronically steerable parasitic array radiator (ESPAR) antenna with reactance- tuned coupling and maintained reonance," *IEEE Trans. Antennas Propag.*, vol. 60, no. 4, pp. 1803–1813, Apr. 2012.

[46] J. J. Luther, S. Ebadi, and X. Gong, "A low-cost 2×2 planar array of three-element microstrip electrically steerable parasitic array radiator (ESPAR) subshells," *IEEE Trans. Microw. Theory Techn.*, vol. 62, no. 10, pp. 2325–2336, Oct. 2014.

[47] R. White and G. M. Rebeiz, "Single- and Dual-Polarized Tunable Slot-Ring Antenna," *IEEE Trans. Antennas Propag.*, vol. 57, no. 1, pp. 439–448, Jan. 2009.

[48]   N. Behdad and K. Sarabandi, "A Varactor Tuned Dual-Band Slot Antenna," *IEEE Trans. Antennas Propag.*, Special Issue on Multifunction Antennas and Antenna Systems, pt. II, vol. 54, no. 1, pp. 401–408, Jan. 2006.

[49]   S. V. Hum and H. Y. Xiong, "Analysis and Design of a Differentially-Fed Frequency Agile Microstrip Patch Antenna," *IEEE Trans. Antennas Propag.*, vol. 58, no. 10, pp. 3122–3130, 2010.

[50]   Erdil, E.,Topalli, K., Unlu, M., Civi, O., and Akin, T. "Frequency Tunable Microstrip Patch Antenna using RF MEMS Technology". *IEEE Trans. Antennas Propag.*, Vol. 55(4). pp 1193–1196, 2007.

[51]   S. L.-S. Yang, A. A. Kishk, and K.-F. Lee, ''Frequency Reconfigurable U-slot Microstrip Patch antenna,'' *IEEE Antennas Wireless Propag. Lett.*, vol. 7, pp. 127–129, Jan. 2008.

[52]   S. A. Long, M. W. McAllister, L. C. Shen, "The resonant cylindrical dielectric cavity antenna", *IEEE Trans. Antennas Propag.*, vol. AP-31, no. 3, pp. 406-612, May 1983.

[53]   Y. X. Guo, K. M. Luk, K. W. Leung, "Mutual coupling between millimeter-wave dielectric resonator antennas", *IEEE Trans. Microw. Theory Tech.*, vol. 47, no. 11, pp. 2164-2166, Nov. 1999.

[54]   R. J. Dorris, R. T. Long, S. A. Long, M. A. Khayat, J. T. Williams, "Mutual coupling between cylindrical probe-fed dielectric resonator antennas", *IEEE Antennas Wireless Propag. Lett.*, vol. 1, pp. 8-9, 2002.

[55]   R. Chair, A. A. Kishk, K.-F. Lee, "Comparative study on the mutual coupling between different sized cylindrical dielectric resonators antennas and circular microstrip patch antennas", *IEEE Trans. Antennas Propag.*, vol. 53, no. 3, pp. 1011-1019, Mar. 2005.

[56]   M. Ranjbar Nikkhah, J. Rashed-Mohassel and A. A. Kishk, "Compact low-cost phased array of dielectric resonator antenna using parasitic elements and capacitor loading*," IEEE Trans. Antennas Propag.*, vol. 61, no. 4, pp. 2318-2321, Apr. 2013.

[57]   M. R. Nikkhah, P. Loghmannia, J. Rashed-Mohassel, and A. A. Kishk, "Theory of ESPAR design and their implementation in large arrays," *IEEE Trans. Antennas Propag.*, vol. 62, no. 6, pp. 3384–3388, Jun. 2014.

[58]   R. Movahedinia, M. R. Chaharmir, A. R. Sebak, M. R. Nikkhah, and A. A. Kishk, "Realization of large dielectric resonator antenna ESPAR," *IEEE Trans. Antennas Propag.*, vol. 65, no. 7, pp. 3744–3749, Jul. 2017.

[59]   R. Movahedinia, A. Sebak, M. R. Chaharmir, M. Ranjbar Nikkhah and A. A. Kishk, "X-band circularly polarized electronically steerable parasitic array radiator of DRA," *IEEE Trans. Antennas Propag.*, vol. 66, no. 2, pp. 721-728, Feb. 2018.

[60]   D. Deslandes, K. Wu, "Single substrate integration technique of planar circuits and waveguide filters", *IEEE Trans. Microwave Theory Tech.*, vol. 51, pp. 593-596, Feb. 2003.

[61]   F. Xu, K. Wu, "Guided-wave and leakage characteristics of substrate integrated waveguide", *IEEE Trans. Microw. Theory Techn.*, vol. 53, no. 1, pp. 66-73, Jan. 2005.

[62]   L. Yan, W. Hong, G. Hua, J. X. Chen, K. Wu, T. J. Cui, "Simulation and experiment on SIW slot array antennas", *IEEE Microw. Wireless Compon. Lett.*, vol. 14, pp. 446-449, Sep. 2004.

[63]   S. K. Yong and C.-C. Chong, "An overview of multigigabit wireless through millimeter wave technology: Potentials and technical challenges," *EURASIP J. Wireless Commun. Netw.*, vol. 2007, no. 1, p. 50, Jan. 2007.

[64]   Z. Pi and F. Khan, "An introduction to millimeter-wave mobile broadband systems," *IEEE Commun. Mag.*, vol. 49, no. 6, pp. 101–107, Jun. 2011.

[65]   C. H. Doan et al., "Millimeter-wave CMOS design," *IEEE J. Solid State Circuits*, vol. 40, no. 1, pp. 144–155, Jan. 2005.

[66]   H. Shigematsu et al., "Millimeter-wave CMOS circuit design," *IEEE Trans. Microw. Theory Tech.*, vol. 53, no. 2, pp. 472–477, Feb. 2005.

[67]   J. Xue, Z. Feng and P. Zhang, "Spectrum Occupancy Measurement and Analysis in Beijing," presented at the *International Conference on Electronic Engineering and Computer Science*, 2013.

[68]   D. Peroulis, K. Sarabandi, and L. P. B. Katehi, "Design of reconfigurable slot antennas," *IEEE Trans. Antennas Propag.*, vol. 53, no. 2, pp. 645–654, Feb. 2005.

[69]   A. Sheta and S. F. Mahmoud, "A widely tunable compact patch antenna," *IEEE Antennas Wireless Propag. Lett.*, vol. 7, pp. 40–42, 2008.

[70]   M. Komulainen, M. Berg, H. Jantunen, E. Salonen, and C. Free, "A frequency tuning method for a planar inverted-F antenna," *IEEE Trans. Antennas Propag.*, vol. 56, no. 4, pp. 944–950, Apr. 2008.

[71]   N. Behdad and K. Sarabandi, "Dual-band reconfigurable antenna with a very wide tunability range," *IEEE Trans. Antennas Propag.*, vol. 54, no. 2, pp. 409–416, Feb. 2006.

[72]   Y. Cai, Y. J. Guo, and T. S. Bird, "A frequency reconfigurable printed Yagi-Uda dipole antenna for cognitive radio applications," *IEEE Trans. Antennas Propag.*, vol. 60, no. 6, pp. 2905–2912, Jun. 2012.

[73]   C. R. White and G. M. Rebeiz, "A shallow varactor-tuned cavity-backed slot antenna with a 1.9:1 tuning range," *IEEE Trans. Antennas Propag.*, vol. 58, no. 3, pp. 633–639, Mar. 2010.

[74]   S. Zhang, G. H. Huff, and J. T. Bernhard, "A pattern reconfigurable microstrip parasitic array," *IEEE Trans. Antennas Propag.*, vol. 52, no. 10, pp. 2773–2776, Oct. 2004.

[75]   Y. Xue-Song, W. Bing-Zhong, W. Weixia, and X. Shaoqiu, "Yagi patch antenna with dual-band and pattern reconfigurable characteristics," *IEEE Antennas Wireless Propag. Lett.*, vol. 6, pp. 168–171, 2007.

[76]   S. V. Shynu and M. J. Ammann, "Reconfigurable antenna with elevation and azimuth beam switching," *IEEE Antennas Wireless Propag. Lett.*, vol. 9, pp. 367–370, 2010.

[77]   C. Gu, S. Gao and B. Sanz-Izquierdo etc.," Frequency-Agile Beam-Switchable Antenna," *IEEE Trans. Antennas Propag.*, vol. 65, no. 8, pp. 3819-3826, Aug. 2017.

[78]   C. J. Panagamuwa, A. Chauraya, and J. C. Vardaxoglou, "A frequency and beam reconfigurable antenna using photoconducting switches," *IEEE Trans. Antennas Propag.*, vol. 54, pp. 449–454, 2006.

[79]   Q. Qiu, S. Gong, and Y. Xu etc., "A Novel Pattern And Frequency Reconfigurable Microstrip Parasitic Array," *Progress In Electromagnetics Research Letters*, vol. 41, 149-158, 2013.

[80]   S. Nikolaou, R. Bairavasubramanian, C. Lugo, I. Carrasquillo, D. C. Thompson, G. E. Ponchak, J. Papapolymerou, and M. M. Tentzeris, "Pattern and frequency reconfigurable annular slot antenna using pin diodes," *IEEE Trans. Antennas Propag.*, vol. 54, no. 2, pp. 439–448, Feb. 2006.

[81]   G. H. Huff, J. Feng, S. Zhang, and J. T. Bernhard, "A novel radiation pattern and frequency reconfigurable single turn square spiral microstrip antenna," *IEEE Microw. Wireless Compon. Lett.*, vol. 13, no. 2, pp. 57–59, 2003.

[82]   H. Liu, S. Gao and T. H. Loh, "Frequency Agile Small Smart Antenna," *4th Eur. Conf. on Antennas and Propagation (EuCAP 2010)*, Barcelona, Spain, April. 12-16, 2010, pp.1-4.

[83]   L. Haitao, S. Gao, and T. H. Loh, "Compact MIMO antenna with frequency reconfigurability and adaptive radiation patterns," *IEEE Antennas Wireless Propag. Lett.*, vol. 12, pp. 269–272, 2013.

[84]   M. R. Islam and M. Ali, "Elevation plane beam scanning of a novel parasitic array radiator for 1900 MHz mobile handheld terminals," *IEEE Trans. Antennas Propag.*, vol. 58, no. 10, pp. 3344–3352, Oct. 2010.

[85]   Revision of Part 15 of the Commission's Rules Regarding Ultra-Wideband Transmission Systems, First Report and Order (ET Docket 98-153), *Federal Communications Commission, adopted Feb.* 14, 2002, released Apr. 22, 2002.

[86]   A. Giorgetti, M. Chiani, and M. Z. Win, "The effect of narrowband interference on wideband wireless communication systems," *IEEE Trans. Commun.*, vol. 53, no. 10, pp. 2139–2149, Dec. 2005.

[87]   S. Q. Xiao, M. C. Tang, Z. F. Ding, and B.-Z. Wang, "Wide-angle scanning phased array with pattern reconfigurable elements," *IEEE Trans. Antennas Propag.*, vol. 59, no. 11, pp. 4071–4076, Nov. 2011.

[88]   R. L. Xia, S. W. Qu, P. F. Li, D. Q. Yang, S. Yang and Z. P. Nie, "Wide angle scanning phased array using an efficient decoupling network," *IEEE Trans on antenna and propag.*, vol 63, no. 11, pp. 5161-5165, 2015.

[89]   D. Blanco, N. Llombart, and E. Rajo-Iglesias, "On the use of leaky wave phased arrays for the reduction of the grating lobe level," *IEEE Trans. Antennas Propag.*, vol. 62, no. 4, pp. 1789–1795, Apr. 2014.

[90]   W. Ouyang and X. Gong, "A cavity-backed slot ESPAR E-plane array", *2017 IEEE Wireless and Microwave Technology Conference (WAMICON)*, Orlando., FL., pp. 1-3, Apr. 2017.

[91]   W. Ouyang and X. Gong, "Cavity-backed slot ESPAR cross array with two-dimensional beam steering control", *in Proc. IEEE Antennas Propag. Soc. Int. Symp. (APSURSI)*, San Diego, CA, USA, Jul. 2017, pp. 307–308.

[92]   M. M. Jacob, J. Long, and D. F. Sievenpiper, "Non-foster loaded parasitic array for broadband steerable patterns," *IEEE Trans. Antennas Propag.*, vol. 62, no. 12, pp. 6081–6090, Dec. 2014.

[93]   A. Alieldin, Y. Huang and W. M. Saad, "Optimum partitioning of a phased-MIMO radar array antenna," *IEEE Antennas Wireless Propag. Lett*., vol. 16, pp. 2287-2290, Jun. 2017.

[94]   J. D. Díaz et al., "A cross-stacked radiating antenna with enhanced scanning performance for digital beamforming multifunction phased-array radars," *IEEE Trans. Antennas Propag.*, vol. 66, no. 10, pp. 5258-5267, Oct. 2018.

[95]   H. Chou, M. Lee and C. Yu, "Subsystem of Phased Array Antennas With Adaptive Beam Steering in the Near-Field RFID Applications," *IEEE Antennas Wireless Propag. Lett.*, vol. 14, pp. 1746-1749, Apr. 2015.

[96]   R. Siragusa, P. Lemaitre-Auger and S. Tedjini, "Tunable near-field focused circular phase-array antenna for 5.8-GHz RFID applications," *IEEE Antennas Wireless Propag. Lett.*, vol. 10, pp. 33-36, Jan. 2011.

[97]   Y. Abo Rahama, O. Al Aryani, U. Ahmed Din, M. Al Awar, A. Zakaria and N. Qaddoumi, "Novel microwave tomography system using a phased-array antenna," *IEEE Trans. Microw. Theory Techn.*, vol. 66, no. 11, pp. 5119-5128, Nov. 2018.

[98]   T. Lambard, O. Lafond, M. Himdi, H. Jeuland, S. Bolioli and L. Le Coq, "Ka-band phased array antenna for high-data-rate SATCOM," *IEEE Antennas Wireless Propag. Lett.*, vol. 11, pp. 256-259, Mar. 2012.

[99]   C. Ding, Y. J. Guo, P. Qin and Y. Yang, "A compact microstrip phase shifter employing reconfigurable defected microstrip structure (RDMS) for phased array antennas," *IEEE Trans. Antennas Propag.*, vol. 63, no. 5, pp. 1985-1996, May 2015.

[100]   W. Ouyang and X. Gong, "An Electronically-Steerable Parasitic Array Radiator (ESPAR) Using Cavity-Backed Slot Antennas," *IEEE Antennas Wireless Propag. Lett.*, vol. 18, no. 4, pp. 757-761, Apr. 2019.

[101]   J. Galejs, "Admittance of a rectangular slot which is backed by a rectangular cavity," *IEEE Trans. Antennas Propagat.*, vol. AP-11, pp. 119-126, Mar. 1963.

[102]   S. D. Targonski, R. B. Waterhouse, and D. M. Pozar, "Design of wideband aperture-stacked patch microstrip antennas," *IEEE Trans. Antennas Propag.*, vol. 46, no. 9, pp. 1245–1251, Sep. 1998.

[103]   P. K. Singhal, B. Dhaniram, S. Banerjee, "A stacked square patch slotted broadband microstrip antenna", *J. Microw. Optoelectron.*, vol. 3, no. 2, pp. 60-66, Aug. 2003.

[104]   M. A. Matin, B. S. Sharif, C. C. Tsimenidis, "Probe fed stacked patch antenna for wideband applications", *IEEE Trans. Antennas Propag.*, vol. 55, no. 8, pp. 2385-2388, Aug. 2007

[105]   R. Li, B. Pan, A. N. Traille, J. Papapolymerou, J. Laskar, M. M. Tentzeris, "Development of a cavity-backed broadband circularly polarized slot/strip loop antenna with a simple feeding structure", *IEEE Trans. Antennas Propag.*, vol. 56, no. 2, pp. 312-318, Feb. 2008.

[106]   Y. Luo, J. Bornemann, "Circularly polarized substrate integrated waveguide antenna with wide axial ratio beamwidth", *IEEE Antennas Wireless Propag. Lett.*, vol. 16, pp. 266-269, 2017.

[107]   Y. Wu, S. Wong, J. Lin, L. Zhu, Y. He and F. Chen, "A circularly polarized cavity-backed slot antenna with enhanced radiation gain," *IEEE Trans. Antennas Propag.*, vol. 17, no. 6, pp. 1010-1014, June 2018.